ADVANCED GEOPHYSICAL DATA ANALYSIS AT HARVEY-1: STORAGE SITE CHARACTERIZATION AND STABILITY ASSESSMENT

Final report

ANLEC R&D Project 7-1111-0198

Prepared by:

R. Pevzner[1], D. Lumley[2], M. Urosevic[1], B. Gurevich[1,3], A. Bóna[1], S. Ziramov[1], V. Rasouli[1] , J.Shragge[2], M.Pervukhina[3], T.Mueller[3] and V. Shulakova[3]

CURTIN UNIVERSITY - 1, UNIVERSITY OF WESTERN AUSTRALIA - 2 AND CSIRO - 3

3/25/2013

ACKNOWLEDGMENTS

The authors would like to acknowledge contributions to the South-West Hub Flagship project by the Western Australian Department of Mines and Petroleum (including the Geological Survey of Western Australia), the Western Australian Royalty for Regions Program and the Commonwealth Department of Resources, Energy and Tourism. The authors wish to acknowledge financial assistance provided through Australian National Low Emissions Coal Research and Development (ANLEC R&D). ANLEC R&D is supported by Australian Coal Association Low Emissions Technology Limited and the Australian Government through the Clean Energy Initiative.

The authors would also like to thank James Underschultz (ANLEC R&D) and Sandeep Sharma (Schlumberger) for valuable technical review comments regarding the report.

EXECUTIVE SUMMARY

One of the first planned onshore commercial-scale CO_2 geosequestration projects in Australia is at the South West Hub site, approximately 150 km south of Perth, WA. As part of the detailed characterisation work at the site, the new Harvey-1 Data Well was drilled in early 2012 to approximately 3km depth, penetrating the Lower Lesueur formation which is the main CO2 injection target. Its purpose was to obtain rock core samples and other physical data to reduce gaps in geological knowledge and help assess the suitability of the formation for CO_2 storage. Drilling of the Harvey-1 Data Well has provided several geophysical data sets, including log data and zero-offset vertical seismic profiling (ZVSP) data. In addition, a set of 2D seismic lines was acquired in 2011, with basic image processing performed by a contractor. The main goal of this ANLEC research project is to apply a range of advanced data analysis techniques, developed by (or available to) WA:ERA researchers, to the geophysical datasets acquired at the Harvey-1 data well and the recently acquired 2D seismic data, in order to extract higher value from the data, reduce risk in the SW Hub CCS project through improved storage site characterisation, and guide optimal acquisition and processing parameters for future geophysical surveys.

The main conclusions of the 2D seismic data analysis at the SW Hub site are:

- The seismic data quality varies strongly with spatial coordinates, generally improving from west to east, and so careful signal/noise enhancement is required in both seismic acquisition and processing stages.
- Major faults tend to strike NW-SE, and so for optimal 2D and 3D imaging, new seismic acquisition programs should include finer shot-receiver sampling and longer offsets along the east-west or NE-SW (dip) direction.
- Strong near-surface (eg. top 100m) velocity variations are present at the site, probably due to the shallow coastal limestone (high velocity) layer which dips from west to east. Since this high velocity layer does not satisfy the standard “static correction model”, near surface velocity analysis requires advanced techniques.
- Crooked line geometries from collecting 2D seismic data along roads can significantly distort geological structural images, including creating false structures, distorting true structures, and non-imaging of some reflection events altogether. Since crooked line geometry cannot easily be fixed in processing, it is important to minimize data holes and irregular geometry during 3D seismic acquisition.
- High-resolution velocity analysis by both pre-stack time migration (PSTM) and pre-stack depth migration (PSDM) can significantly improve the images of steep faults, fault blocks, and also weak internal reflections (eg. within the Lesueur Fm).

- PSDM tends to improve the images compared to PSTM of large steep-dip faults, major fault blocks, subtle internal faulting and weak reflections within the Lesueur Fm.
- All of the above issues will be important for future 3D seismic surveys acquired at the SW Hub site.

The main conclusions of the ZVSP data analysis at the Harvey-1 well location are:

- A seismic-to-well tie using a VSP corridor stack was performed which shows that the VSP data quality and match to the logs and surface seismic is excellent at the site;
- V_P and V_S velocity profiles were derived for the entire ZVSP depth range to about 1200m depth, and correlate well with other data and velocity analysis techniques.
- Seismic attenuation estimates give values of the apparent Q factor of about 40 for almost the whole depth range.
- Attempts to estimate the relative contribution of scattering and intrinsic attenuation are limited by the log data available for the analysis, however estimates made from existing log data show that contribution of the scattering component should play a very minor role.
- No significant azimuthal shear wave anisotropy was found from shear wave splitting analysis, possibly due to the limited offsets of ZVSP coverage.
- We recommend that full offset (OVSP) surveys be acquired at all future SW Hub wells. Acquisition of walk-away VSP data should also be considered in order to obtain seismic anisotropy parameters required for high quality surface seismic imaging and stress analysis.

The main conclusions of the borehole stress data analysis at the Harvey-1 well location are:

- The mechanical properties of the Yalgorup member are significantly weaker than that of the Wonnerup member. The Yalgorup is composed of interlayers of siltstone and claystone whereas the Wonnerup member is mainly sandstone.
- The results of rock mechanical modelling (RMM) confirmed that the dominant stress regime in the study area is a strike-slip regime.
- Most of the breakouts and drilling events observed from calliper logs and reported in the drilling and well reports were in the Yalgorup member. The RMM has a close agreement with these observations.

- The results of the Rock Mechanical Model (RMM) built for the Harvey-1 well indicate that a more suitable mud weight for drilling could have mitigated the rock failures to a large extent.
- The average direction of the maximum horizontal stress is broadly consistent with the east-west direction reported for the Perth Basin and surrounding areas (King et al., 2008 and references therein).

1. INTRODUCTION

The successful development and execution of large-scale CO_2 geosequestration projects is an essential part of the Low Emission Coal Technologies program in Australia. One of the first planned commercial-scale CO_2 geosequestration projects onshore Australia is at the South West Hub site, approximately 150 km south of Perth, WA.

As part of the detailed site characterisation work at the SW Hub site, the new Harvey-1 Data Well was drilled in early 2012 to approximately 3km depth, penetrating the Lower Lesueur formation which is the main CO2 injection target. Its purpose was to obtain rock core samples and other physical data to reduce gaps in geological knowledge and help assess the suitability of the formation for CO_2 sequestration. Drilling of the Harvey-1 Data Well has provided several geophysical data sets, including log data and zero-offset vertical seismic profiling (ZVSP) data. In addition, a set of 2D seismic lines was acquired in 2011, with basic image processing performed by a contractor.

The main goal of this ANLEC research project is to reduce CCS risk at the SW Hub site by applying a range of advanced data analysis techniques, developed by (or available to) WA:ERA researchers, to the geophysical datasets acquired at the Harvey-1 data well and the 2011 2D seismic data, and thereby improve storage site assessment to a greater degree than can be provided by standard industry service company consulting. Our analysis will help address community concerns and technical issues regarding CO_2 storage, including the four main components of subsurface site characterisation:

1. properties of the reservoir rock to allow the injection and storage of the desired quantities of CO_2;
2. properties of the top seal rock to allow effective containment of the stored CO_2;
3. fault sealing capacity and long term stability to trap CO_2;
4. properties of the *in-situ* rock stress to assess long term stability of the storage site.

In addition, a 3D surface seismic survey will be acquired in 2013 after drilling the Harvey-1 well, to more accurately image the 3D subsurface at the CO_2 injection/storage site. Results of the geophysical data analysis in this report will provide useful input for the design of the 3D seismic survey acquisition parameters and image processing flow.

In this report we:

1. Present the results of our 2D seismic data processing tests and provide recommendations for future 3D seismic data acquisition and processing programs;
2. Present the results of the ZVSP data processing, seismic-well-tie, seismic attenuation analysis, and seismic anisotropy analysis;
3. Present the results of the borehole data stress-field analysis.

2. 2D SEISMIC PROCESSING TEST RESULTS AT THE SOUTH WEST HUB SITE

In this section we describe the results of selected 2D seismic data reprocessing tests using advanced research processing techniques, and make recommendations for future 3D seismic acquisition and processing programs at the SW Hub site.

In the first set of processing tests we select two east-west lines (11GA-LL1 and 11GA-LL2) and reprocess them using nominal (e.g. straight line) geometry. At the initial stage we focus on enhancing data quality, de-noising, and stacking velocity analysis. Initial post- and pre-stack migration results are also presented. We further identify significant issues at the SW Hub site that can create major obstacles to accurate seismic data imaging. Two of the most significant challenges are 1) crooked line acquisition geometry, and 2) the presence of steeply dipping reflection events, often crossing seismic acquisition lines out-of-plane, such as those created by high-dip faults. To address these issues we conduct further advanced processing tests. First, we explore how the crooked line geometry affects imaging, by conducting pseudo-3D processing of two crooked line segments of the 11GA-LL1 line using prestack time Kirchhoff migration (PSTM), and prestack depth wave-equation migration (PSDM). Finally, using the same line, we apply PSDM to test improvement of the images of complex subsurface structure including steep dip faults.

Our processing test results lead us to the following **major conclusions** at the SW Hub site:

1. Seismic data quality varies strongly with spatial coordinates, generally improving from west to east (also see #2 below), and so careful signal/noise enhancement is required in both seismic acquisition and processing stages.
2. Major faults tend to strike NW-SE, and so for optimal 2D and 3D imaging, new seismic acquisition programs should include the finer shot-receiver sampling and longer offsets along the east-west or NE-SW (dip) direction.
3. Strong near-surface velocity variations are present at the site, probably due to the shallow coastal limestone (high velocity) layer which dips from west to east. Since this high velocity layer does not satisfy the standard “static correction model”, near surface velocity analysis requires advanced techniques.
4. Crooked line geometry can significantly distort the structural images, including creating false structures, distorting true structures, and non-imaging of some reflection events altogether. Since crooked line geometry cannot easily be fixed in processing, it is important to minimize data holes and irregular geometry during 3D seismic acquisition.

5. High-resolution velocity analysis by both PSTM and PSDM can significantly improve the images of steep faults, fault blocks, and also weak internal reflections (eg. within the Lesueur Fm).
6. PSDM tends to improve the images compared to PSTM of large steep-dip faults, major fault blocks, subtle internal faulting and weak reflections within the Lesueur Fm.
7. All of the above issues will likely be important for future 3D seismic surveys acquired at the SW Hub site.

2.1. Data Acquisition

Six 2D seismic lines were acquired in 2011 by Geoscience Australia and WA-DMP in the South Perth Basin, Western Australia (Figure 1). For the purposes of easy access for the seismic crew the data was acquired along roads; as a result the lines are crooked. A Vibroseis source was used, with a 25m shot station interval and a nominal 300 channels per shot with a symmetrical split-spread geometry.

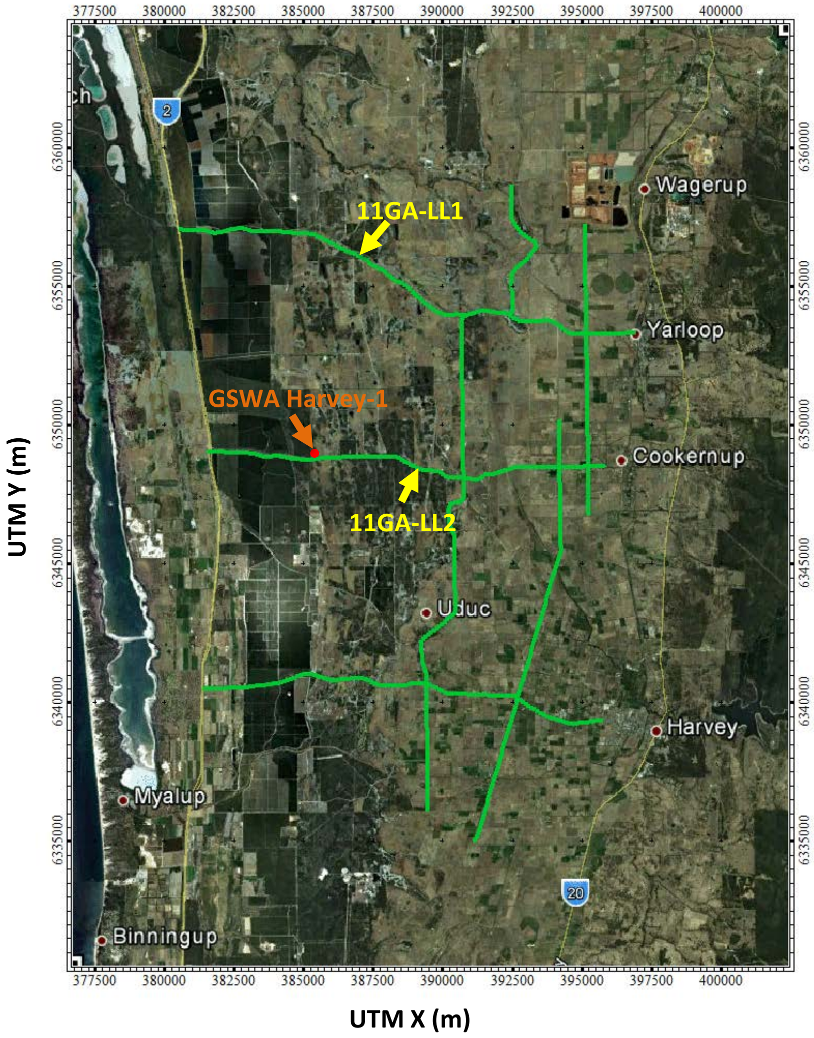

Figure 1. *Location scheme.*

Table 1: Line summary

Line	Number of Shots	2D Km
Line 11GA-LL1	658	17.73
Line 11GA-LL2	537	15.25
Line 11GA-LL3	494	14.88
Line 11GA-LL4	1010	26.65
Line 11GA-LL5	529	15.65
Line 11GA-LL6	378	10.45

The data was initially routinely processed by VelSeis. The main purpose of our research processing tests is to have a detailed look at the target interval and provide recommendations for future 3D seismic surveys.

Two east-west lines were selected for processing:

- Line 11GA-LL1: 658 shots, 17.73 km length
- Line 11GA-LL2: 537 shots, 15.25 km length

The acquisition parameters were as follows:

Table 2: Acquisition parameters

General Survey Parameters	
Survey name	L198 Lower Lesueur
Survey location	Harvey & Waroona Shires, Western Australia
Date of recording	March, 2011
Total Number of Lines	6 Lines
Total Number of Source Points	3606 Points
Bin Size	12.5 m
Total Number of Bins	7984
Nominal Stacking Fold	150
Offset Range	0-3725
Geo Datum	GDA94, MGA Zone 50
Source Parameters	
Source Type	Vibroseis
Source Array	3 Vibrators 30m array length
Sweep Parameters	3 sweeps: 6 - 64 Hz, 12 – 96 Hz, 8 – 72 Hz, 8s sweep
Source Point Spacing	25 m
Receiver Parameters	
Receiver Array	1 x 12, Sensor 10 Hz
Receiver Point Spacing	25 m
Number of Channels	300
Spread Array	3725-12.5-0-12.5-3725
Recording Parameters	
Instrument type	Sercel 428XL
Record length	5000 ms
Sample Interval	2 ms
Recording Filters	High Cut: 200 Hz
Tape Format	SEG-D

Field data quality is good overall, varying with shot location. The data quality generally increases towards the eastern parts of the lines (Figures 2 and 3).

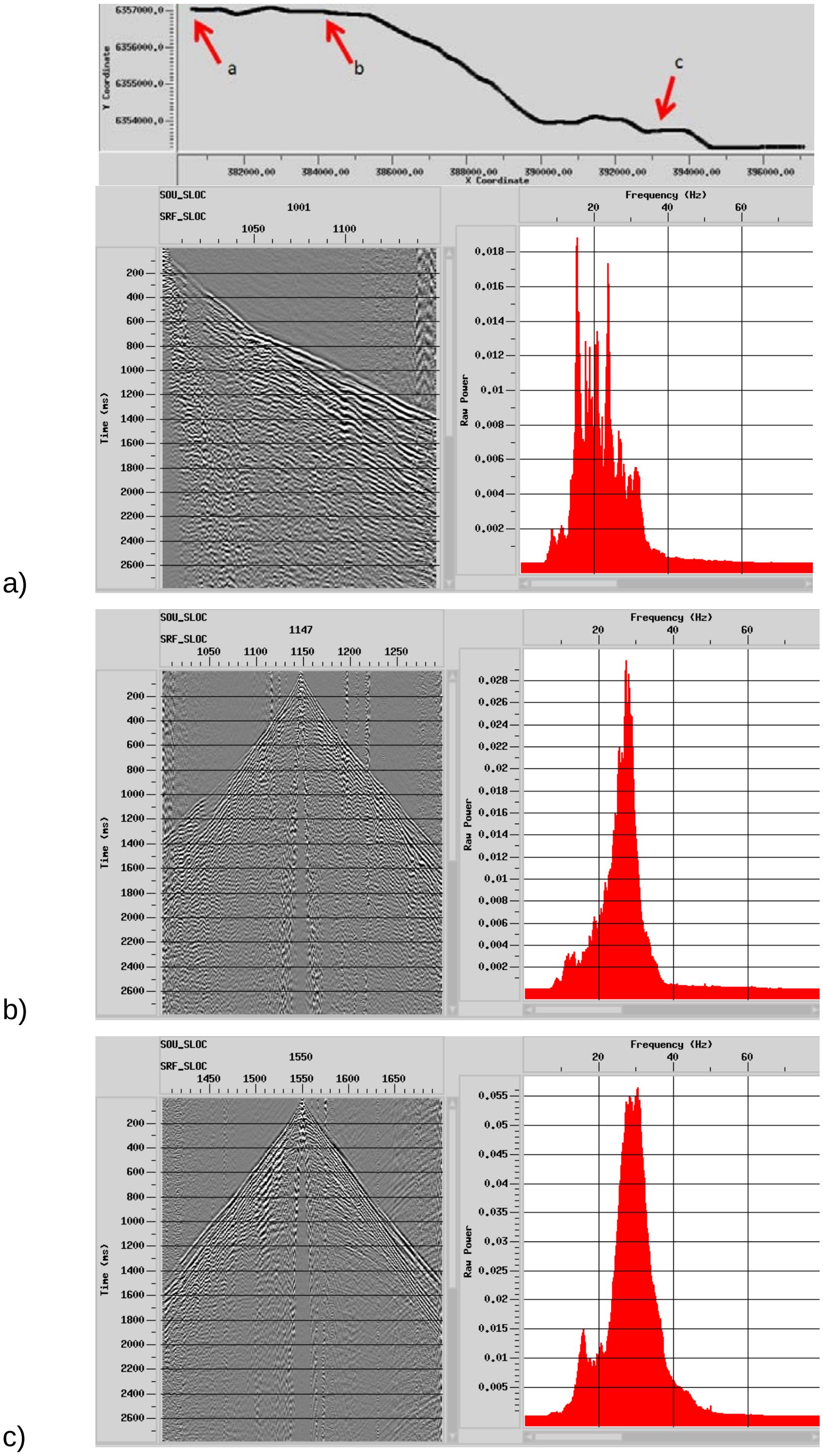

Figure 2. ***Raw data examples from different parts of Line 11GA-LL11 and their amplitude spectra. SOU_SLOC and SRF_SLOC refer to source and receiver station numbers.***

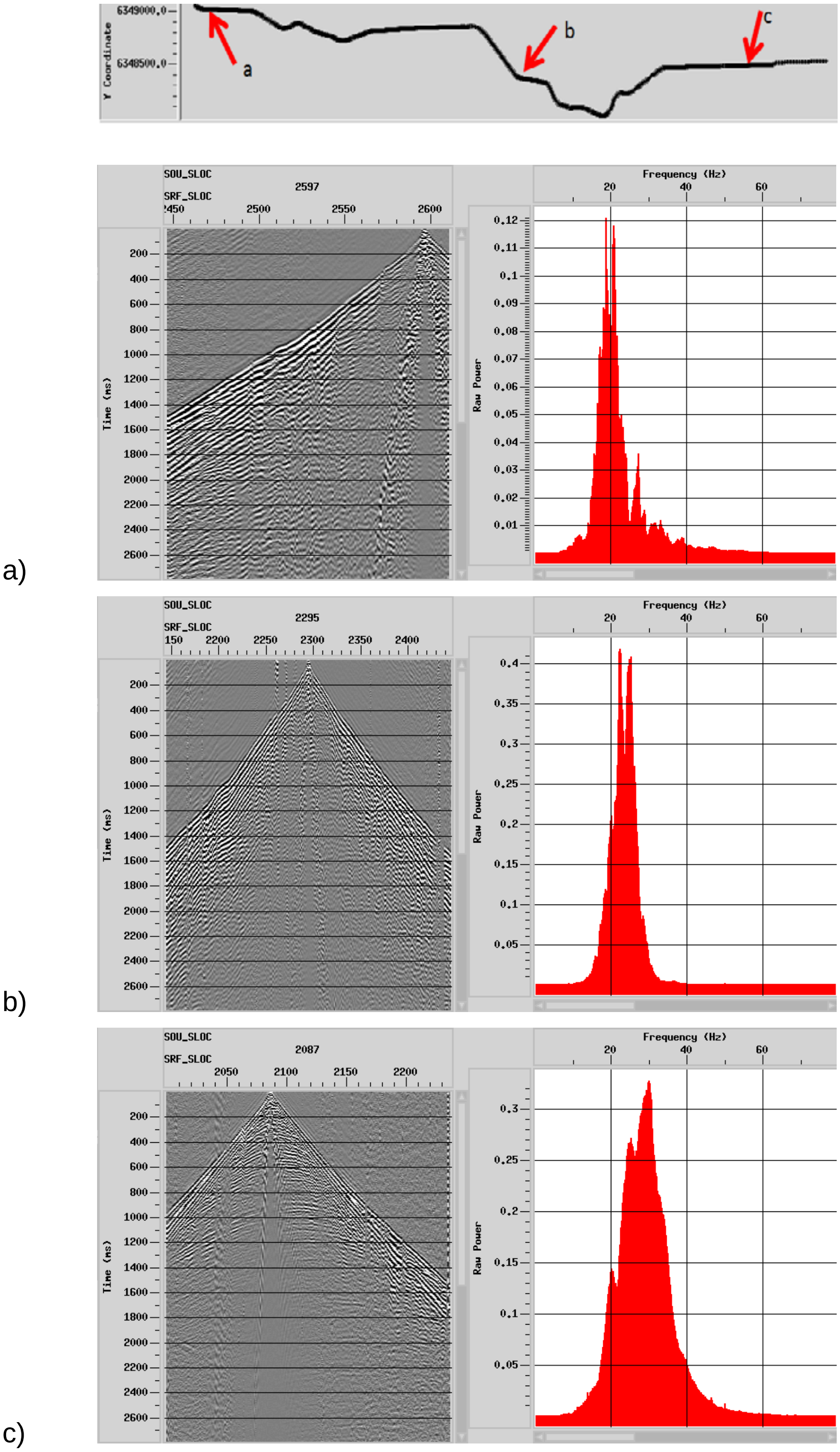

Figure 3. ***Raw data examples from different parts of Line 11GA-LL22 and their amplitude spectra.***

2.2. Data processing assuming nominal (straight-line) geometry

Processing flow chart is shown in the table 3.

Table 3: Processing Flow Chart

Procedure	Parameters
Data Input	**SEG-D data Input**
Geometry assignment	**Applied from ASCII files**
Binning	**Bin size 12.5 m**
Trace Editing	**Kill bad traces**
Elevation Statics	**Final datum elevation – 0 m,** **Replacement Velocity – 2250 m/s**
True Amplitude Recovery	**time power constant 1.5**
Air Blast Attenuation	**Attenuation mode for air velocity at 331 m/s**
TFD Noise Rejection	**Frequency range 0-125 Hz, aperture - 21**
Spiking Deconvolution	**Zero-phase, applied in a gate** **Decon Operator length – 80 ms,** **Operator 'white noise' level – 1%**
Bandpass Filtering	**8-14-70-120 Hz**
Trace Muting	**Top muting**
Automatic Gain Control	**500 ms, applied before FK filter and removed after**
Linear Moveout Correction	**applied before FK filter and removed after**
FK Filtering	**applied in a window**
Bandpass Filter	**7-10-140-150 Hz**
Interactive Stacking Velocity Analysis	**5 iterations**
Residual Static Correction	**2-3 iteration (Max Power Autostatics)**
Normal Moveout Correction	**30% - NMO muting**
Common depth point (CDP) stacking	**Method of trace summing – Mean,** **Power scalar for stack normalisation 0.5**
FX-deconvolution	**Wiener Levinson filter, 1-120 Hz**
Time Migration	**Post-stack Phaseshift, Prestack Kirchhoff**

2.2.1. Geometry

All data was loaded into the processing system and reformatted to internal ProMax format. Geometry information was extracted from the ASCII files. A midpoint distribution was then calculated for lines 11GA-LL1 and LL2 (Figure 4). Midpoints are displayed as white points, sources and receivers as black points. The spatial midpoint distribution is uneven and deviates up to 800 m in some places due to the crookedness of the line geometry.

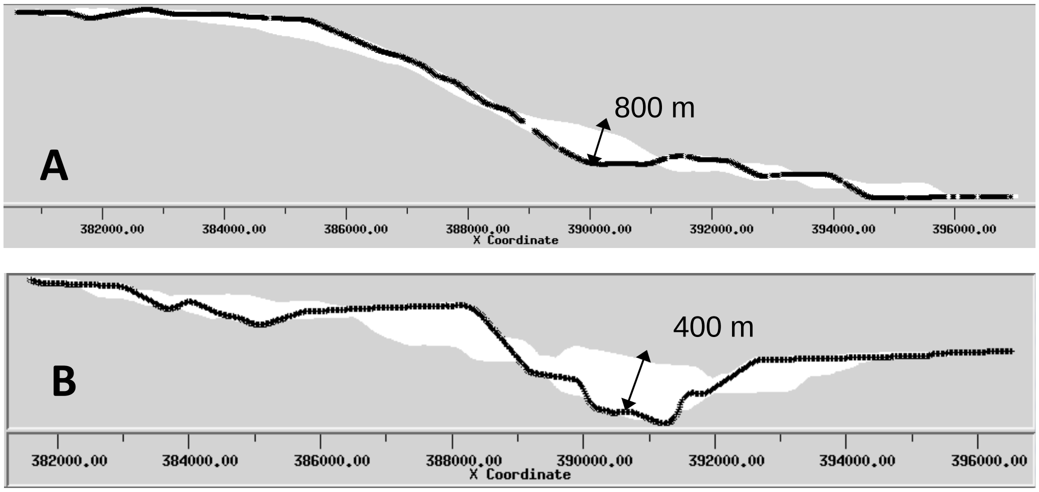

Figure 4. ***Midpoint distribution for (a) Line 11GA-LL1 and (b) Line 11GA-LL2 (not to same scale).***

The data was first processed assuming a straight line where the angular relationship between the shot and the receivers was not taken into account. The bin size is 12.5 m.

Distribution of CDP fold for both lines is shown in Figure 5. Maximum CDP fold is in the centre (up to 140) it then decreases to the edges of the survey.

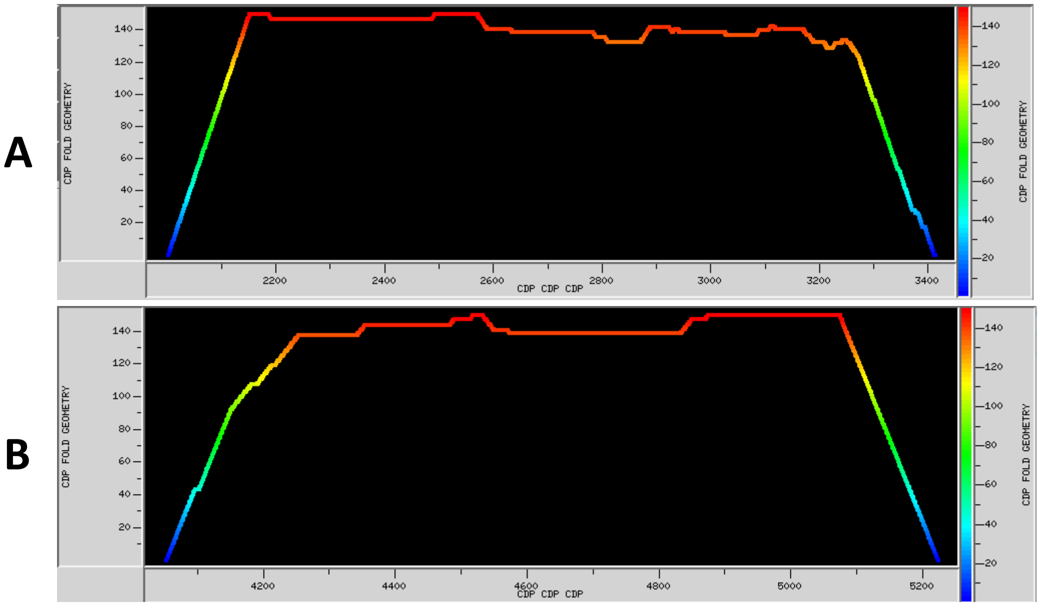

Figure 5. ***CDP fold distribution (range 0-150) for Line 11GA-LL1 (a) and Line 11GA-LL2 (b). Horizontal axis is labelled with CDP numbers.***

All geometry information was assigned to the trace headers. It includes source, receiver and CDP locations along with offsets, elevations and CDP fold.

2.2.2. Pre-processing

Trace Editing

Trace editing includes:

- killing bad traces (noisy traces and traces without signal were picked manually),
- top trace muting with the following parameters:

AOFFSET, m	TIME, ms
0	25
450	330
2125	1360
3660	2240

Elevation statics

The topography is mostly flat over the survey area. Variation in elevation is a maximum of 40 m with the values varying from 6 to 45 m. In order to compensate for the effects of variation in elevation, static shifts have been applied from ASCII statics files provided by VelSeis. The static shifts were calculated using a single layer refraction method (Lawton 1989). The weathering velocity was set to 800 m/s. For this refraction method, first breaks were picked on a refractor corresponding to the base of weathering. Offset was limited to 750 m:

Final datum elevation – 0 m, Replacement Velocity – 2250 m/s.

The maximum time shift is about 40 ms (see Figure 6). Total static correction was up to 8 ms on the Eastern side.

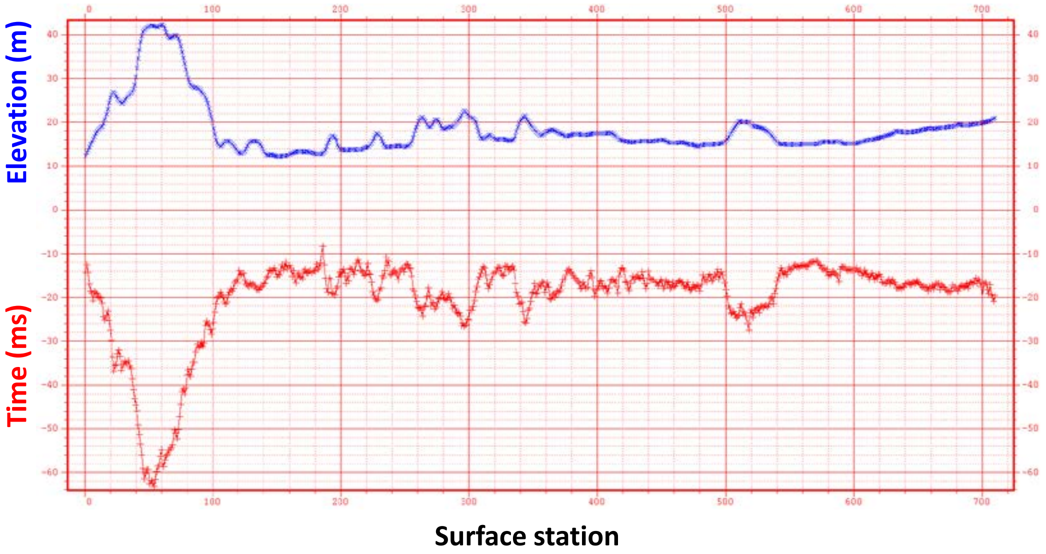

Figure 6. ***An example of elevation changes (blue line) and static shifts (red line) for receivers for Line 11GA-LL1.***

True Amplitude Recovery

The loss of amplitude as a function of time is a consequence of several factors such as geometrical spreading of the wave front, absorption of the signal and transmission coefficient loss. After testing different gain functions the following parameters were chosen:

- apply time raised to a power correction with time power constant equal to 1.5 (ie. t 1.5).

Air Blast Attenuation and Noise Reduction

Air blast attenuation was applied in attenuation mode for an air-wave velocity of 331 m/s. TDF noise rejection applied to the data isolated noise by replacing it with the median spectral amplitudes calculated from 21 adjacent traces. The frequency range was set to 0-125 Hz.

Spiking Deconvolution

In order to improve the shape of the wavelet and increase temporal resolution a deconvolution was applied. After testing different algorithms the following parameters were chosen:

Type – spiking, zero-phase.

Deconvolution operator length was estimated from autocorrelation functions (Figure 7) and seismograms after deconvolution with different operator lengths (50, 60, 70, 80 and 100 ms). An operator length of 80 ms was chosen.

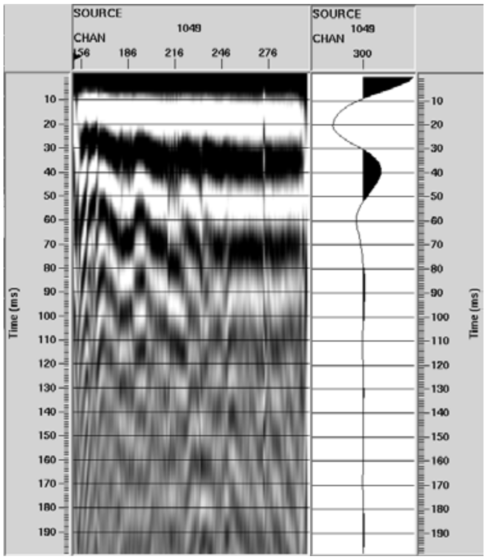

Figure 7. Autocorrelation functions for SOU_SLOC 1550 for Line 11GA-LL1 (left) and the result of function summing (right).

Deconvolution was applied in a specially designed window (see Figure 8). This design window started below the first break noise. Added white noise was 1%. An example of an amplitude spectrum before and after deconvolution is shown in Figure 9.

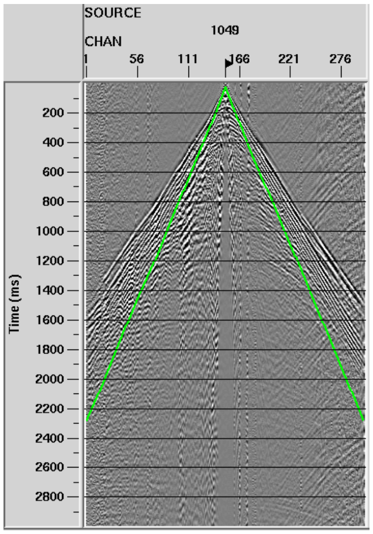

Figure 8. Deconvolution operator window.

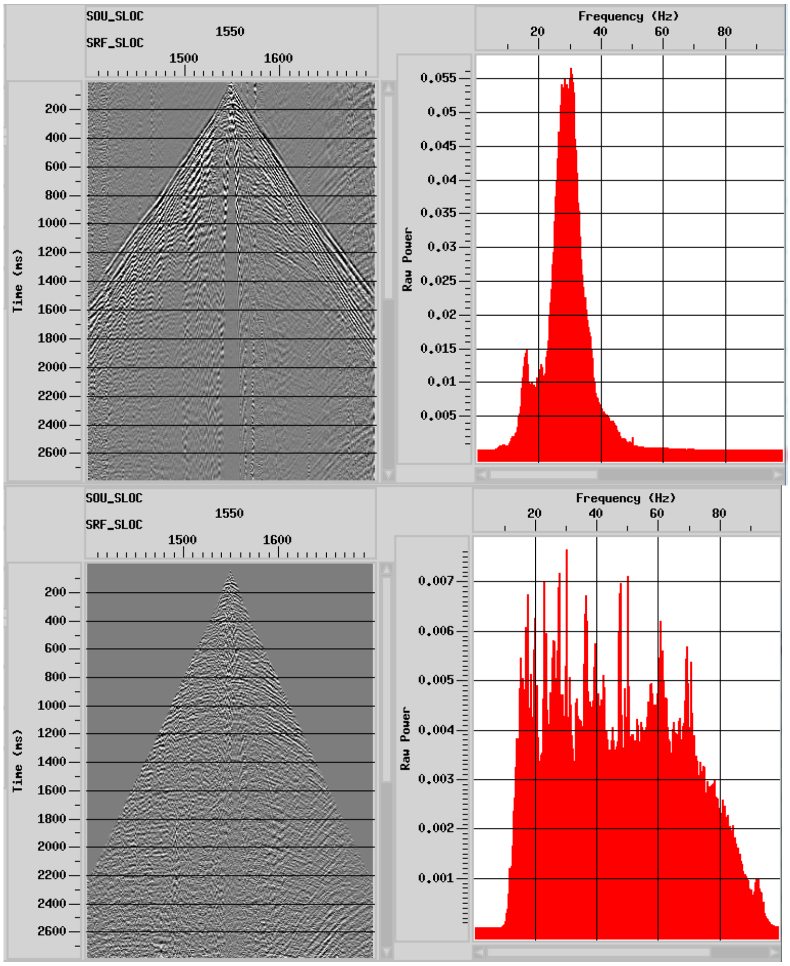

Figure 9. Example of an amplitude spectrum before (top row) and after **(bottom row) deconvolution for SOU_SLOC 1550 for Line 11GA-LL1.**

Bandpass Filter

An Ormsby bandpass filter was applied with the following parameters - 8-14-90-140 Hz. The purpose was to remove low frequency noise from the data. It doesn't affect high frequencies at this stage. The hi-cut slope 90-140 Hz was applied to suppress Gibb's artifacts (sidelobe ringing). The filter was reapplied after deconvolution.

FK Filtering

FK filtering was applied in three consecutive steps. In order to be able to delineate between signal and noise in the FK plane, a linear moveout correction was applied before each step of filtering and then removed from the data. Each time the filter was applied in a specially designed polygon containing different noise components of the wavefield.

Automatic gain control (AGC) was applied before all steps of filtering and then removed from the data. AGC operator length was set to 500 ms.

FK filtering was applied in a ‘pass’ mode (Figure 10).

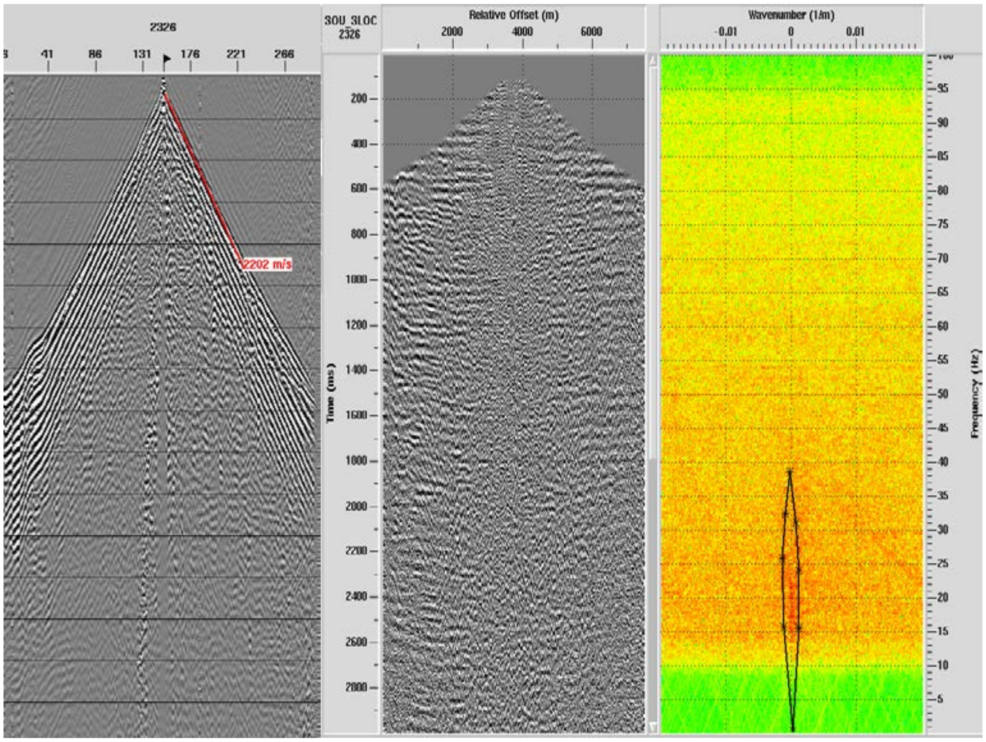

Figure 10. A seismogram before and after linear moveout correction (1st iteration) and an example of an FK polygon.

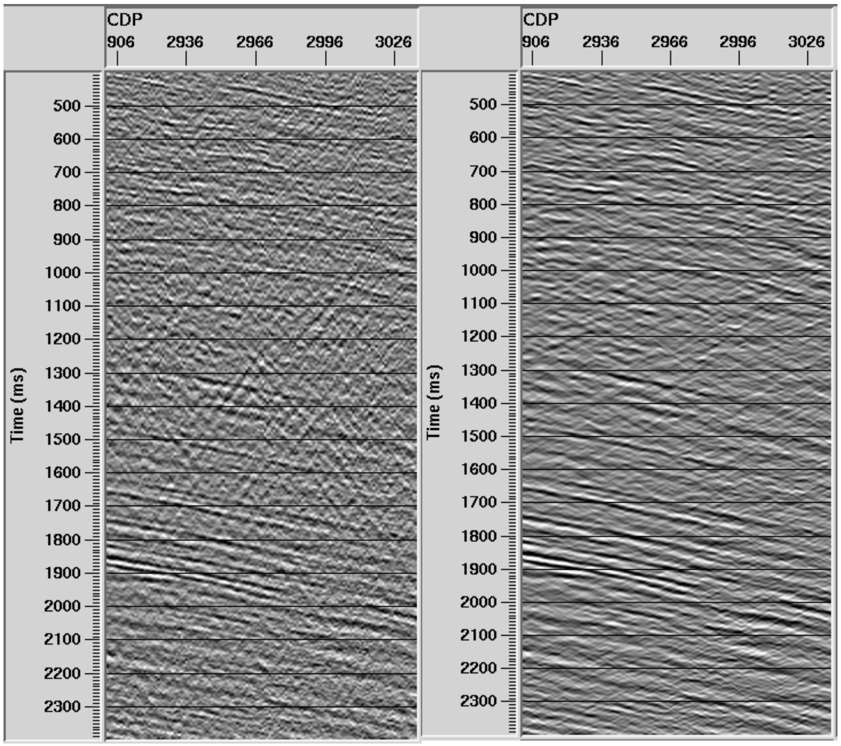

Figure 11. A fragment of the CDP stacked section before (left) and after (right) application of the first (out of three) FK filter.

Pre-processing for velocity analysis and residual static correction

In order to improve the continuity of reflections, special pre-processing was applied to the data for enhanced velocity analysis and statics correction calculations.

Bandpass filter (8-14-40-60 Hz) along with AGC (500 ms window) was applied to CDP gathers to reduce low and high frequency noise and intensify reflections.

Especially for velocity analysis 2D super-gathers were formed from the data.

This pre-processing routine was performed only for velocity analysis and static correction calculations. The final processing result was obtained without it.

2.2.3. Velocity Analysis

Four sets of velocity analysis were carried out.

The first two passes were done before the dip moveout correction (DMO) and the last two – after DMO application.

The first pass was done before the residual static correction. Velocities were picked on a sparse grid ~ 500 – 800 m in the areas of the strongest signal.

The second pass velocity analysis was done after the residual static correction. Velocities were picked on a finer 300m grid. Interactive velocity analysis was performed using supergathers, semblances and CVS panels (Figure 12 and Figure 13). It can be seen that the RMS velocities correspond to the changes in geological structures.

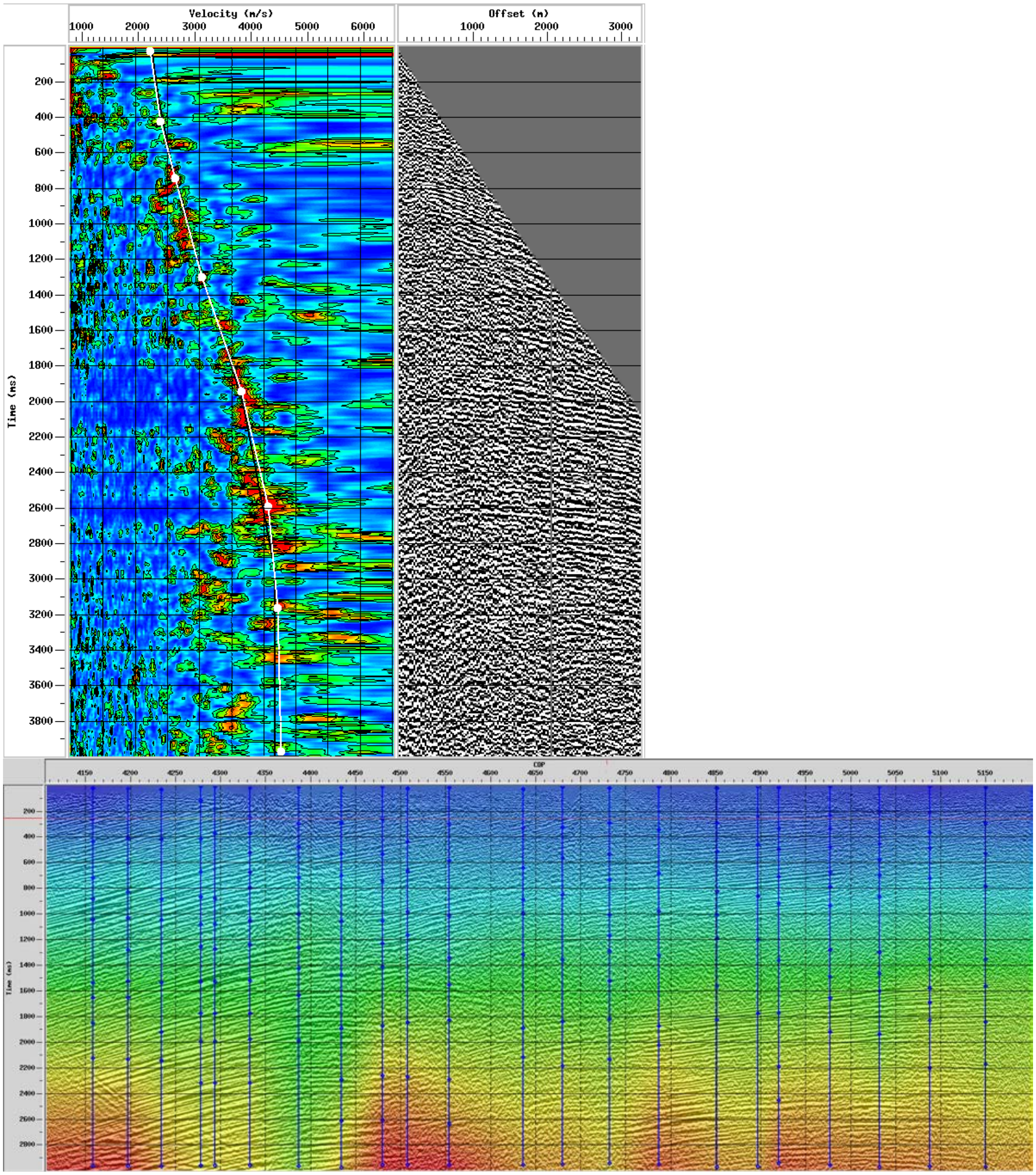

Figure 12. Interactive velocity analysis for Line 11GA-LL1: example of supergather, velocity semblance and velocity field with marked points of velocity analysis (1st iteration).

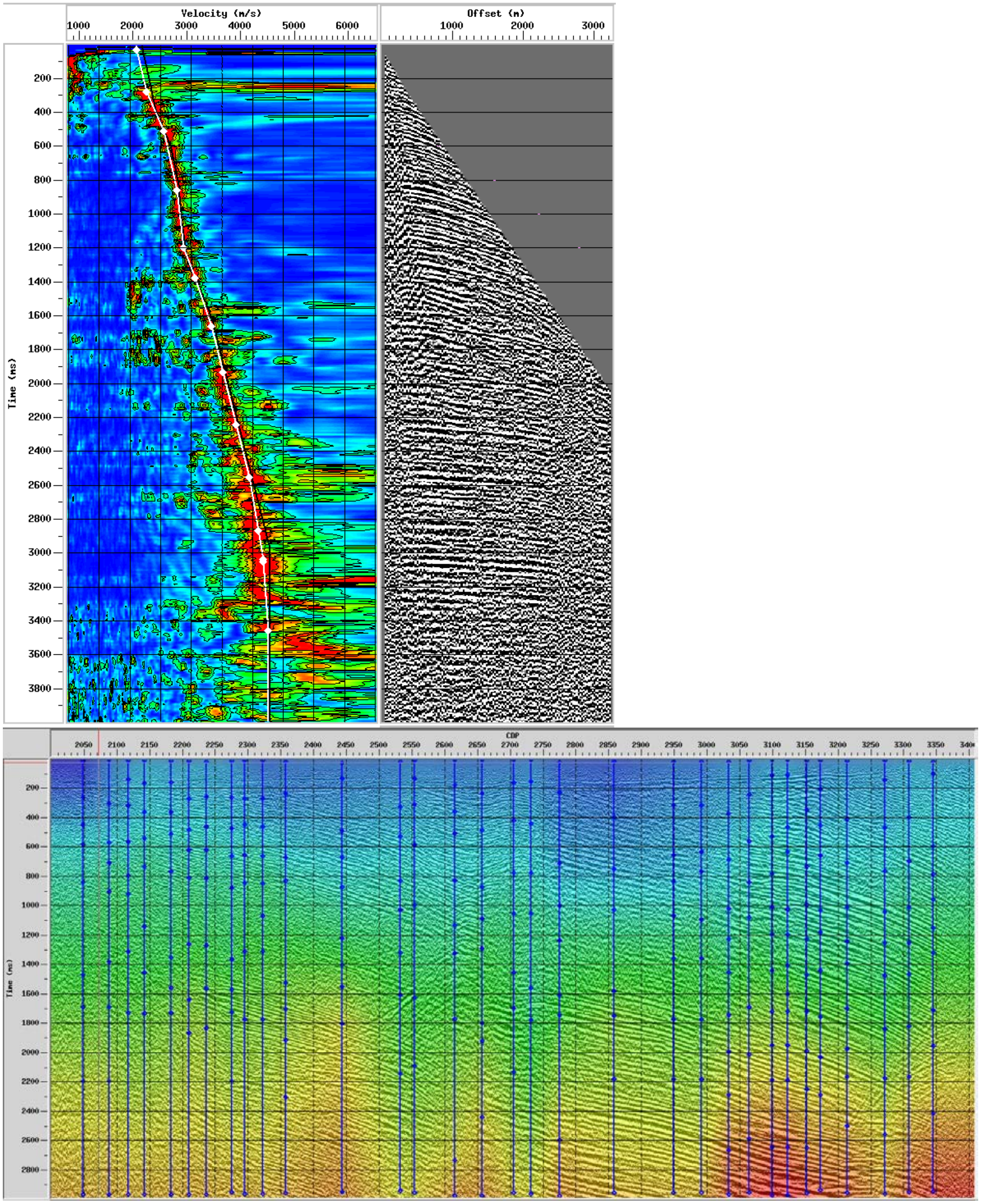

Figure 13. Interactive velocity analysis for Line 11GA-LL2: example of supergather, velocity semblance and velocity field with marked points of velocity analysis (1st iteration).

2.2.4. Residual Static Correction

Elevation and refraction static corrections can only compensate for slow spatial variations in the near-surface weathering layer velocity. Residual static corrections are additionally needed to correct for rapid near-surface spatial velocity variations that result in rapid timeshifts and weak reflector continuity within prestack gather traces.

The residual static model inherently assumes that the near-surface layer is lower velocity compared to the deeper layers, which allows the static corrections to be estimated and applied as a single “static” time shift per each trace. However, if the near surface layer is higher velocity compared to deeper layers (as is the case in some areas of the SW Hub site), the residual static model is no longer valid and the corrections must instead be estimated via tomography (for example) and applied as time-varying shifts to each trace.

Residual static corrections were calculated using the method of Maximum Power autostatics (Ronen and Claerbout 1985). It includes two stages: first – horizon picking, second – static shift calculation. The smash parameter was set to 31. The window used for the trace correlation calculations was 300 ms.

After static corrections, velocity analysis was performed. Elimination of high frequency static shifts improves continuity of the reflection data. As a result, surface consistent residual statics showed considerable improvement in the continuity of the main horizons (Figure 14). However, as noted above, due to the high velocity near surface layer (coastal limestone?) present at the SW Hub site, a more advanced analysis (eg. tomography) should be performed that does not rely on the static model low-velocity assumption.

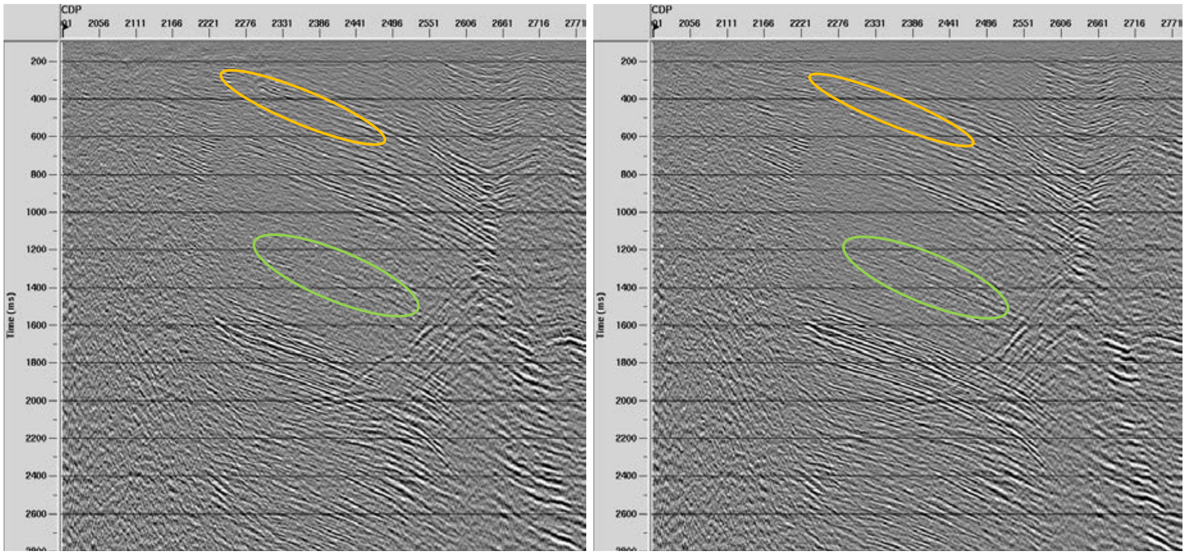

Figure 14. A fragment of a stacked section from Line 11GA-LL1 with previous and current velocities and statics (coloured circles indicate examples of areas with significant changes).

2.2.5. CDP Stacking

The data was stacked using the mean method for trace summing. The root power scalar for stack normalisation was set to 0.5.

2.2.6. Post Processing

Post processing includes the following routine:

- Time variant (TV) spectral whitening,
- FX-deconvolution.

In order to increase the continuity of the main horizons and further suppress noise, FX-Deconvolution was applied to the data with the following parameters:

- Type of filter – Wiener Levinson,
- Percentage of white noise - 1%,
- Horizontal window length – 31,
- Time window length - 300 ms,
- Frequencies – 1-120 Hz.

2.2.7. Time migration

CDP stacked sections were migrated using post- and pre- stack migration algorithms. Post-stack Phase-shift migration was applied for the frequency range 6-120 Hz (Figure 15-16 a and b). Dips of up to 90 degrees were included in calculations. The result is less noisy but migration fails to resolve the fault in the middle of the section observed in the pre-stack migrated images (see below and, also, in section 2.4).

Pre-stack Kirchhoff time migration with the same parameters provides a better result (shown in Figure 15 c and Figure 16c) for the lower part of the lines.

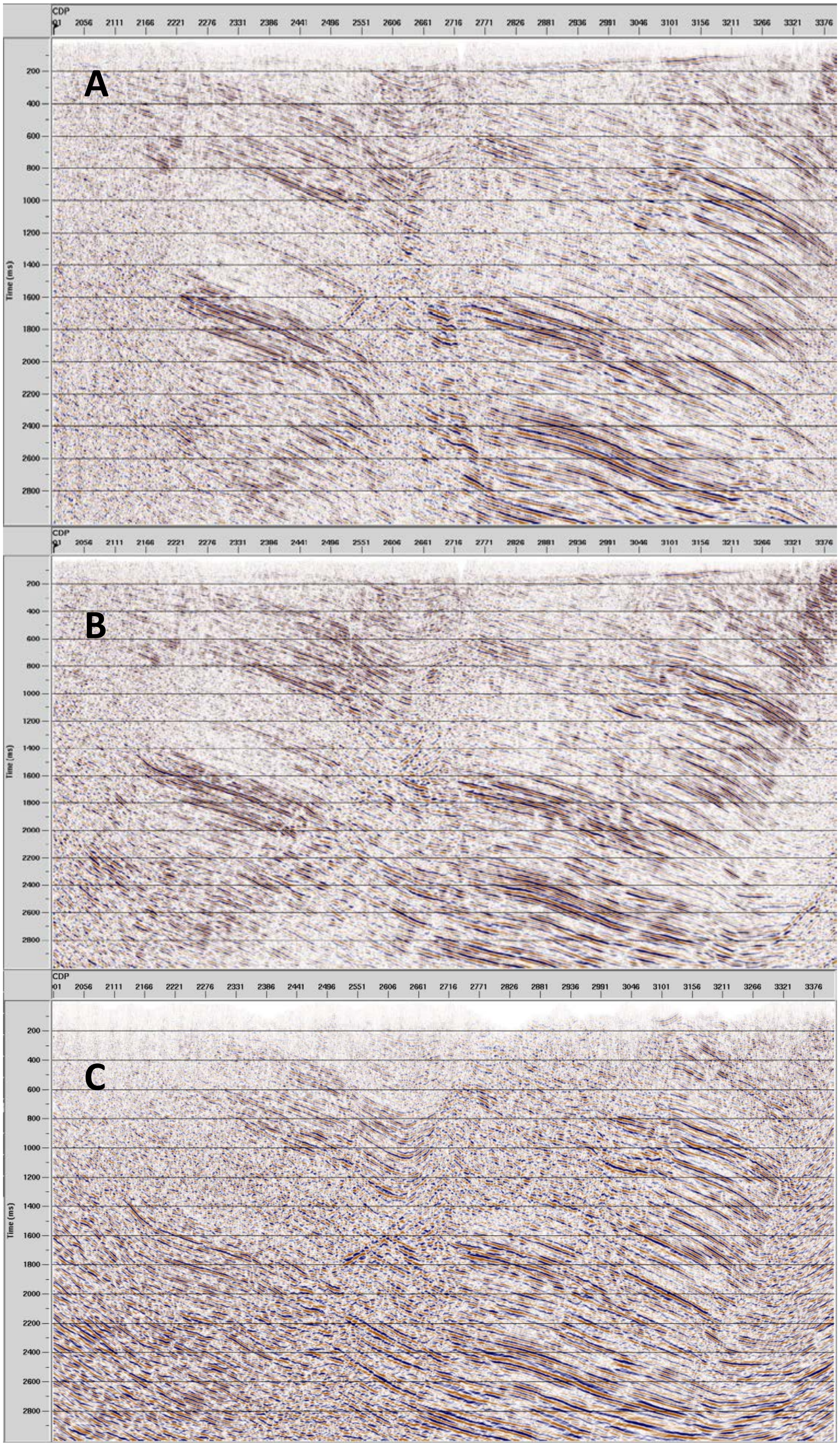

Figure 15. Line 11GA-LL1 CDP time stack before (a) and after migration (b – post stack, c – pre-stack).

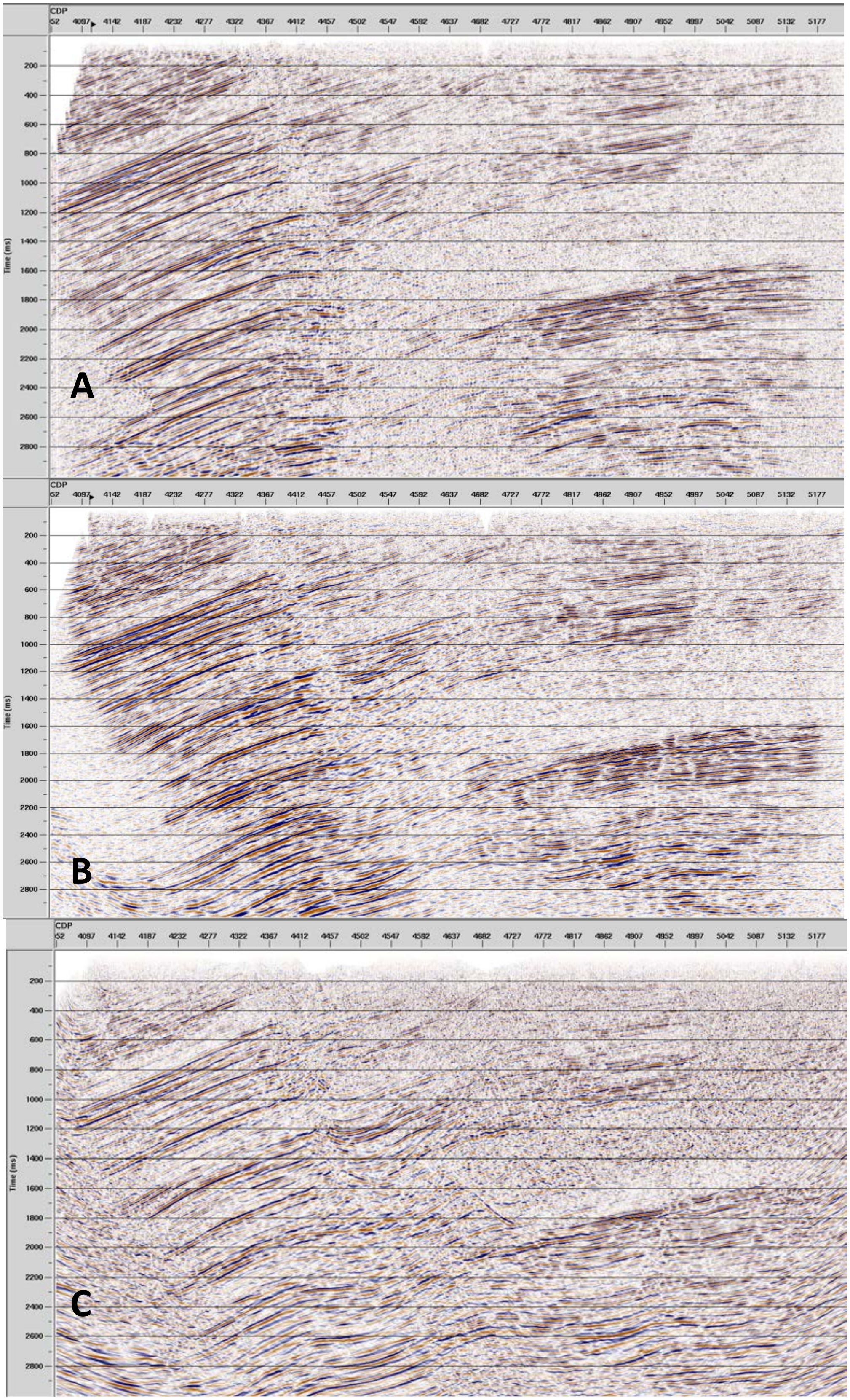

Figure 16. Line 11GA-LL2 CDP time stack before (a) and after migration (b - post-stack, c - pre-stack).

2.2.8. Processing using nominal straight-line geometry – observations

Refraction

Figure 17 demonstrates a simple refraction stack for 2900 m offset and 2500 m/s velocity. A strong shallow refractor is visible that varies between 40-120 ms time depth along the line, which may be related to the coastal limestone deposit.

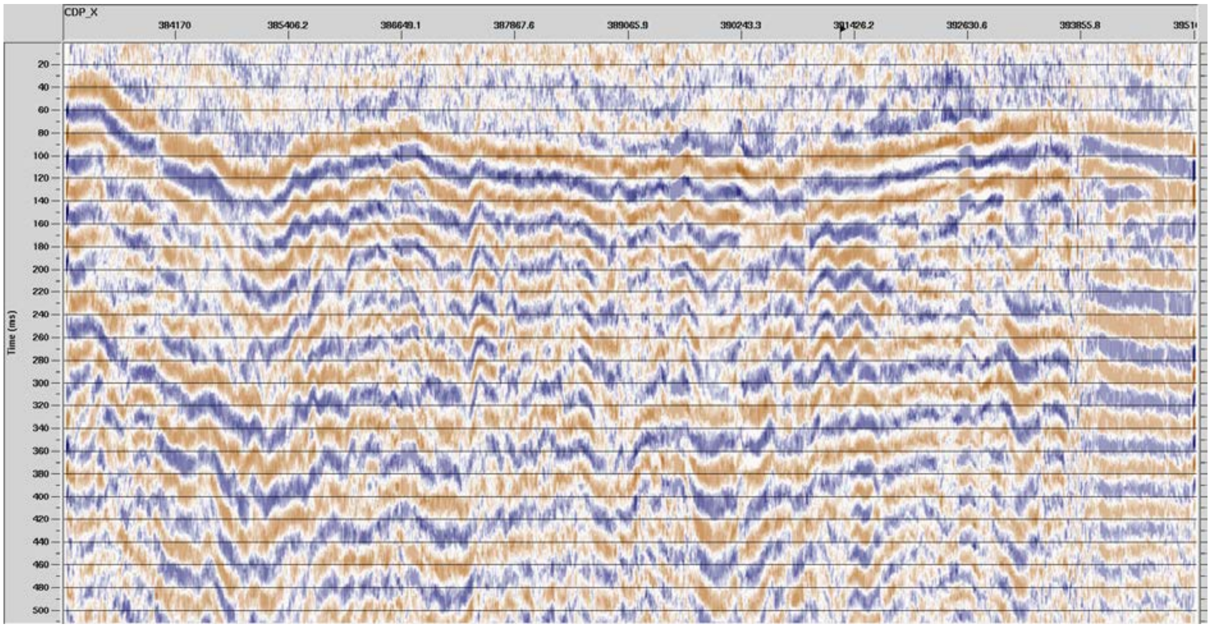

Figure 17. Line 11GA-LL1 - A simple refraction stack for the offset 2900 m and velocity 2500 m/s.

Multiples

A strong shallow multiple event is present in the data at approximately 250-300 ms shown by the blue arrow on Line 11GA-LL1 (Figure 18). It can be clearly seen especially at the right part of the line (CDP 2750-3401). The cause of the multiple reflection is probably due to the hard limestone formation in the shallow overburden.

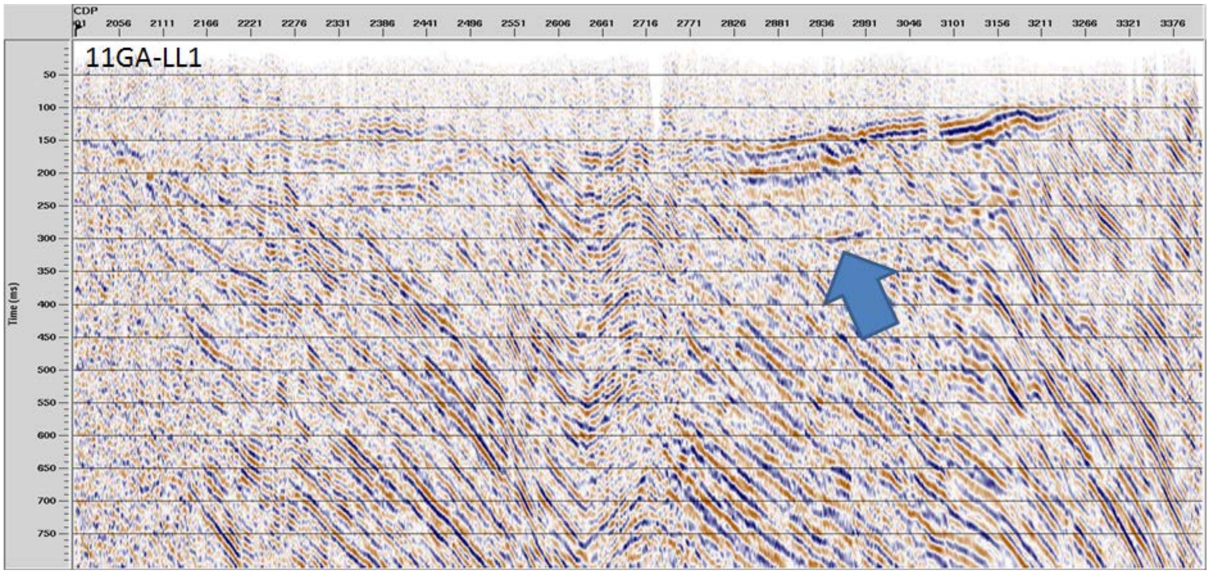

Figure 18. Line 11GA-LL1 - an example of a shallow multiple reflection, probably due to the hard limestone layer in the near surface (blue arrow points to the event).

Variable ground surface coupling

A significant issue at the SW Hub site seems to be variable ground coupling due to spatial changes in near surface conditions (see, for instance, Figure 2&3). Figure 19 is a stacked section which was produced using a processing flow without AGC. The image amplitudes are seen to change drastically along the line, probably due to poor coupling of sources and receivers along the lines from hard to soft surface conditions.

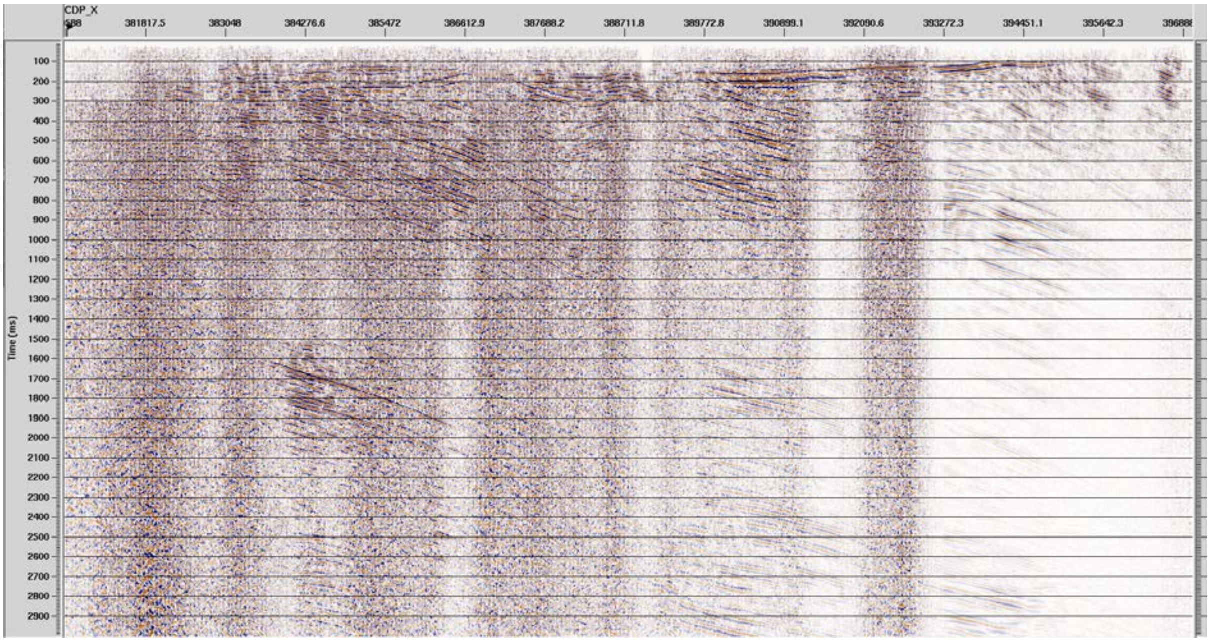

Figure 19. An example of CDP stack (Line 11GA-LL1) with non-AGC processing. No amplitude corrections were applied to compensate variable ground coupling conditions. The amplitude variations are likely caused by strong changes in ground surface coupling conditions along the line.

Out of Plane Events

Due to crooked line geometry and complex 3D geological structures including faults, ‘out of plane’ reflection events seem to be present in the 2D seismic data. In order to examine this further we produced a series of CDP stacks with fixed velocities. Figure 21 shows two stacked sections for velocities 2900 m/s and 3100 m/s. The blue arrows mark seismic events that have the same amplitude as events above them. For example, in Figure 21 (a) the event at 1.6 s has the same amplitude as the event from 0.8 s (the top of the Lesueur formation).

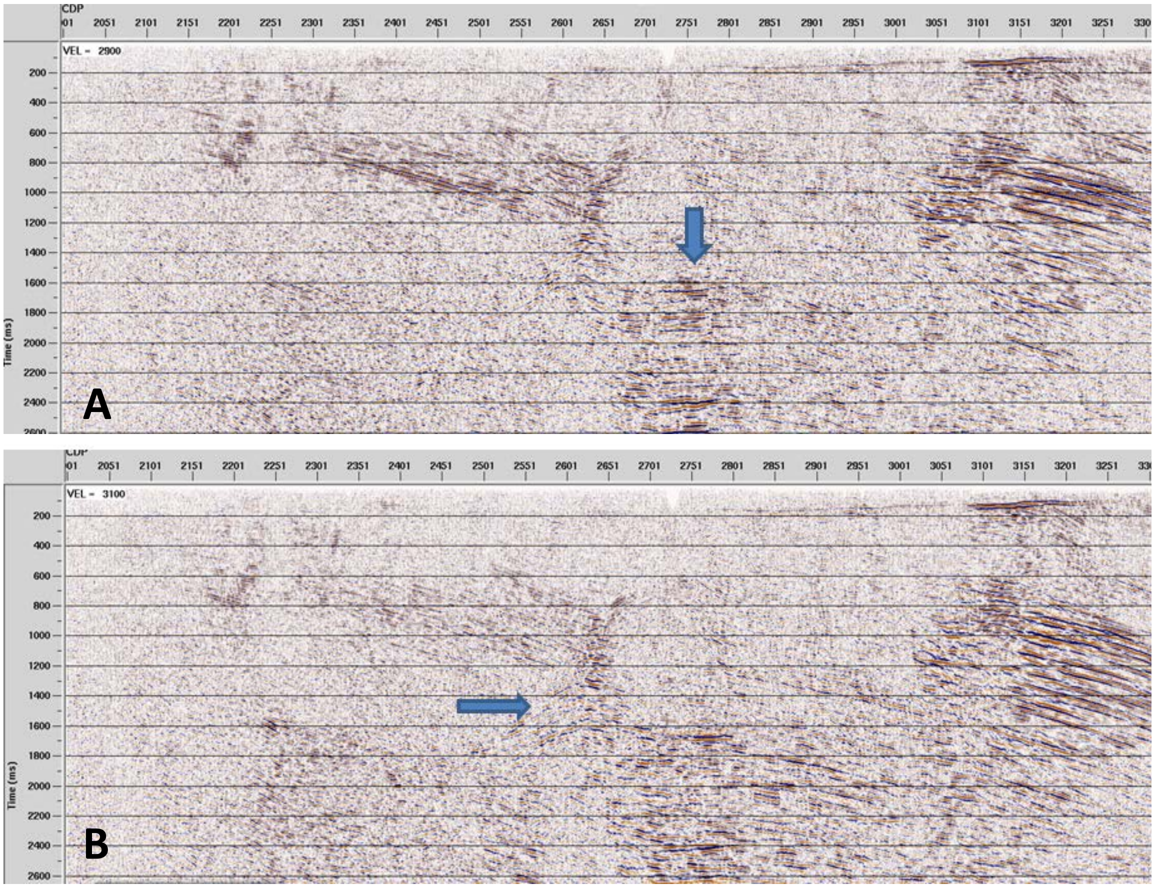

Figure 20. Line 11GA-LL1 – An example of out of plane events (blue arrows) for the velocities (a) 2900 m/s and (b) 3100 m/s.

Crooked Line Geometry (Line 11GA-LL1)

Crooked line geometries can cause false geological structures and velocity anomalies, as shown in Figures 21-22 (indicated by the red circle and blue arrow respectively), if processing does not correctly take into account the 3D angular relationship between the shots, receivers and the reflection surface.

.

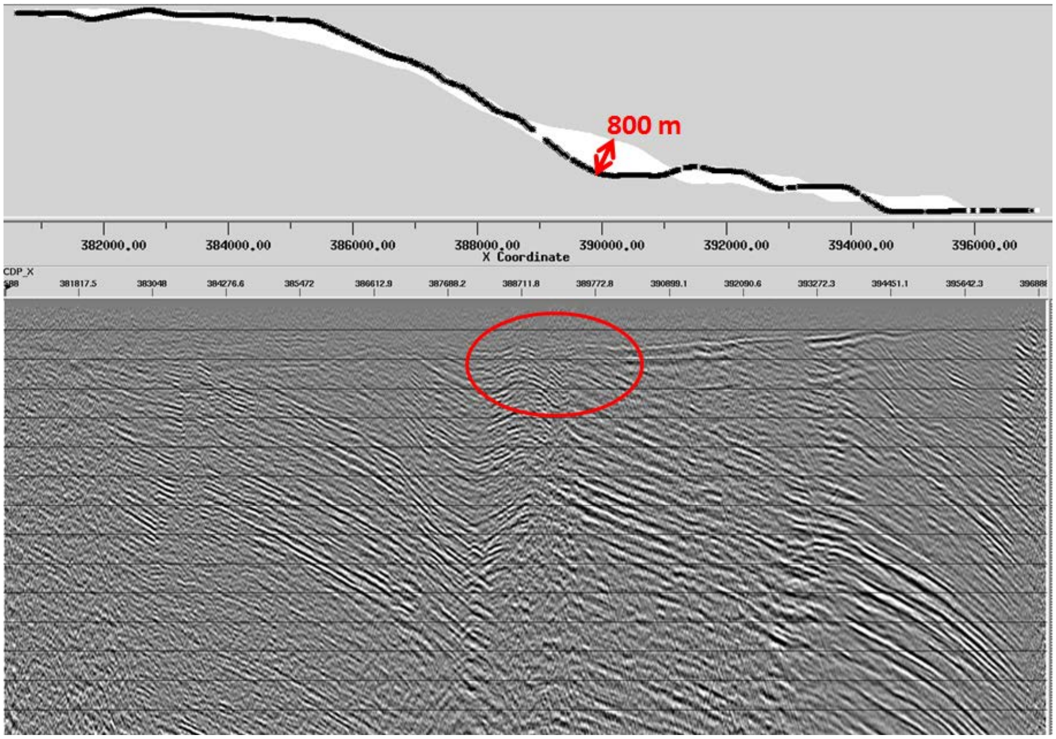

Figure 21. Line 11GA-LL1 – circled area in image corresponds to the most crooked part of the line and is probably a false structure.

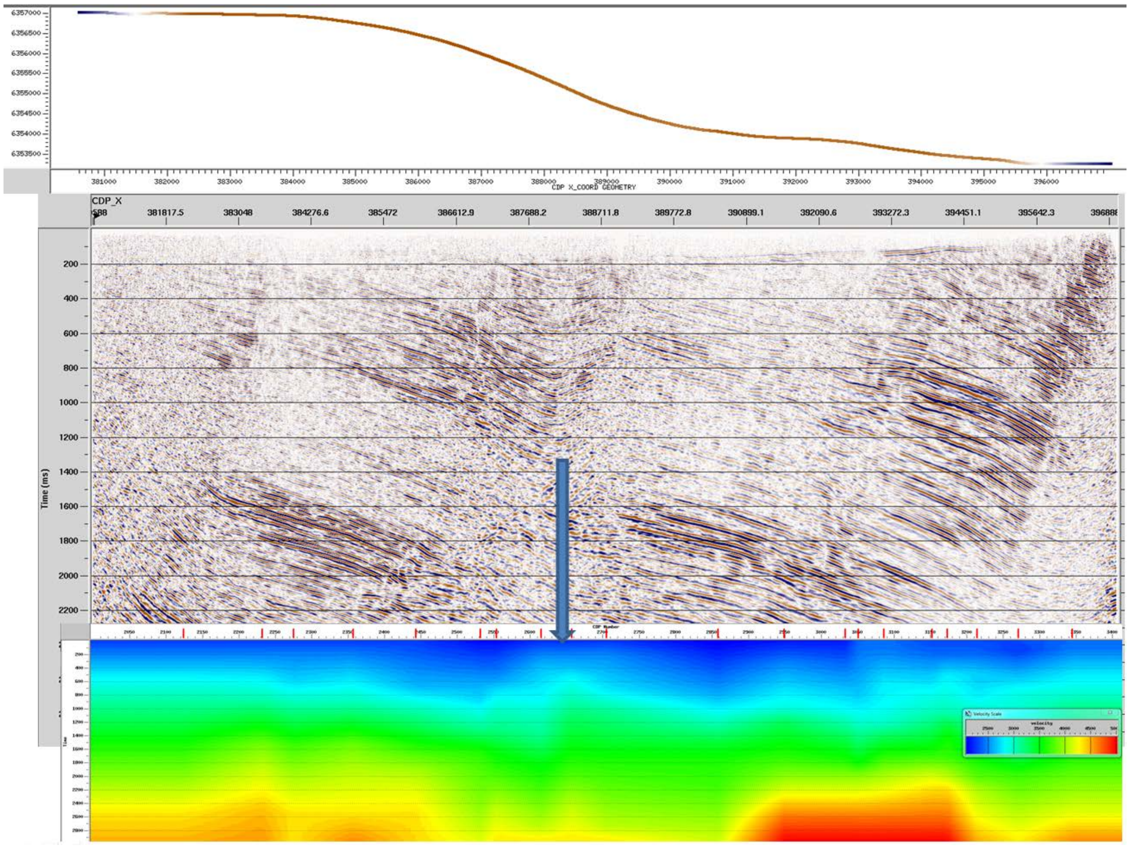

Figure 22. Line 11GA-LL1 – blue arrow corresponds to (probably false) image structure and RMS velocity anomaly in of the most crooked part of the line.

2.3. Velocity structure in the shallow part of the section from diving wave analysis

Studying the shallow part of the section is important as it can provide information which can be used not only for seismic data acquisition design and processing but also for geological interpretation of features related to modern tectonics. Existing 11GA-LL 2D seismic data provides relatively poor quality imaging of the near surface structure from reflection data processing. One way to get additional information about the shallow structure is to use refracted/diving waves.

In this study we utilise diving wave analysis using a Wichert-Herglotz integral. This technique, originates from works by Slichter (Slichter 1932), who adopted this method from global seismology. One of the principal limitations of the method is that is assumes a monotonic increase of the interval velocity with depth. We use the approach described in (Greenhalgh and King 1980) to derive velocity at the maximum penetration depth for an individual ray.

First breaks were picked for 11GA-LL2 for the entire offset range, after semi-automated corrections and filtering we applied 1.5 D Wichert-Herglotz travel-time inversion. Figure 23 shows the result of the inversion.

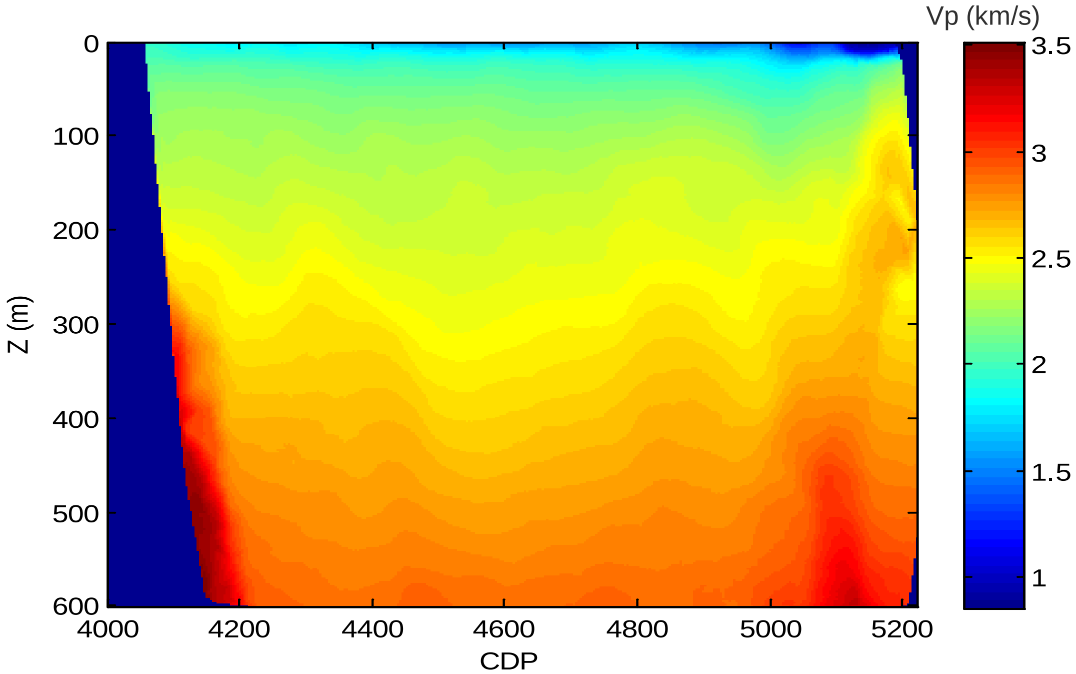

Figure 23. Line 11GA-LL2. Result of 1.5D Wichert-Herglotz travel-time inversion.

The velocity section was converted to time domain and compared to the migrated section obtained through CDP data processing (Figure 24).

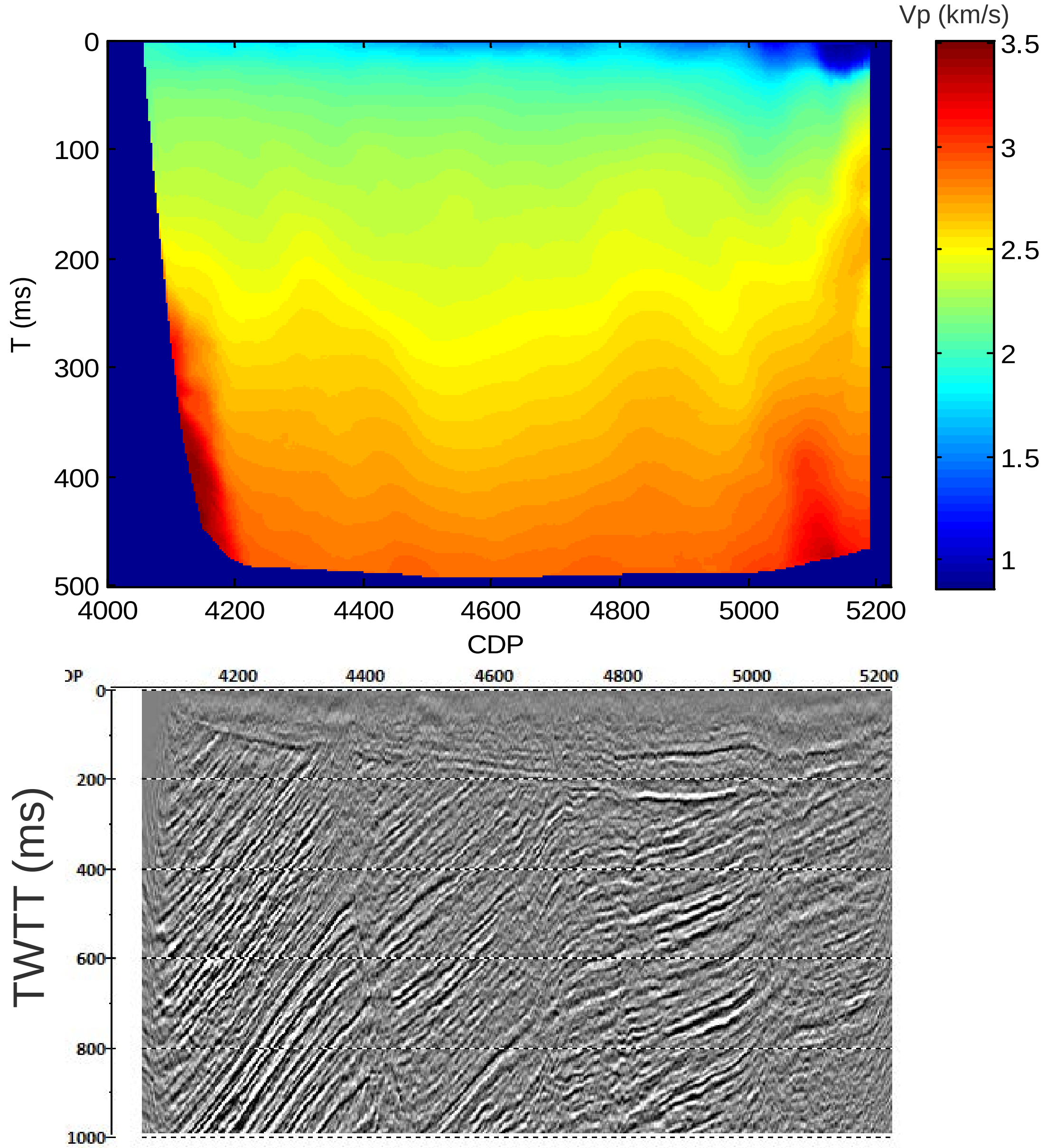

Figure 24. Line 11GA-LL2. Result of 1.5D Wichert-Herglotz travel-time inversion in time domain (top) compared to migrated section (bottom).

We observe a good agreement between the general subsurface structure (especially the location of the faults) seen on the seismic reflection section and velocity model from the 1% travel time inversion. Large offsets available for the existing survey allow us to obtain a velocity model for up to ~500 m depth. The other important observation is that one can see some indication of faulting as shallow as 100 m (100-150 ms) deep.

2.4. Pseudo 3D processing and pre-stack time Kirchhoff migration (PSTM)

Pseudo-3D imaging of 2D seismic data can be achieved by prestack time (PSTM) or depth (PSDM) migration of a (crooked) line of 2D seismic gathers into a full 3D image volume, and then extracting an optimal 2D image from within the 3D volume. The benefit of this process is that out of plane reflections can be imaged into their correct 3D position within the full 3D image volume, as opposed to being imaged to incorrect locations within a single 2D image plane. However, this pseudo-3D process is still only partly accurate in 3D, since to properly focus the image at the true reflection points within the full 3D image volume, a full crossline data aperture as can only be provided by full 3D seismic data acquisition is required.

Pseudo-3D time-domain PSTM processing of the 2D seismic dataset involves a number of key steps that are discussed in more detail in the following sections (pseudo-3D PSDM results will be discussed later). Two segments of line 11GA-LL1 were processed, within a 3D binning grid.

2.4.1. 3D Binning

3D binning of seismic data was computed with a bin size 12.5mx12.5m. This small bin size results in a small nominal fold coverage, but with trace density, large enough to have satisfactory PSTM results.

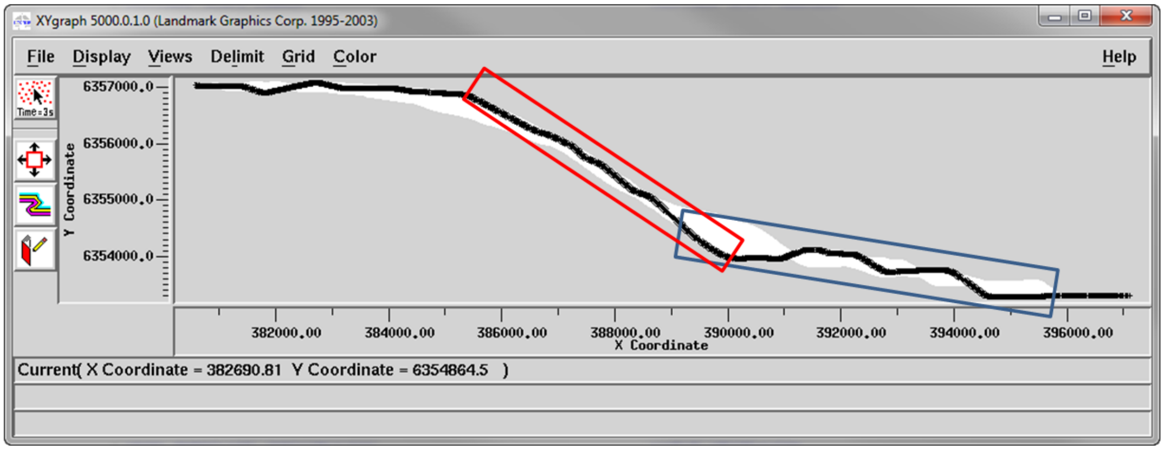

Current(X Coordinate = 382690.81 Y Coordinate = 6354864.5   )

🟦 L1.13D: survey azimuth 98.5 deg; bin size 12.5x12.5m

🟥 L1.23D: survey azimuth 122.34 deg; bin size 12.5x12.5m

Figure 25: Midpoint scatter of processed survey

The following Figure 26 shows fold coverage and offset distribution of line segment L1.1.3D. The crossline size of 800m would be large enough accommodate all actual CMP points.

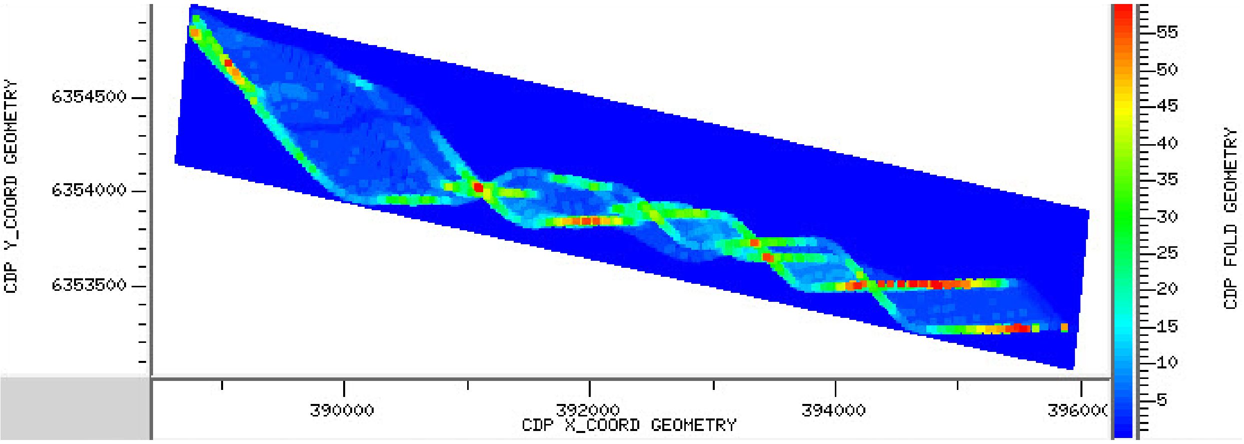

Figure 26. Line segment L1.1.3D fold map

Figure 27 shows fold coverage and offset distribution of line segment L1.2.3D. The south partof the cube is overlapping with segment L1.1.3D

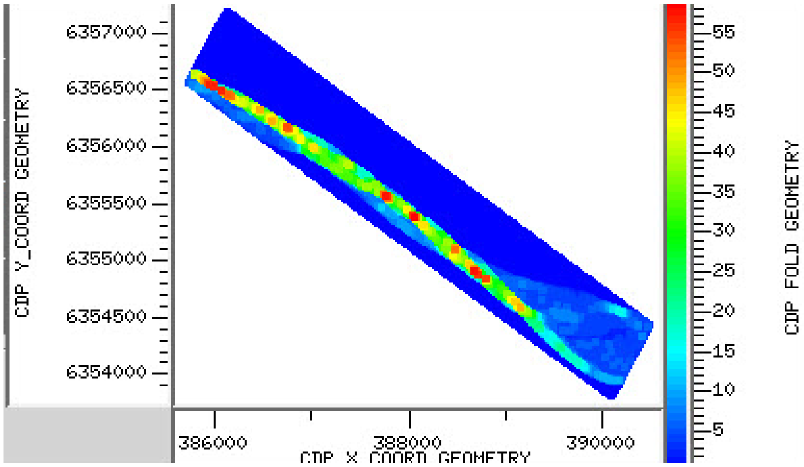

Figure 27. Line segment L1.2.3D fold map

2.4.2. Velocity Analysis and PSTM

An initial single velocity function was used to migrate the 2D dataset, after which, the final velocity analysis was performed on the following 3D grid.

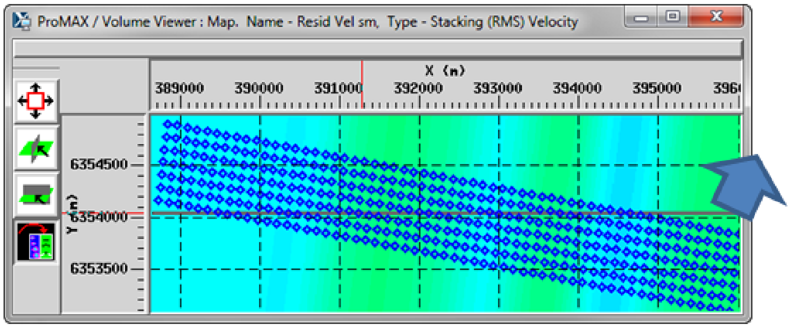

Interpolated velocity positions

Inline
increment
direction

Figure 28: Line segment L1.1.3D, velocity analysis grid

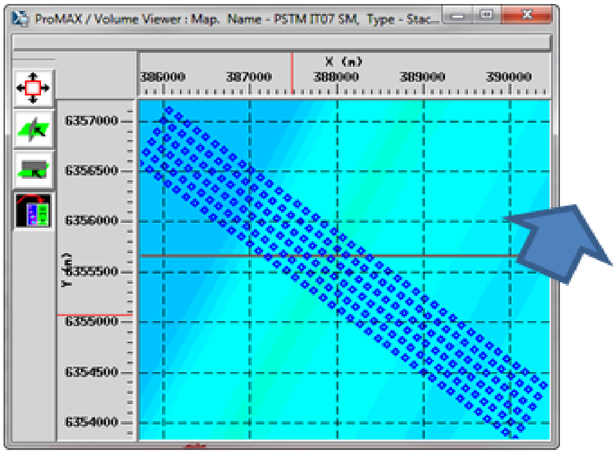

Interpolated velocity positions

Inline
increment
direction

Figure 29: Line segment L1.2.3D, velocity analysis grid

The full processing flow is outlined in the table below. The pre-processing sequence used in this effort is slightly different from the one used before. As here we focus on structural aspects of imaging only a short-window AGC was applied.

Table 4: Pseudo-3D Processing Flow Chart

1. **3D binning and geometry**
2. **Elevation static**
3. **Quality control (QC) of the elevation static solution (on shot records, every 20th shot)**
4. **Tests for: amplitude compensation, band-pass filter, Multi-channel filtering (F-K/τ-p), autocorrelation and deconvolution**
5. **Window design for amplitude compensation and deconvolution**
6. **Surface wave noise attenuation (apparent velocity of 2100 m/s, frequency mix in the range of 1 – 80 Hz)**
7. **Application of deconvolution**
8. **Bandpass filter (Butterworth, in the source bandwidth range)**
9. **Derivation of single velocity function**
10. **Brute stack**
11. **Computation of surface consistent residual reflection statics (delay time based) & application of residual statics**
12. **Preliminary Prestack Kirchhoff Time Migration**
13. **Second pass velocity analysis**
14. **Final Prestack Kirchhoff Time Migration**
15. **Velocity Analysis for further refinement of stacking velocity**
16. **Stack**
17. **Post stack processing**

2.4.3. Pseudo-3D PSTM final sections

Final PSTM Sections of both segments of line 11GA-LL1 are displayed in the Figures 29-30 bellow. The relative location of pseudo-3D volumes and arbitrary lines are shown in Figure 30.

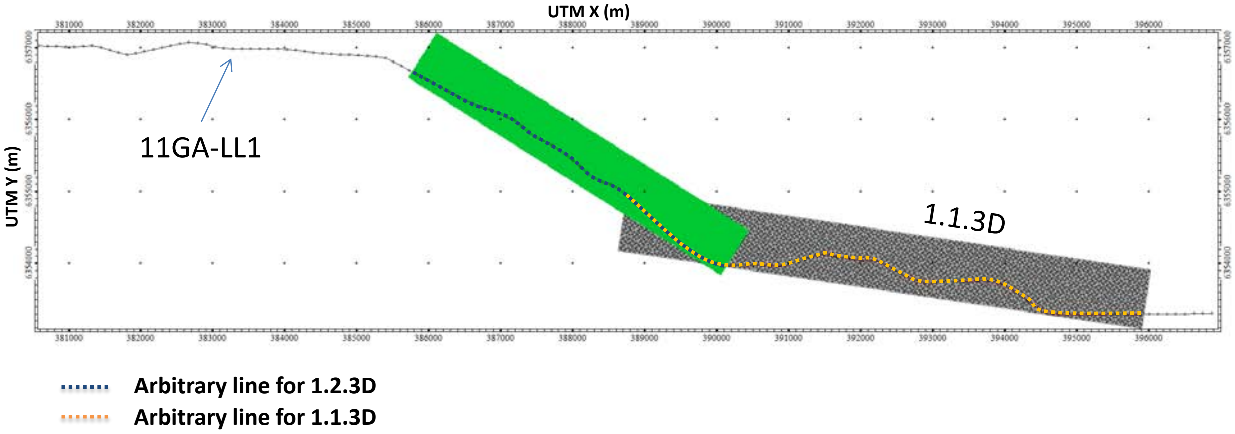

Figure 30. Relative location of 11GA-LL1 line, pseudo-3D volumes and arbitrary lines

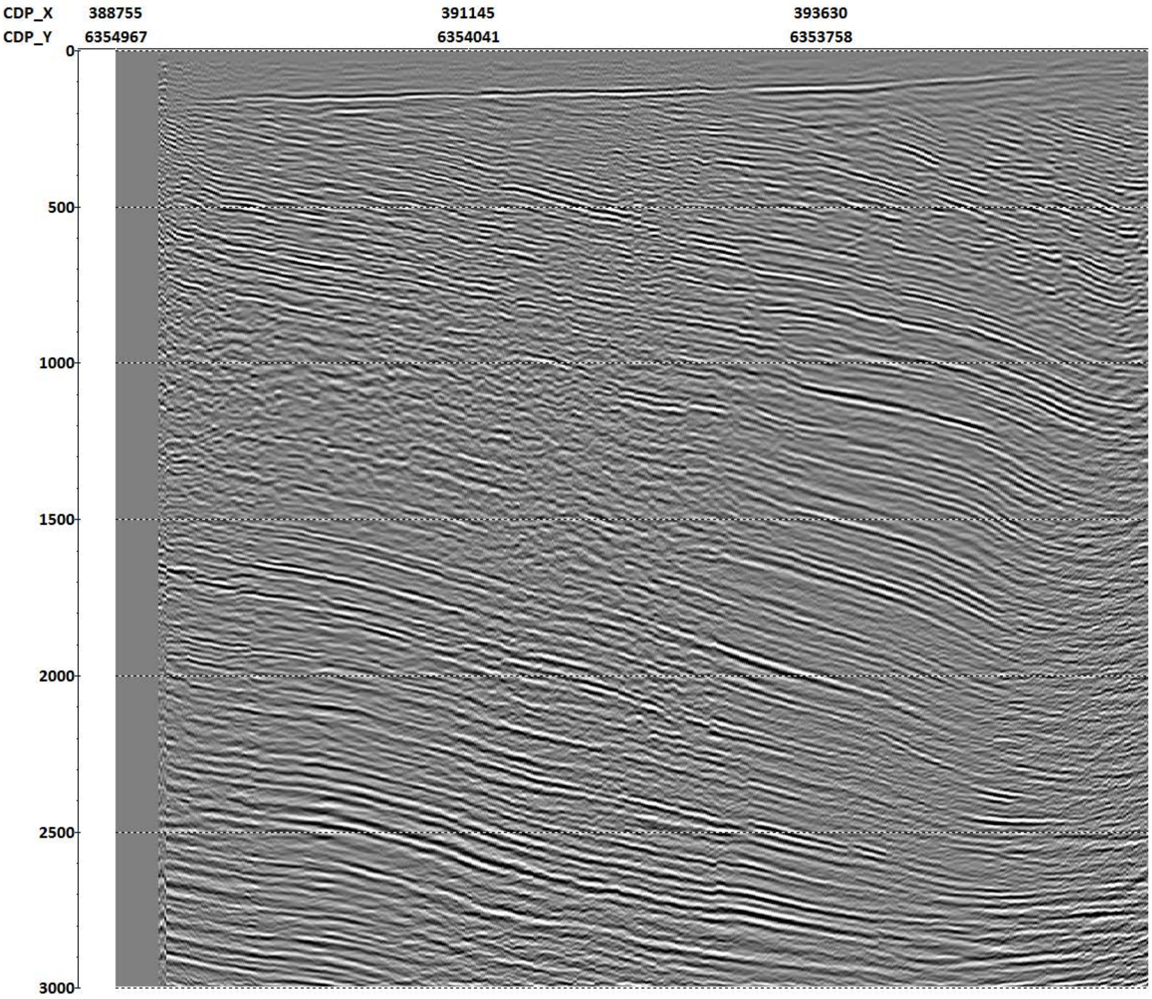

Figure 31. Arbitrary line from 1.1.3D following the 11GA-LL1 2D line track.

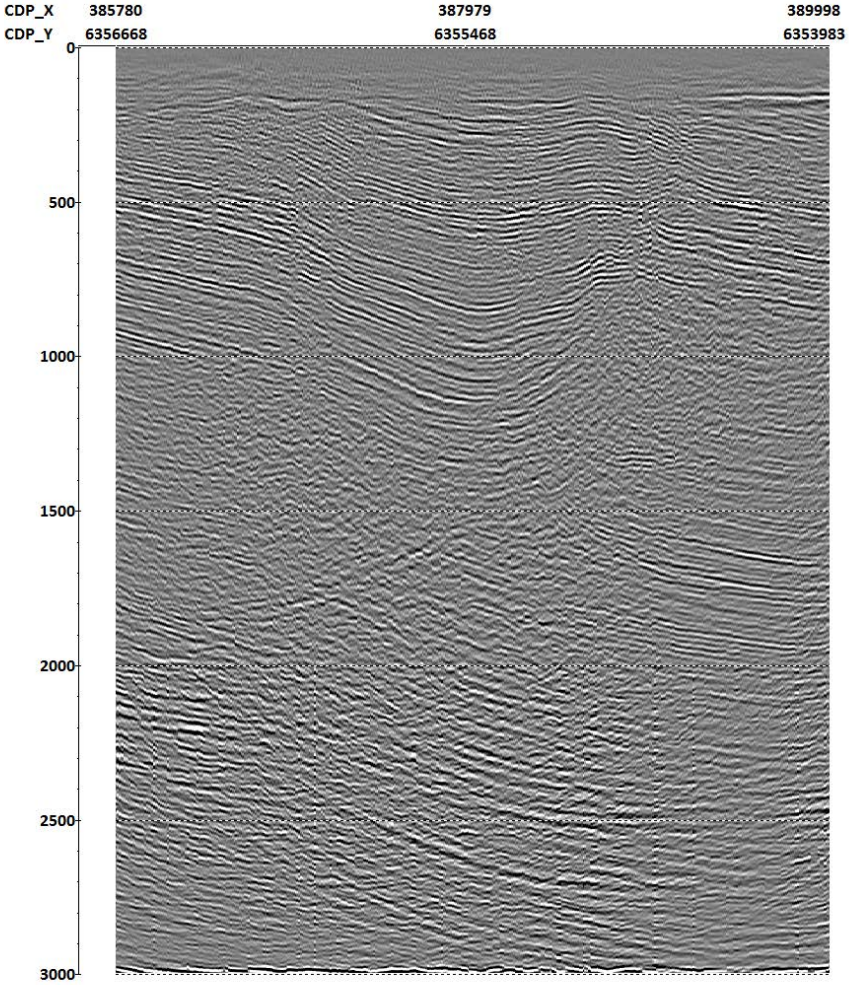

Figure 32. Arbitrary line from 1.2.3D following the 11GA-LL1 2D line track

Application of pseudo-3D prestack time migration as shown in Figures 29-30 can be seen to partially compensate for the crooked line geometry, by improving the continuity of the imaged reflectors, and also the vertical and lateral resolution. Additionally, the pseudo-3D PSTM process appears to improve fault definition (see Figure 30 between 1500-2000 ms for example).

2.5. Pre-stack depth migration of the SW Hub 2D Seismic Data (PSDM)

Prestack depth migration (PSDM) is an advanced and computationally expensive imaging technique that can provide improved images compared to PSTM in the presence of strong subsurface geologic structure and/or strong spatial velocity variation. For such cases, PSDM provides improved images in which reflectors and faults are positioned more accurately both laterally and in depth, steeply dipping surfaces (such as faults) are better imaged, and high-resolution PSDM velocity analysis can improve images of weak or subtle reflections and small targets such as small-throw fault truncations. Since the SW Hub site appears to have complex subsurface structure and steep-dip faulting, we tested PSDM on the 2D seismic data to see if it could provide improved images compared to more conventional PSTM processing.

The initial prestack depth migration test for the 11GA-LL1 2D seismic dataset was to assume a perfect 2D acquisition straight-line geometry, as was done previously for the PSTM case. As discussed earlier, this approximation assumes that seismic data are acquired along a straight line with no out-of-plane reflections, and is a poor assumption for imaging reflectors (especially shallow) where the crooked line geometry deviates significantly from a straight line. Nevertheless, it represents a good first-pass attempt to see how well PSDM compares with the 2D prestack time migration (PSTM) images, and whether PSDM improves the image of geologic structure.

The pre-processed data set used for PDSM was similar to that used for the PSTM tests. A key difference was that we applied an additional processing step to remove the vertical streaking evident on the shot records (Figure 33, left panel). These irregular amplitudes cause fairly strong impulse-response noises to appear in the PSDM test images. We removed these artifacts by applying a trace-balancing procedure to equalise amplitudes within and across shot records, and then divided the result by the smoothed envelope of the original record to approximately restore original amplitudes. The right panel of Figure 33 shows the trace-balancing results for shot record 580. Note that the amplitudes of the underlying hyperbolic reflectors are fairly consistent between the two panels.

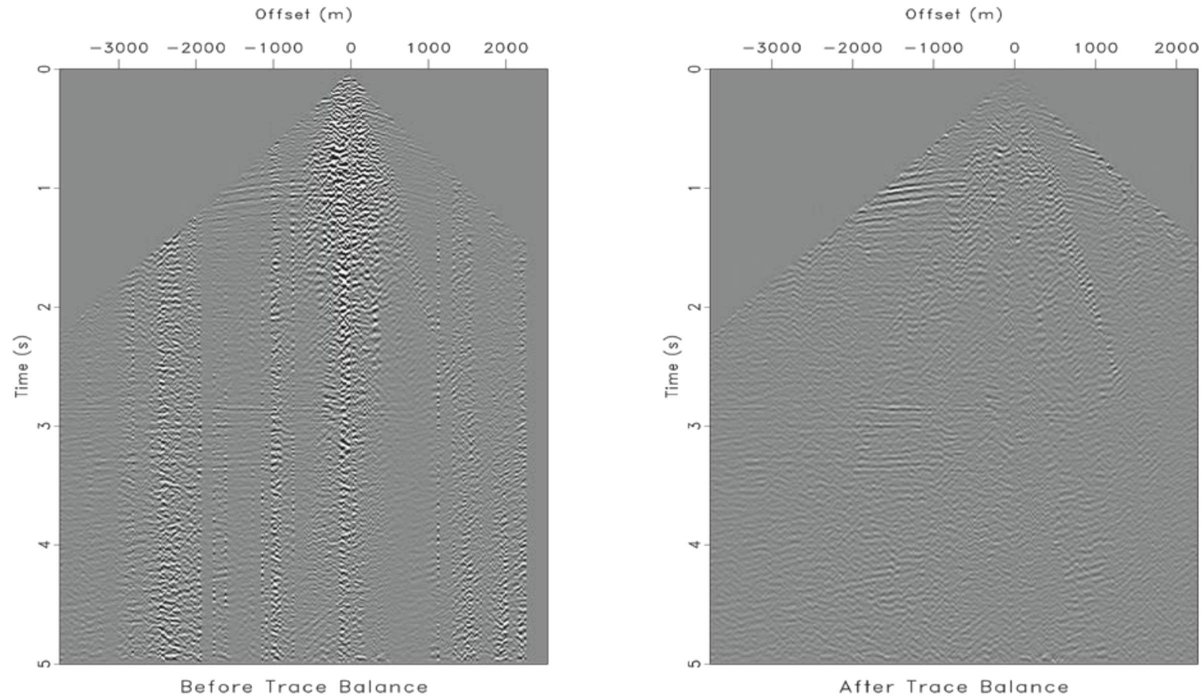

Figure 33. Shot record 580 before (left panel) and after (right panel) applying trace balancing.

Before performing PDSM we first generated a background P-wave velocity model using information available from preliminary work on the Harvey-1 borehole. We constrained the near surface (0-1.2 km) using P-wave velocities from the VSP analysis. Velocities at intermediate depths (1.2-3.2 km) were extracted from the P-wave borehole sonic log, while those of the deeper section (3.2-7.0 km) were extrapolated from the sonic log trend between 2.8-3.2 km that showed an asymptotic behaviour to roughly 5.0 km/s. Figure 34 shows the background V(z) velocity-depth trend used for migration, which formed the basis of our initial 2D PSDM velocity model.

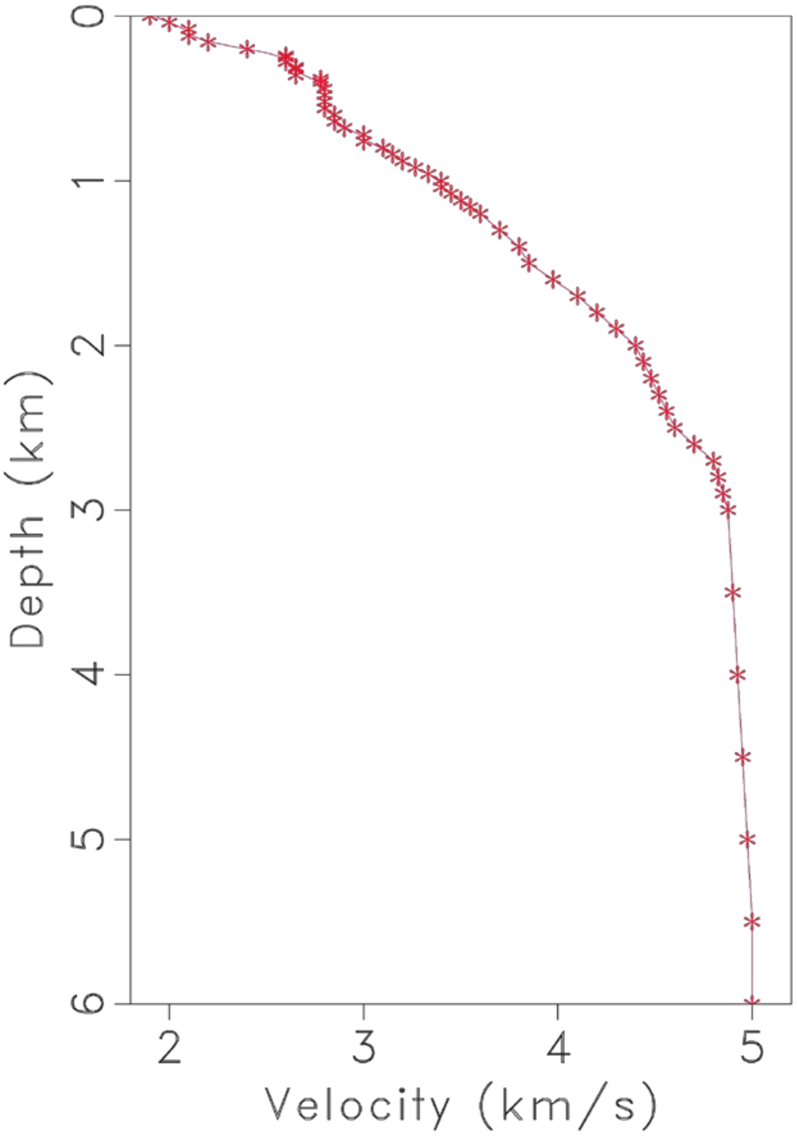

Figure 34. The V(z) migration velocity profile used as the initial background model for 2D and 3D PSDM.

We used a wave-equation PSDM algorithm to generate the 2D shot-record migration results. Data were first interpolated and regularised onto a regular mesh at uniform intervals as required for the wave-equation migration algorithm. Figure 35 shows the 2D PSDM depth image result using the velocity profile in Figure 34. The results are similar and somewhat improved compared to the 2D PSTM images; however, note that there are steep-dip reflectors newly present in the PSDM image that are likely to be enhanced fault plane reflections. See for example at location [x,z]=[7.0,3.0] km which is interpreted to be a major fault separating two faulted blocks of the Lesueur (with about 1km vertical displacement of fault throw), and at location [17.0,4.5] km which is interpreted to be the Darling Fault imaged at depth, beyond the east end of the 2D seismic line.

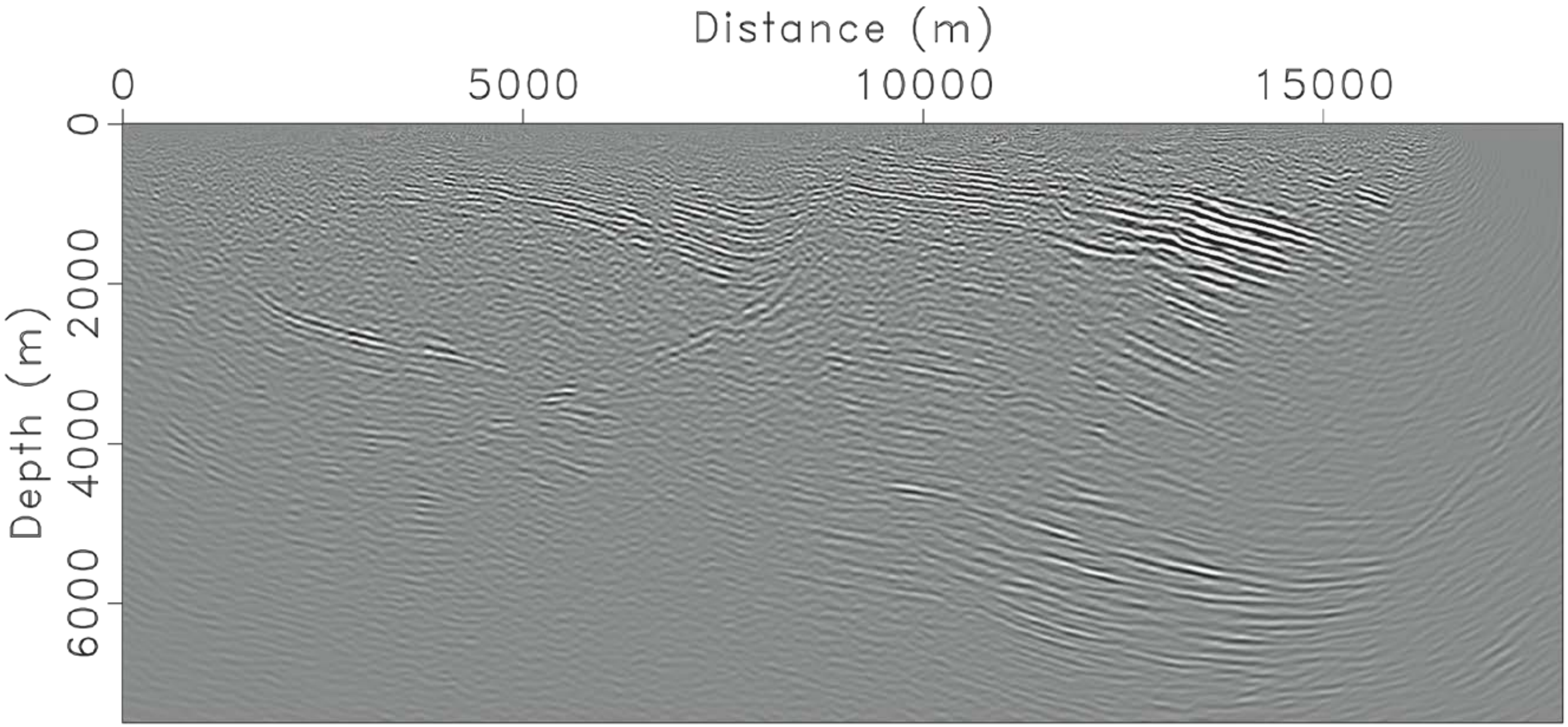

Figure 35. 2D PSDM image using the V(z) migration velocity profile of Figure 34

We also produced subsurface offset PSDM gathers through shifted wavefield correlations. These gathers are useful for examining velocity model accuracy because well-focused reflectors are a good indication of a correct velocity model, whereas poorly focused reflectors suggest velocity model errors. To examine this we migrated the dataset with the initial baseline velocity model with scaling factors applied ranging between 0.9 (ie. 90%) and 1.1 (ie. 110%) at increments of 0.02 (2%). Figure 36 shows a set of 11 gathers extracted from the depth image volume at 14.25 km. A `bullseye' at 100% scaling factor (along horizontal axis) indicates that the velocity profile in the vicinity and above this location are close to the correct values.

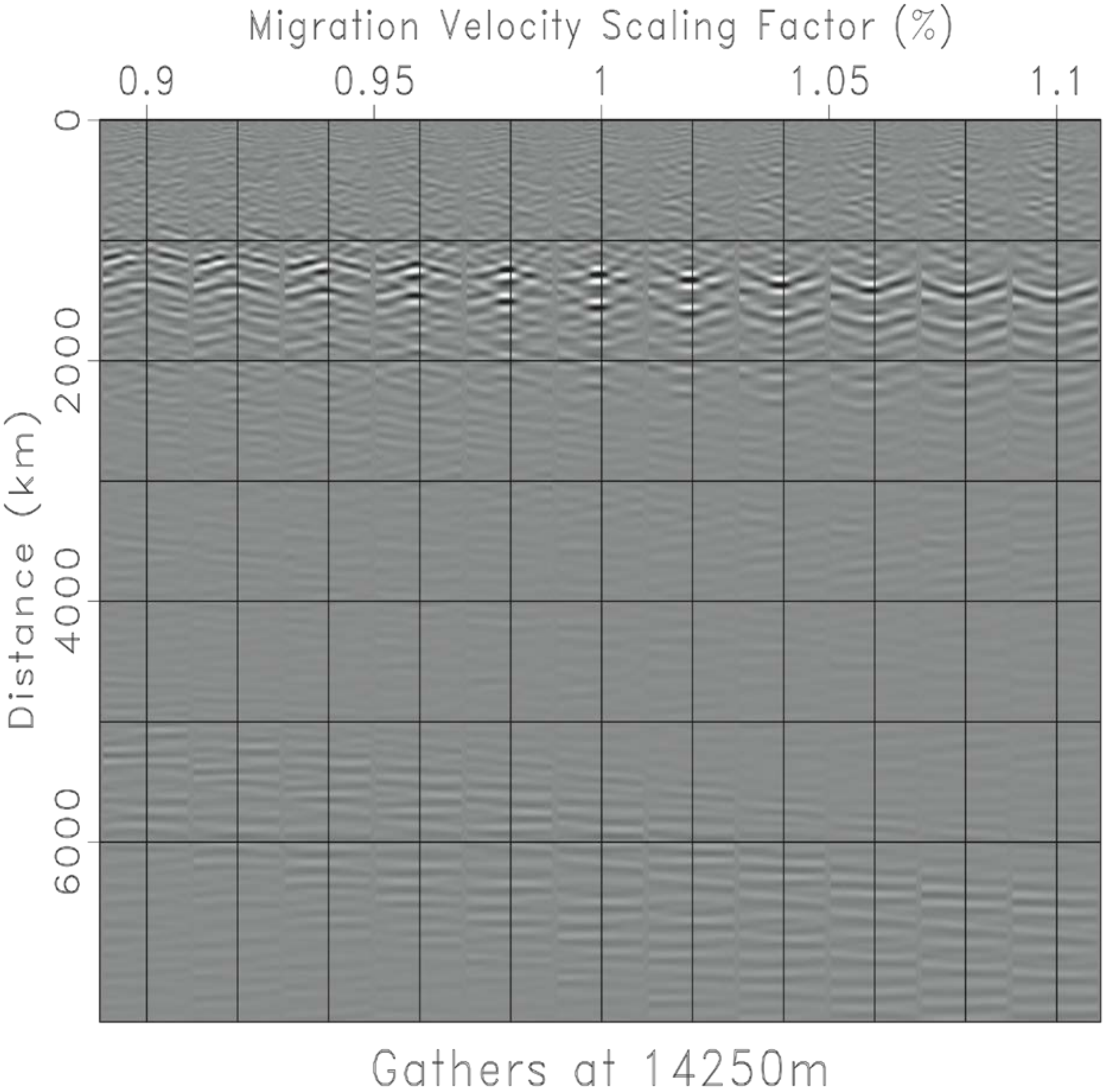

Figure 36. A sample focusing panel extracted at x=14.25 km. The horizontal axis shows the concatenation of 11 offset gathers for various multiplier factors of the velocity profile. The gather at this location is well-focused at 100% scaling indicating the velocity field is fairly accurate in the vicinity of this location.

Subsurface offset gathers also are useful for velocity model updating. We applied 10 iterations of PSDM migration velocity analysis using an image-domain tomography algorithm in order to optimise reflector focusing. Figure 37 shows the result of this analysis, which indicates that eastern portions of the line between 9-15 km require a slower migration velocity than those toward west between 0-9 km. We incorporated this update to form a *v(x,z)* velocity model, which we used to regenerate the image shown in Figure 38. One interesting new observation is that this image appears to show a subtle shallow angle fault imaged stretching from approximately [9.0,2.0] km to [12.5,0.5] km.

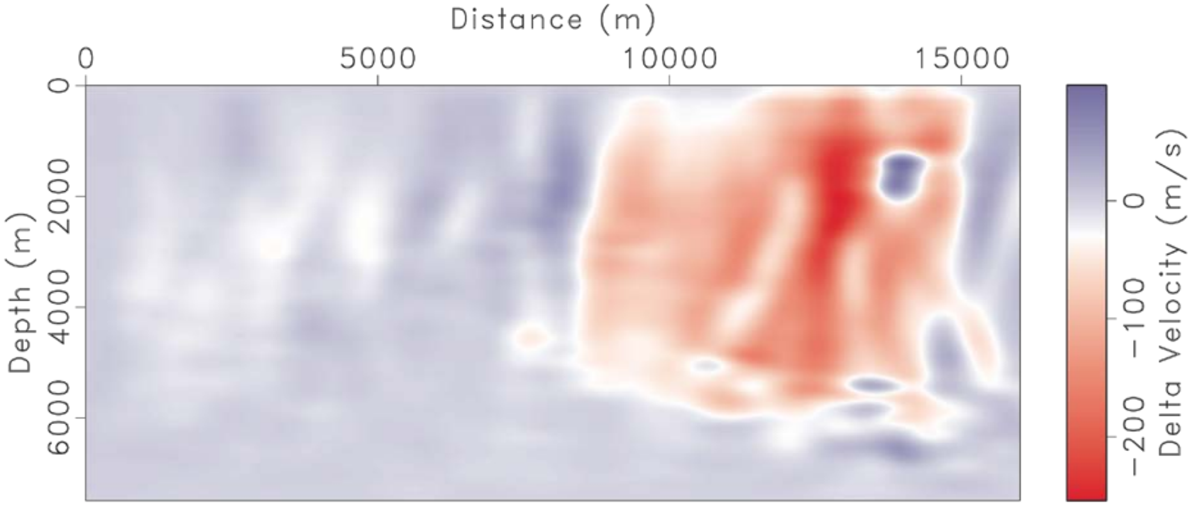

Figure 37. Velocity model update from ten iterations of image-domain tomography.

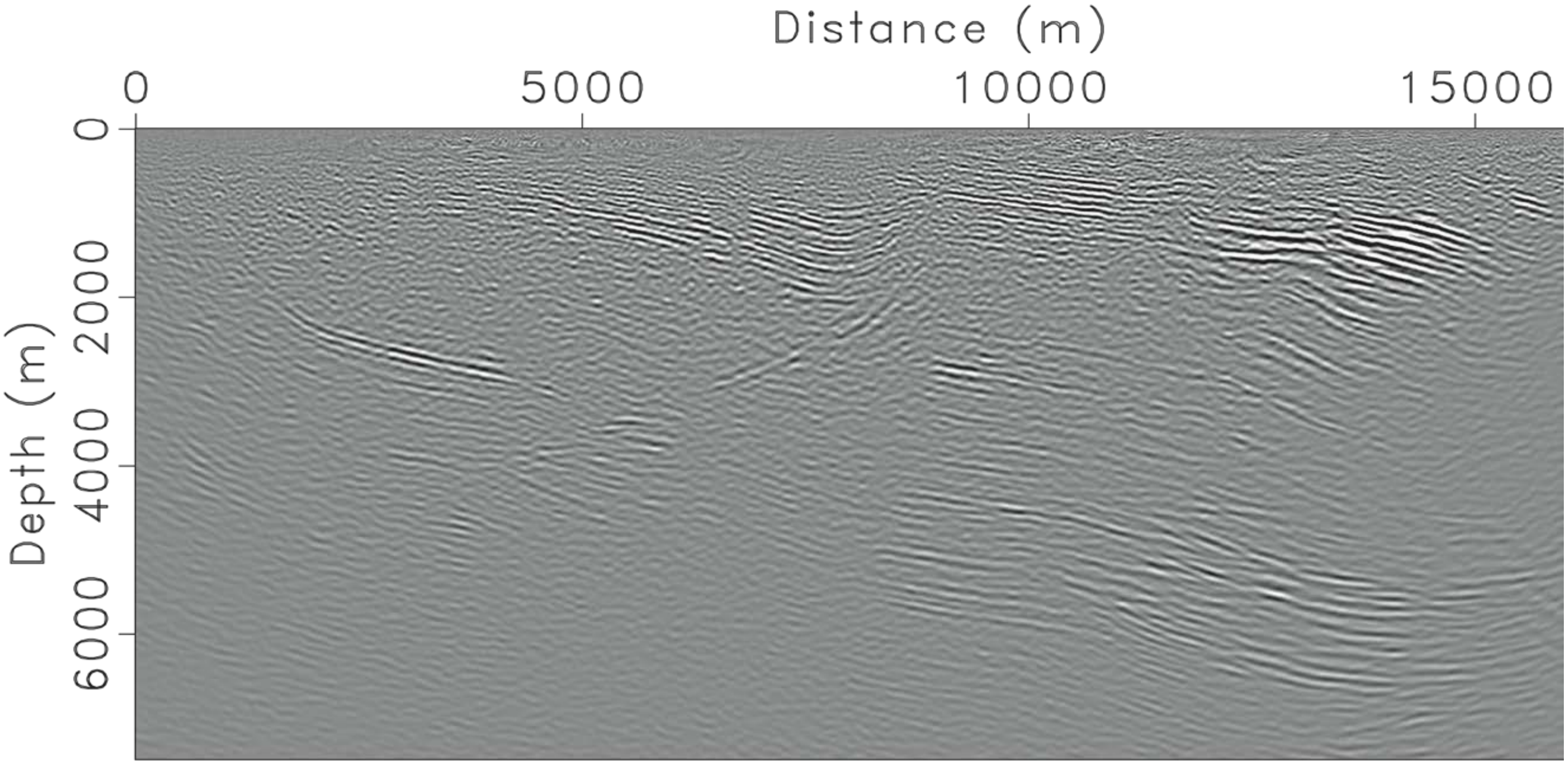

Figure 38. 2D PSDM result after incorporating the velocity update in Figure 37

3D prestack depth migration

Because 3D PSDM better honours `true' wave-propagation paths and amplitudes than a 2D approximation, we applied a full 3D PDSM to the 2D crooked-line data to see whether there were any imaging advantages. Our 3D migration strategy involved three steps: interpolate the 2D crooked-line data into regularly sampled 3D shot profiles; perform 3D shot-profile wave-equation migration using a 3D version of the $v(z)$ migration velocity model, and stack the results into the global 3D cube; and extract a 2D profile from the full 3D image cube along the acquisition path.

Figure 39 shows the 2D line extracted from the 3D migration volume. We note that the interpreted Lesueur fault-block fault reflector at point [x,z]=[7.0,3.0] km is crisper than in the 2D image (Figure 38) and helps supports with greater confidence the interpretation that this is a true fault-plane reflection. The reflector packages at distances >9 km and between 2-6 km depth are also more continuous than those in Figure 38. Based on the imaging improvements after the 2D PSDM image-domain tomography velocity analysis, we assume that applying this type of velocity-updating algorithm in 3D would be similarly beneficial; but the required computational time would only be worth applying to a full 3D seismic data set (in the future).

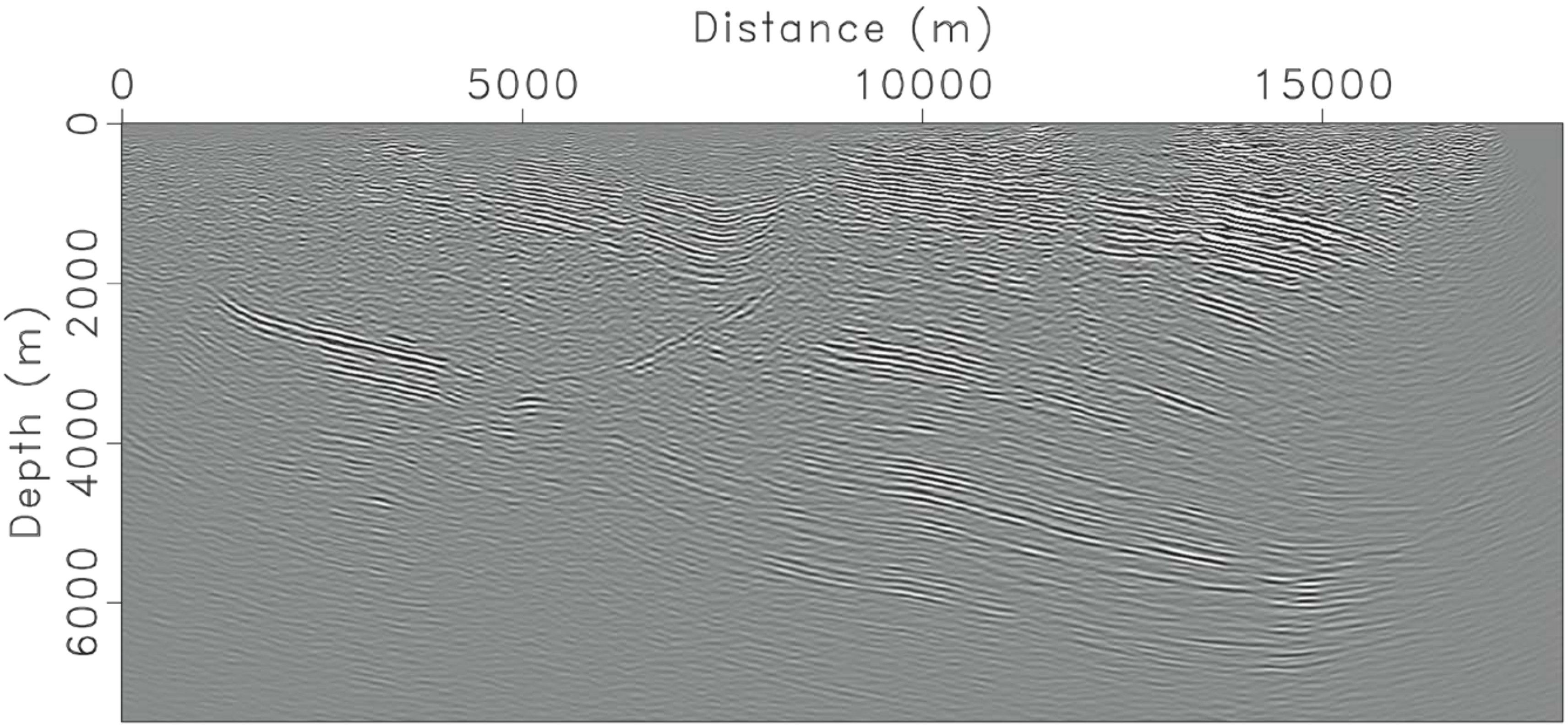

Figure 39. Extracted 2D image from 3D PDSM image volume along the acquisition line.

For comparison purposes, Figure 40 presents a small section of the 2D image extracted from the 3D PDSM volume approximately converted from depth back to time (centre panel), the contractor 2D PSTM result (left panel), and the pseudo-3D PSTM migration (right panel). We note that most of the main reflectivity packages are similarly positioned. However, there are significant amplitude variations due to the different migration methods and post processing sequences applied.

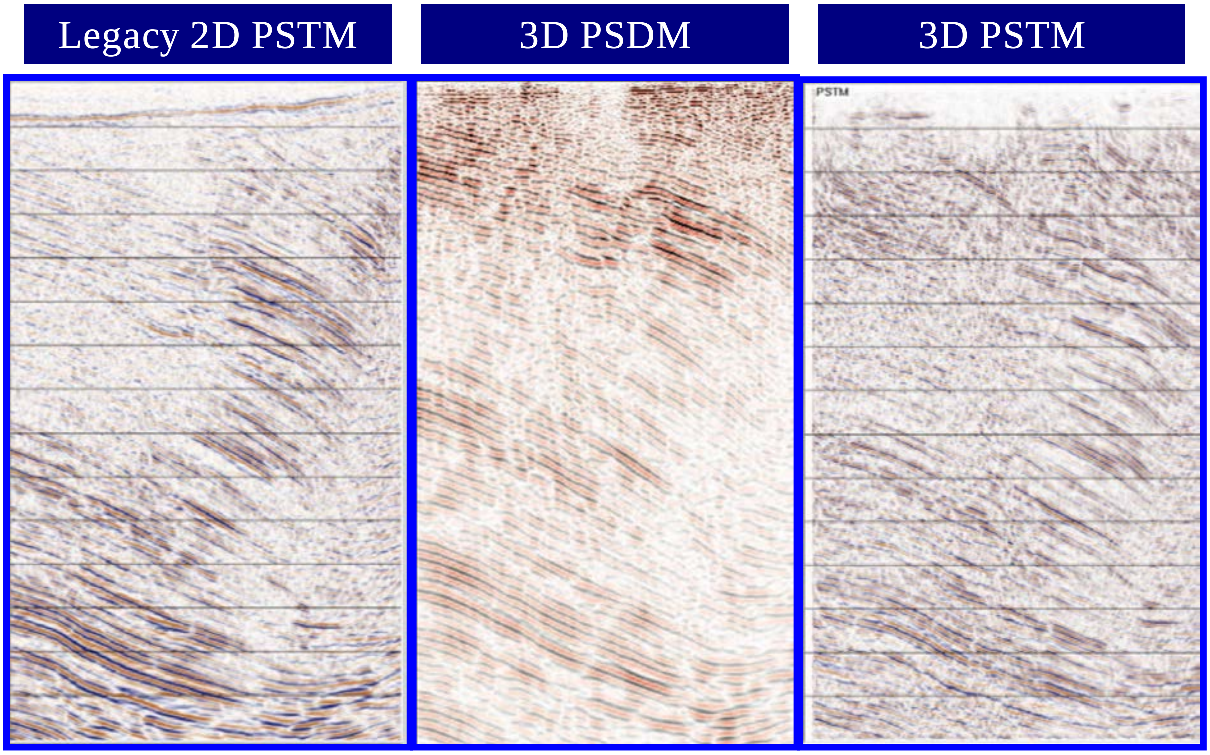

Figure 40. Comparison of 3D PSDM result (middle panel) with existing 2D PSTM (left panel) and 3D PSTM(right panel, one of the cross-lines, see Figure 31)

Our main findings from the PSDM tests are that prestack depth migration provides some image improvements compared to PSTM at the SW Hub site, especially for imaging steep-dip fault-plane reflections, which appear to be more numerous and at a wider range of angles than previously observed in PSTM images. We recommend that full 3D PSDM - with special emphasis on a high-resolution velocity analysis - should be applied to the new 3D seismic data to be acquired in 2013, to help better understand the complex structure and fault systems at the SW Hub site.

2.6. 3D acquisition recommendations

3D Acquisition Fold

- The 2011 2D seismic survey has a fold of ~140, resulting in reasonable image quality. Halving the fold to ~60 (i.e. ~2D_fold/2) for 3D seismic would probably give comparable 3D stacked data quality, so a 3D acquisition fold of 60 or higher is recommended. The 3D acquisition fold of 25 originally planned for the 3D acquisition is too low.

3D Source/Receiver line grid, min/max offsets:

- A 200 x 200 m grid gives an Xmin (the minimum offset which will present in the each bin) of 280 m, which means that we would be unable to image anything shallower than ~240 ms (~300 m depth, which includes the shallow unconformity). To image the unconformity, which is important for near-surface velocity analysis and processing corrections, we need an Xmin of ~150 m or less. Choosing a source brick pattern or slant shooting will help reduce Xmin, and also suppress acquisition footprint noise in the 3D images.
- An even more significant issue is the Xmax value, since the base of the Lesueur formation on LL2 is ~2.6-4.3 km depth. We strongly recommend that Xmax should be increased to at minimum 3 km, and preferably 4 km or more so that we have the possibility to do AVO/Inversion etc to seismically estimate reservoir properties and image CO_2 effects, and also to record more of the steep-dip fault reflections energy in order to make accurate images of large and small faults important for assessing the storage potential for the Lesueur, including the nearby Darling Fault. 3D seismic data recorded with maximum offsets of ~4 km is within acceptable mute parameters. Increasing Xmax to ~ 3km and keeping patch aspect ratio < 1.2 would require at least ~1600 channels.

Source effort:

- An orthogonal grid will create a strong footprint (noise) in the seismic data. It may be acceptable for a structural interpretation of a 3D seismic image but will complicate amplitude attribute analysis and quantitative interpretation, and will definitely affect 4D difference maps where the signal may be weaker than the footprint. A diagonal staggered source brick approach is recommended for consideration. This will also improve the offset-azimuth distribution.
- A larger source effort (combination of a larger number of synchronized vibroseis sources) can provide more signal down to the base Lesueur or deeper for improved imaging at depth.

Record length:

- We recommend a record length of at least 5-6 sec to ensure sure we record the steep dip energy which is required for accurate fault imaging.

Statics and near surface characterization:

- We recommend acquiring a well-sampled set of 3D up-hole times in order to help estimate a good near surface model for seismic processing (we’ve seen clear indications in the 2D seismic data that near-surface variability, and a lack of near-surface data, is causing significant data processing problems).

3. PROCESSING AND ANALYSIS OF ZERO-OFFSET VSP DATA IN HARVEY-1

The main goals of the GSWA Harvey-1 VSP data analysis are listed below:

- Estimation of P and S wave velocity profiles (for site characterisation and future seismic survey planning);
- Estimation of seismic attenuation (for site characterisation and 3D surface seismic processing flow design);
- Seismic to well tie: surface seismic and VSP to logs (reservoir and top seal)
- Estimation of shear-wave anisotropy parameters (for in-situ stress characterisation, fault seal, surface seismic processing flow design) using multicomponent shear wave velocity analysis.

The following relevant data became available to the project:

1. 3C ZVSP data acquired in GSWA Harvey-1 well covering the interval 24.5-1189.0 m. The data was initially provided as a VSProwes ACQ (Avalon Sciences Ltd., http://avalonsciences.com/) project but were later converted to SEG-Y format by Baker Hughes. Field report (Holt, 2012).
2. Log data, including density and velocity logs (XMAC tool data was processed only to P-wave velocities, shear wave velocities or anisotropy parameters were not derived, reliable data covers depths below 872 m MD (or 877.3 m TVD from the surface))
3. Well deviation survey
4. GSWA 2D seismic data

3.1. Data acquisition parameters

Zero-offset VSP (ZVSP) data was recorded in GSWA Harvey-1 well by Baker Hughes (Holt, 2012). The main recording parameters are provided in Table 5.

Table 5. VSP acquisition parameters

General Survey Parameters	
Survey date	19/04/2012
Well coordinates	385503.8 E, 6348945.67 N
Surface elevation	19.1 m above MSL
Reference level elevation	24.3 m above MSL
Receiver parameters	
Downhole tool	3C, ASL Geochain, 3 downhole shuttles

	Sensor: OYO SMC 2400-OMNI-15HZ
Receiver depth range (MD, m)	24.5 - 1189.0
Receiver step (m)	7.5
Record length	6000 ms
Sampling interval	1 ms
Source parameters	
Source position (from the well)	Easting 51.0 m, Northing 46.0 m
Source reference elevation	19.1 m above MSL
Source depth below SRE	2.0 m
Source type	Airgun in a steel lined pit (3x3x3 m), 2x200 in^3, bolt, pressure 2000 psi
Monitor	MP8 above source, distance from source 0.5 m
Source control system	RSS-1
External delay	4 ms

Figure 41 shows the VSP survey location scheme. Well track is shown only for the VSP receiver depth range, the well does not deviate significantly from the vertical direction for this depth range.

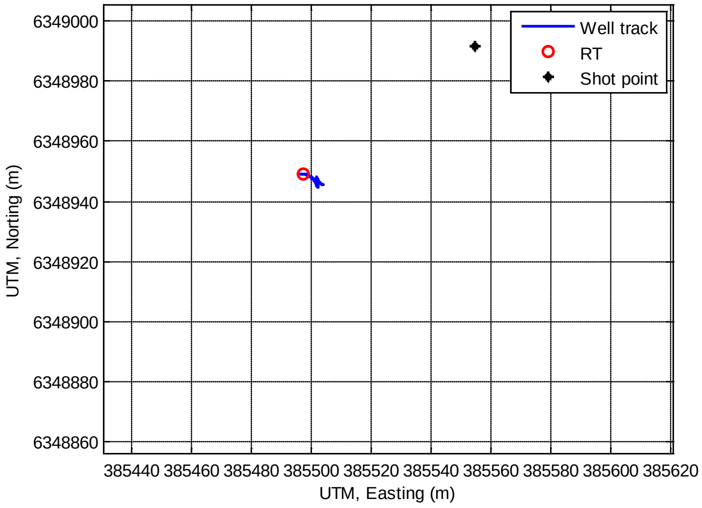

Figure 41. GSWA Harvey-1 VSP survey location scheme (well track is shown only for the VSP receiver depth range).

Several shots were recorded for each receiver interval (Figure 41), the actual number varied from 5 to 15. The greater number of shots for the bottom part of the borehole is caused by source instability during the first part of the survey.

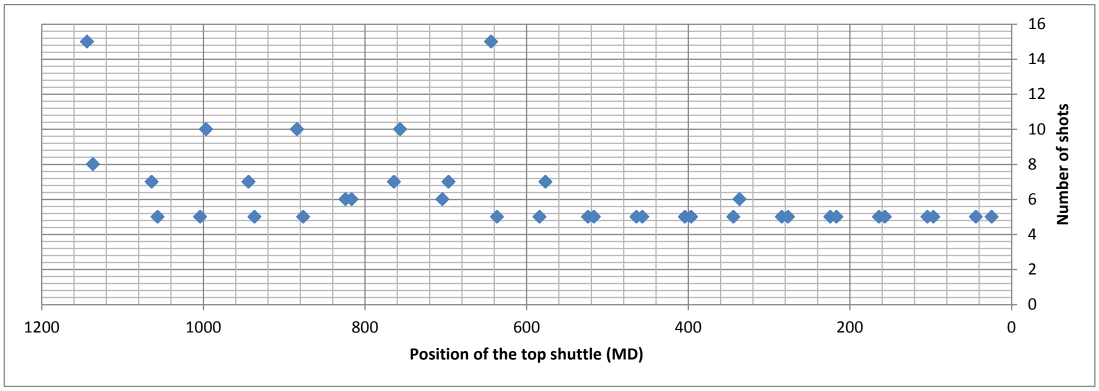

Figure 42. Number of shots per receiver level.

3.2. VSP data processing

The zero-offset VSP data was processed using the RadExPro Advanced (DECO Geophysical) software package. Several routines were performed using purposely designed Matlab/Octave codes.

The general processing flow that was used is listed below:

- Data input, geometry
- Statics, vertical stacking
- Amplitude recovery
- Deterministic deconvolution
- Wavefield separation
- Velocity survey processing
- Normal move out correction
- Corridor stack

After generic VSP data processing we performed additional steps to obtain a well-tie and estimate seismic attenuation and anisotropy parameters.

3.2.1. Data input, geometry

The data was loaded directly from raw shot records (*.rcd files) and verified later using SEG-Y files when they became available.

The coordinates of the source and receiver positions, relative to the well head, were derived from observer logs and deviation survey data provided by GSWA.

3.2.2. Statics, vertical stacking

The reference hydrophone record for the second run of VSP data acquisition is presented in Figure 43.

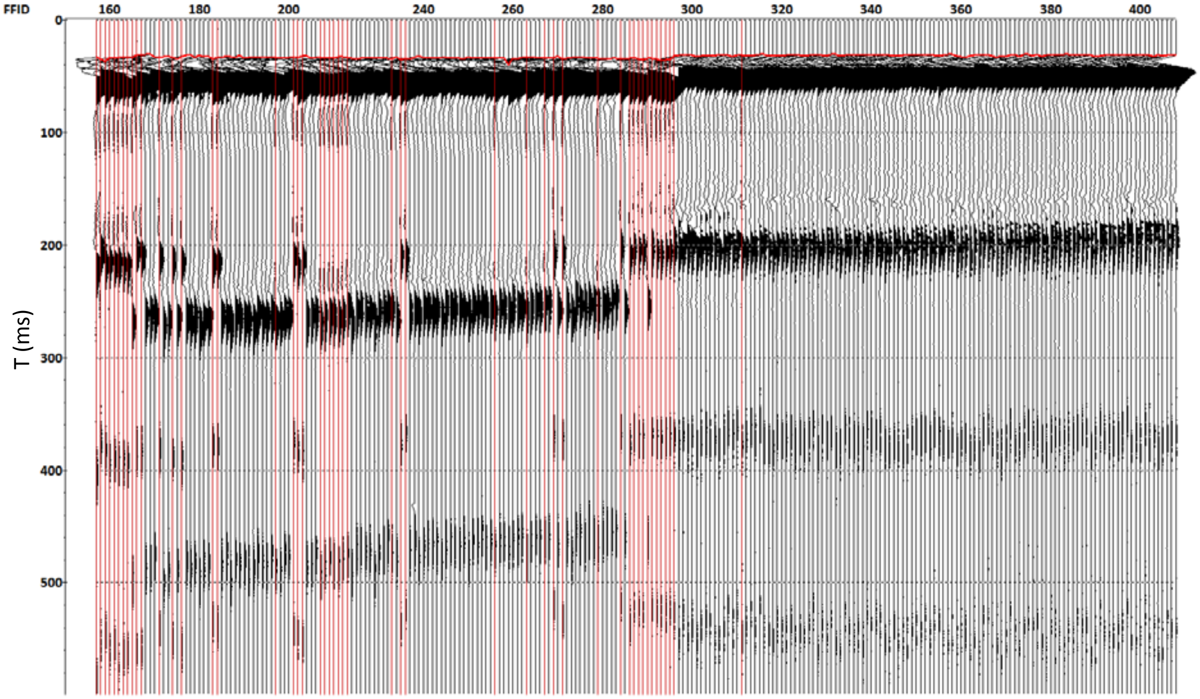

Figure 43. Monitor hydrophone data, traces corresponding to FFIDs marked with red are excluded from processing due to significant source instability.

First arrivals were picked on the monitor hydrophone data and used to apply source statics before the stacking of the geophone traces corresponding to the same depth level.

To compensate for significant variations in source signature a shaping filter (L2, 200 ms, 1% of white noise) designed using the near field hydrophone data was applied to raw shot records prior to stacking (Figure 44, Figure 45).

In the main processing flow the source signature was removed from the data together with some multiples using the 'up-by-down' VSP deconvolution process (Ross and Shah 1987).

Both monitor hydrophone data and actual geophone traces were used to identify individual shots which we excluded from stacking due to excessive noise levels or significant source instability. Prior to stacking traces were aligned for each geophone level.

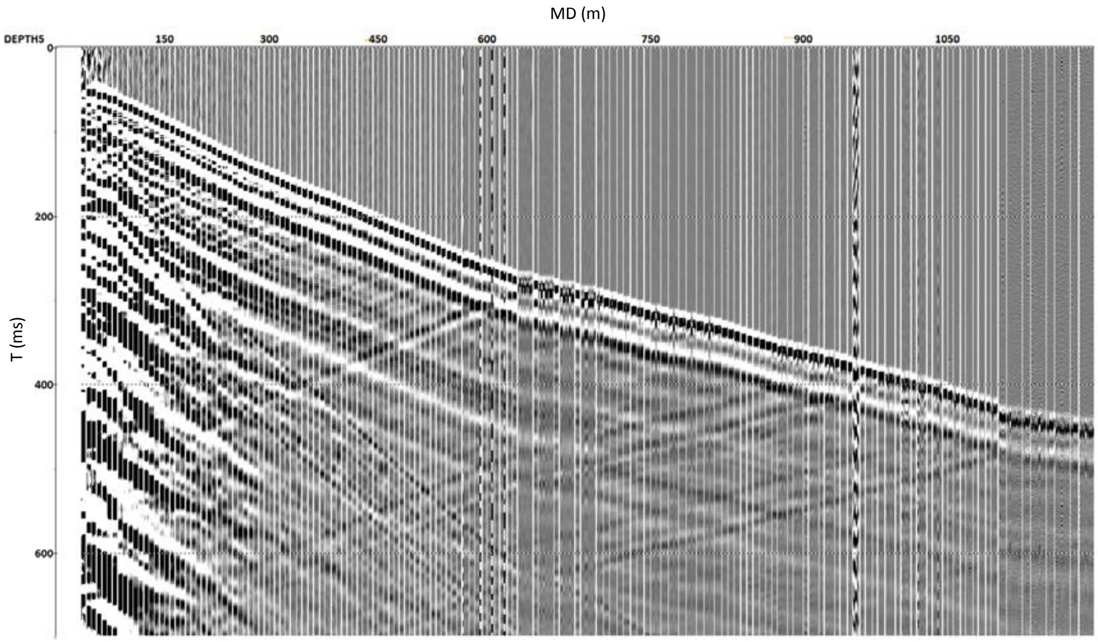

Figure 44. Raw data (Z component) before deconvolution.

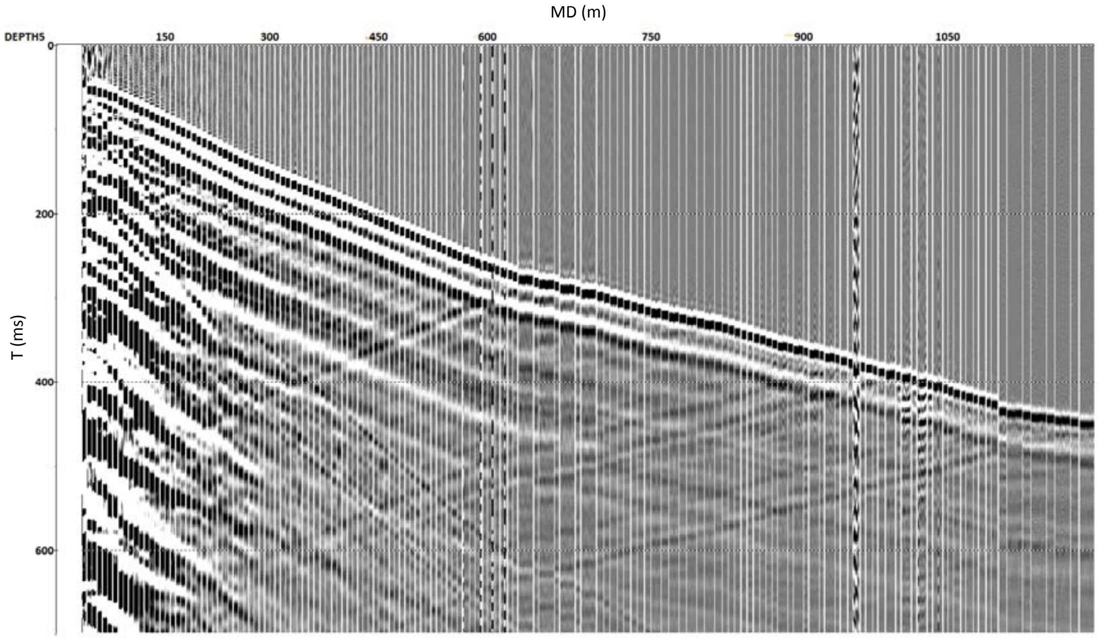

Figure 45. Raw data (Z component) after source signature deconvolution.

The result of the stacking is presented in Figure 46.

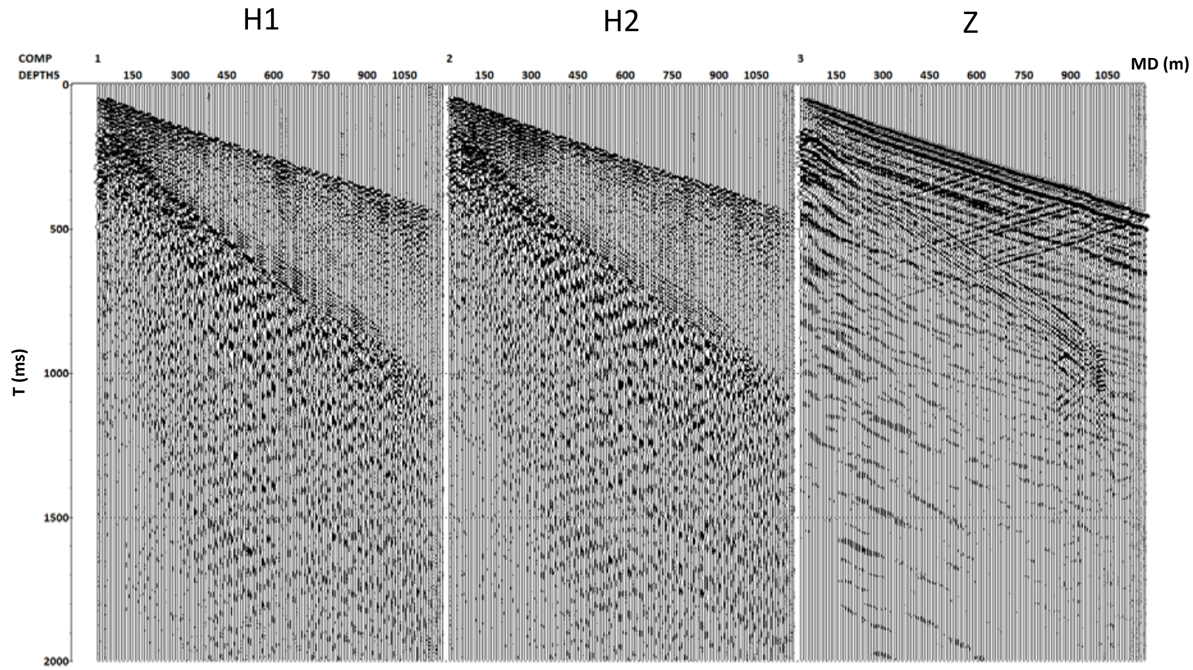

Figure 46. GSWA Harvey-1 raw ZVSP data (H1, H2 – horizontal components, Z – vertical).

3.2.3. 3C orientation

As no dedicated orientation device was used to acquire the data we employed a polarisation analysis of the direct P-wave to orient horizontal components to radial and transverse directions.

To QC orientation and vector fidelity of the tool we compared estimated dip angle of polarisation of the direct P-wave with the angle between the vertical axis and the direction from source to receiver (Figure 47).

The result of the orientation is show in Figure 48. The horizontal component contains significant amounts of shear waves generated by the source as well as PS converted waves. This will allow us to use PS converted shear waves for shear wave velocity profile estimation.

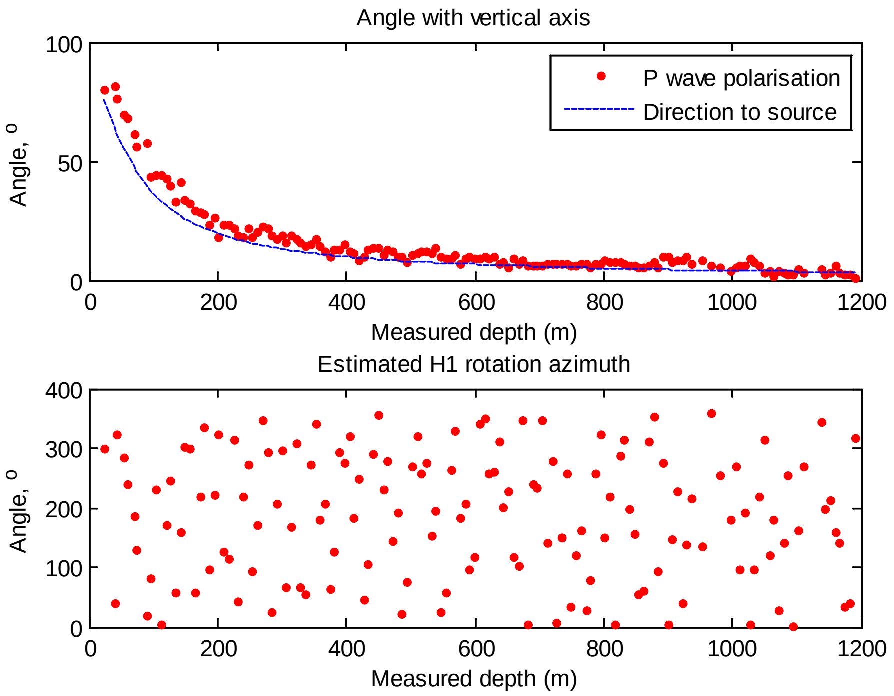

Figure 47. Direct wave polarisation analysis used to orient horizontal components.

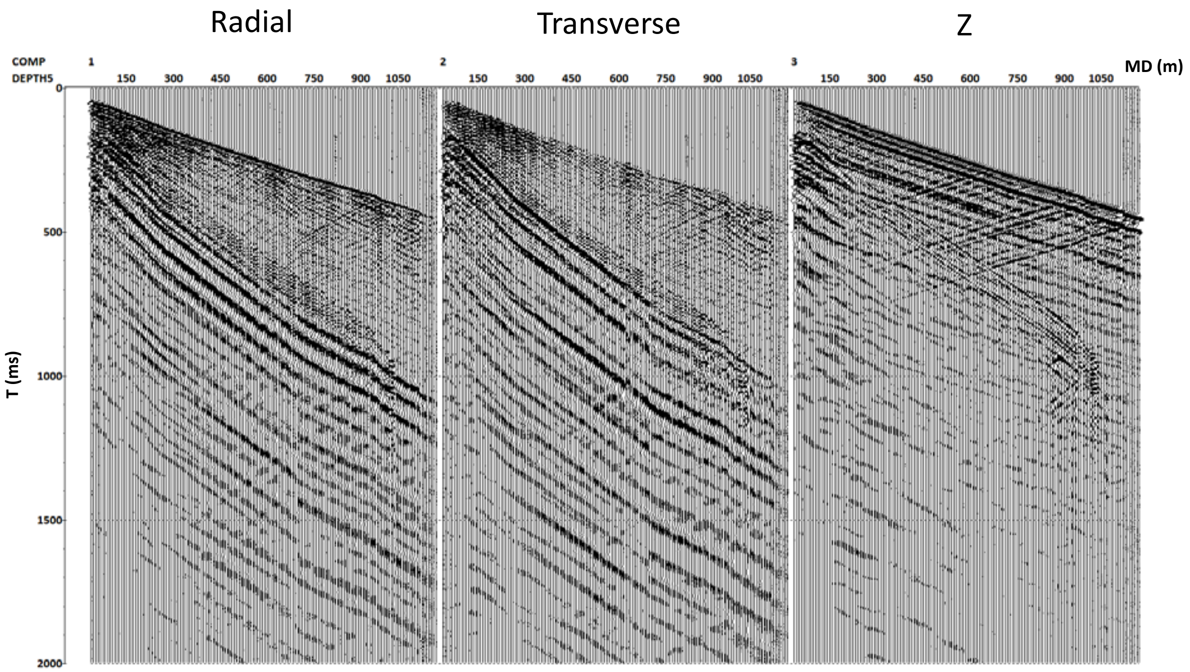

Figure 48. GSWA Harvey-1 ZVSP data after 3C orientation.

Processing steps prior to estimation of the corridor stack trace were applied to the Z-component only.

3.2.4. Amplitude recovery

To compensate for amplitude decay due to divergence of the wavefront a single function (t^2) was used.

3.2.5. Deconvolution

Deterministic deconvolution using downgoing P-waves as an estimate of the wavelet was used to correct the phase of the wavelet to zero and widen the amplitude spectrum. The depth range was divided into two parts: above and below 690 m (as this depth coincides with a significant change in source signature), for this interval the wavelet was estimated by taking an alpha-mean trimmed (50% rejection) average of the downgoing wave field. Traces which correspond to receiver levels above 350 m were excluded from processing because of extreme source-generated noise level. The length of the wavelet used for deconvolution was 480 ms.

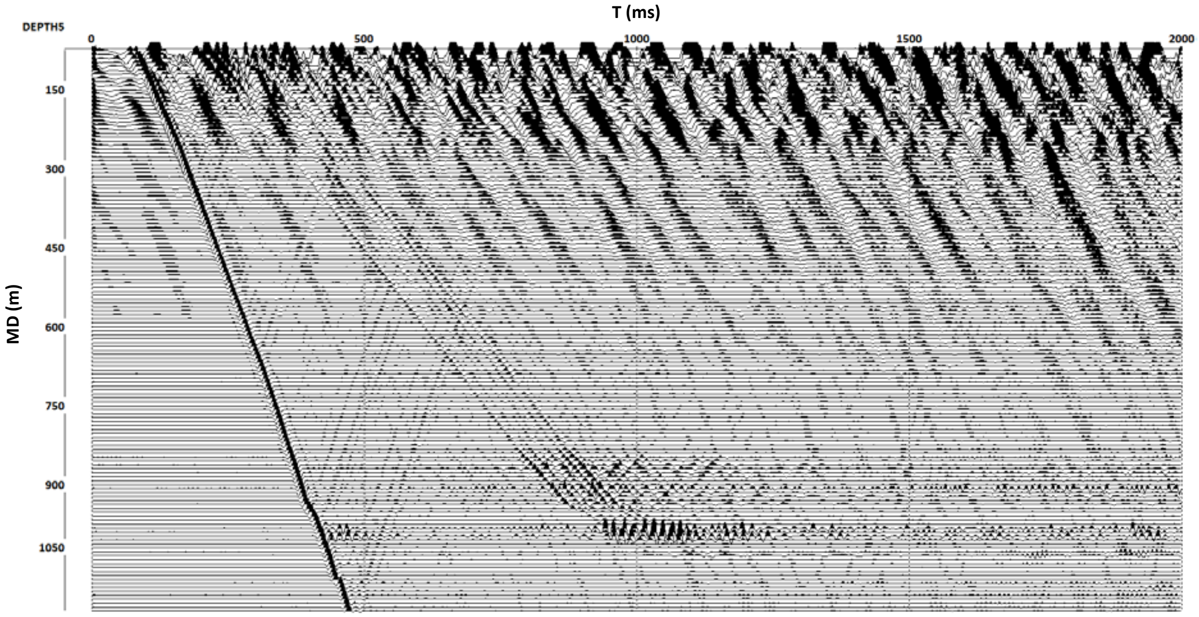

Figure 49. GSWA Harvey-1 ZVSP data, Z component, deconvolution and amplitude correction applied.

3.2.6. Wave field separation

A set of 2D filters (11 traces, alpha-mean trimmed with 50% rejection) in the T-X domain were applied in order to separate the upgoing PP waves. Each unwanted component of the wavefield, such as downgoing P and PS waves, tube waves, etc., was sequentially subtracted from the seismogram via the application of an alpha-mean trimmed 2D filter along its travel time curve in rejection mode.

In order to suppress remaining random noise, a 3x1 running mean average along travel time curves of the PP reflected waves and a bandpass filter (5-10-60-110 Hz, zero-phase, Ormsby) were applied at the final stage of processing. A significant part of the record above the 200 m MD is contaminated with strong surface wave noise. Unfortunately it is impossible to apply 2D filters with a directivity pattern sufficiently narrow to exclude all of them without damaging upgoing PP waves. However as they appear only at late times it will still be possible to pick corridor stack trace mutes to avoid that area, e.g. this will not affect the well tie process.

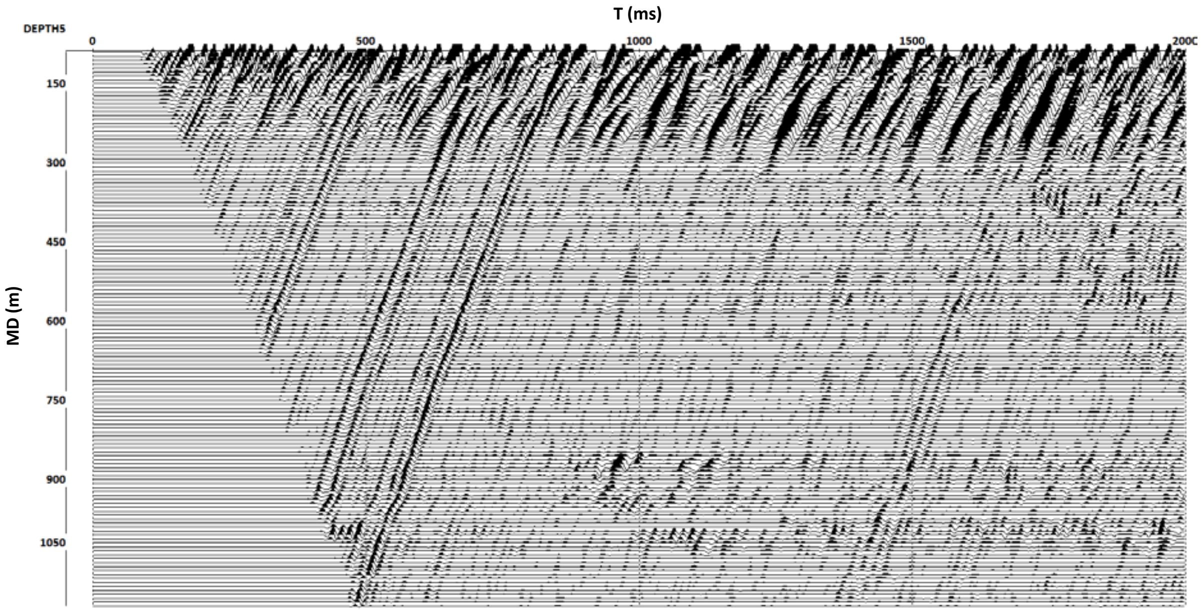

Figure 50. GSWA Harvey-1 ZVSP data, Z component, upgoing PP waves.

3.2.7. Velocity survey processing

To derive the two way travel time curve as a function of depth and also estimate interval P-wave velocities, an interactive tool (Advanced VSP Display) was used (Figure 51). To estimate the boundaries between the layers, the following criteria could be used:

1. Positions of reflections,
2. Bending of the two way travel time curve, and
3. Log data

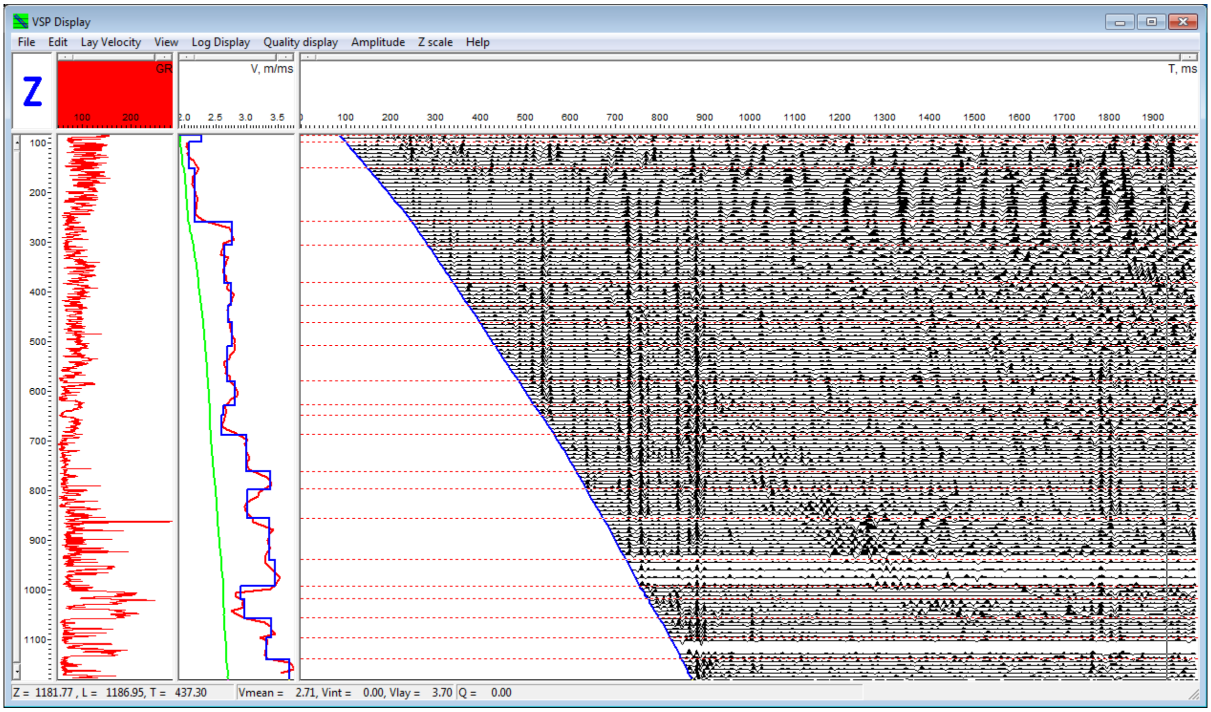

Z = 1181.77 , L = 1186.95, T = 437.30 Vmean = 2.71, Vint = 0.00, Vlay = 3.70 Q = 0.00

Figure 51. GSWA Harvey-1 ZVSP data, Interactive velocity analysis.

Strong source-generated shear waves were observed in the horizontal component after the 3C orientation of the VSP tool. They were used to estimate the S-wave velocity profile in a similar way. In addition, a shear wave velocity profile was obtained using multicomponent velocity analysis techniques (Pevzner et al. 2011); discussed below.

The result of the velocity model survey processing is shown in Figure 52. Tables with the derived check shot data and velocity values are presented in Appendix 1 and 2.

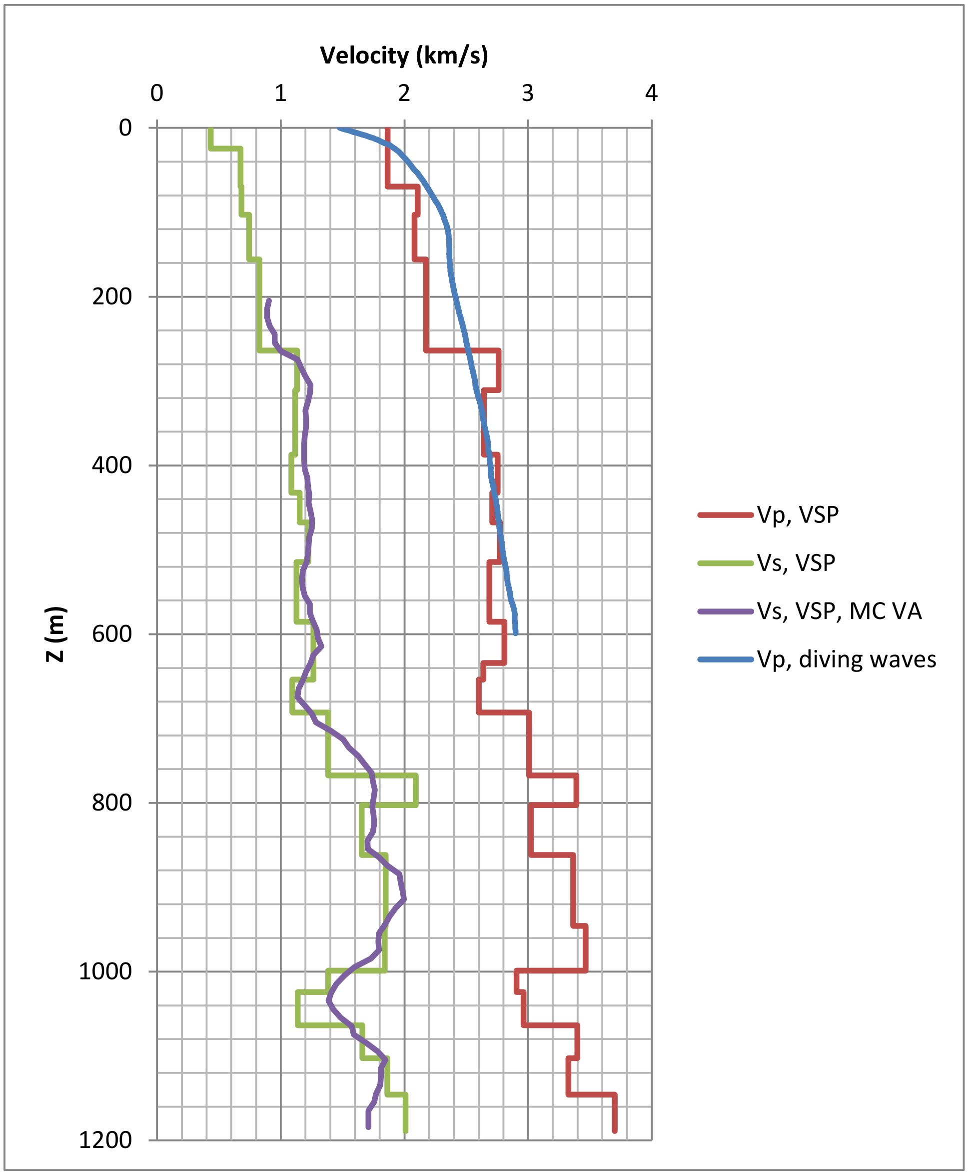

Figure 52. GSWA Harvey-1 ZVSP data, velocity model. Red and green curves represent layer velocities derived through processing of travel time curves for direct P and S waves, purple curve is V_S obtained from multicomponent velocity analysis, and the blue curve is V_P obtained from diving wave analysis performed on GSWA LL2 2D.

3.2.8. VSP NMO and corridor stack

The result of the normal moveout correction of the upgoing PP waves and the corridor stack trace are presented in Figure 53. The blue and red lines show the time gate used to compute the corridor stack trace.

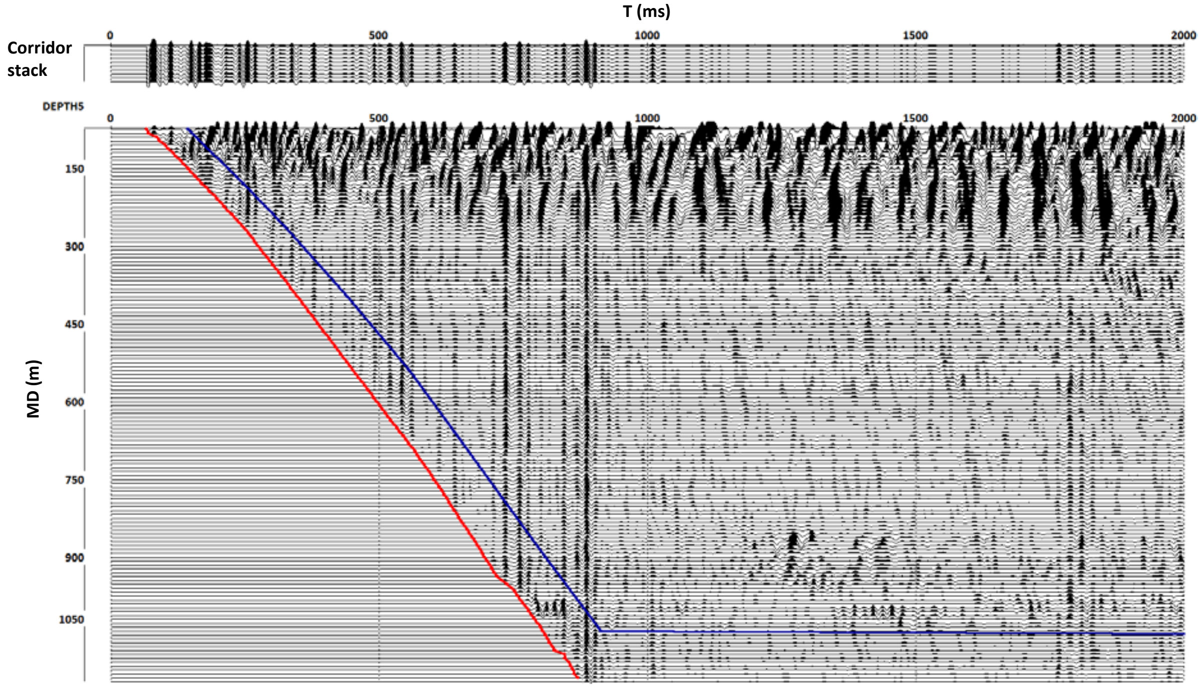

Figure 53. GSWA Harvey-1 ZVSP data, VSP-NMO and corridor stack trace.

3.3. Seismic to well tie

The well is located 165 m off line 11GA_LL2, the closest CDP is 4902. To compute actual shift between the seismic data and corridor stack trace we use a cross-correlation function computed over a 100-1200 ms time window between the corridor stack trace and CDP 4902 (here we use the data after original processing done by the contractor). Optimum shift (after taking into account an elevation static of 20.4 ms to bring VSP data to the seismic datum, which for this dataset was chosen to be MSL) is -13.6 ms.

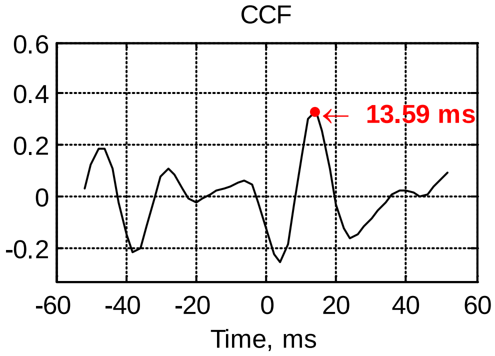

Figure 54. Cross-correlation function.

Results of the well tie using the corridor stack trace are presented in Figure 55. VSP data typically has a wider amplitude spectrum. To equalise the frequency content between VSP and the surface seismic standard, a Wiener filter was computed (40 ms, 1% random noise). Then, the amplitude spectrum of the corridor trace and the VSP data with the normal moveout correction applied were multiplied by the amplitude spectrum of the filter (i.e., the phase spectrum was preserved). All major reflectors can be traced from VSP to surface seismic data.

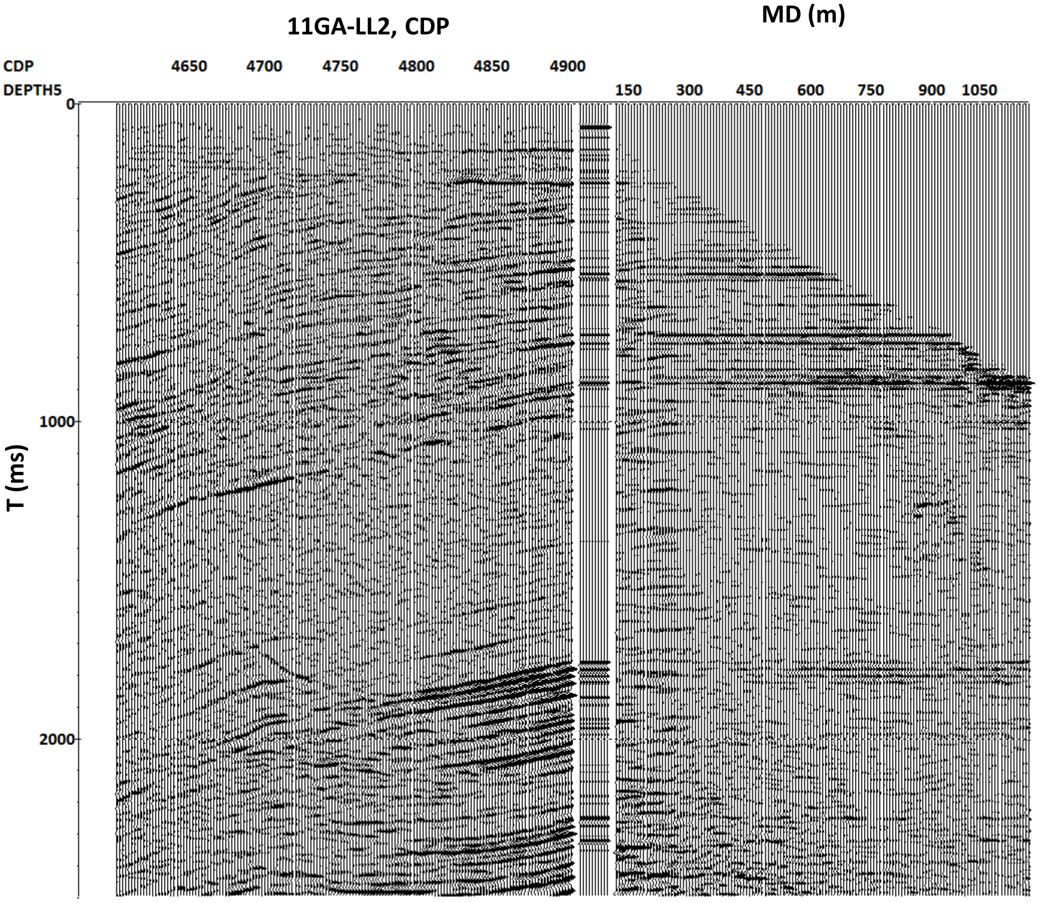

Figure 55. GSWA Harvey-1 ZVSP, the result of the seismic to well tie after spectral matching.

Corresponding check-shot table is provided in Appendix B.

3.4. Estimation of seismic attenuation from ZVSP data

3.4.1. Estimation of apparent attenuation from VSP data

In order to estimate attenuation from the VSP data, we assume that propagation of the seismic wave can be described with linear system theory (Quan and Harris 1997). In this theory, the amplitude spectrum $S_R(f)$ of a direct wave recorded by a receiver located at a given depth is given by by the equation:

$$S_R(f) = G(f) D \cdot H(f) S_0(f) \, , \tag{3.1}$$

where f is frequency; $G(f)$ is a factor including instrument response, source coupling, receiver coupling, radiation pattern and frequency-independent transmission losses; D is a factor responsible for wavefront divergence; $S_0(f)$ is the amplitude spectrum of the emitted wave; and

$H(f)$ describes the attenuation effect. To describe the attenuation effect $H(f)$, we can use the following notation (Quan and Harris 1997):

$$H(f) = \exp\left(-f \int_{ray} \alpha_0 dl \right), \tag{3.2}$$

where α_0 is the attenuation coefficient. This coefficient is related to the quality factor Q: $\alpha_0 = \pi/(Qv)$, where v is the velocity of the wave. This relation implies that both Q and v are independent of frequency.

Recently we examined (Pevzner et al. 2012) a number of approaches for apparent Q estimation from VSP data: the spectral ratio method (Ganley and Kanasewich 1980), the centroid frequency shift method (Hauge, 1981, Quan and Harris, 1997) and the spectral amplitude matching technique (Jansen, 1985; Blias, 2011) for stability in the presence of random noise.

We found that the results of the spectral matching technique and centroid frequency shift method are similar and both are superior to the spectral ratio method. In this study we employ the workflow used in (Pevzner et al. 2012) to analyse GSWA Harvey-1 ZVSP data.

This approach is based on a modified centroid frequency shift method. The centroid frequency of the propagating wave, defined as

$$f_R = \left(\int_0^\infty f \cdot S_R(f) df \right) \Big/ \left(\int_0^\infty S_R(f) df \right), \tag{3.3}$$

decreases linearly with distance and the proportionality constant is proportional to the attenuation coefficient. For an amplitude spectrum given by the Gaussian function, the centroid frequency shift between a pair of receivers located along the ray path is

$$\frac{(f_{R1} - f_{R2})}{\sigma_{R1}^2} = \int_{ray} \frac{\pi}{Qv} dl, \tag{3.4}$$

where σ_R^2 is the variance of the Gaussian spectrum:

$$\sigma_R^2 = \left(\int_0^\infty (f - f_R)^2 \cdot S_R(f) df \right) \Big/ \left(\int_0^\infty S_R(f) df \right). \tag{3.5}$$

For non-Gaussian spectra, Equation 3.5 will have an additional scaling factor. In order to take into account the decreasing bandwidth of the spectra (and the variance) with distance, we modified Equation 3.4 by using the average variance estimated for the pair of receivers rather than the variance at the first receiver.

The main workflow consists of the following stages:

1. Amplitude of the direct wave is measured along the first (negative) extremum in the direct wave (maximum amplitude and RMS amplitude computed in 10 ms window around the first extremum, data was resampled to 0.1 ms prior to measurements) using 3C records. Figure 47 shows a very good agreement of polarisation of the direct P-wave which allows us to assume good vector fidelity of the tool. So we can use all 3 components to measure the amplitude rather than correcting measurements on the Z-component only for the angle of incidence. We also apply a divergence correction using (Newman 1973). As this correction does require velocity information, we use first break picks to estimate interval and RMS velocity. Corrected amplitudes are presented in Figure 56. One can see that the overall amplitude decay (related to scattering and attenuation) rate is about 12 dB/km. These amplitude estimations will be used to QC our attenuation estimates.

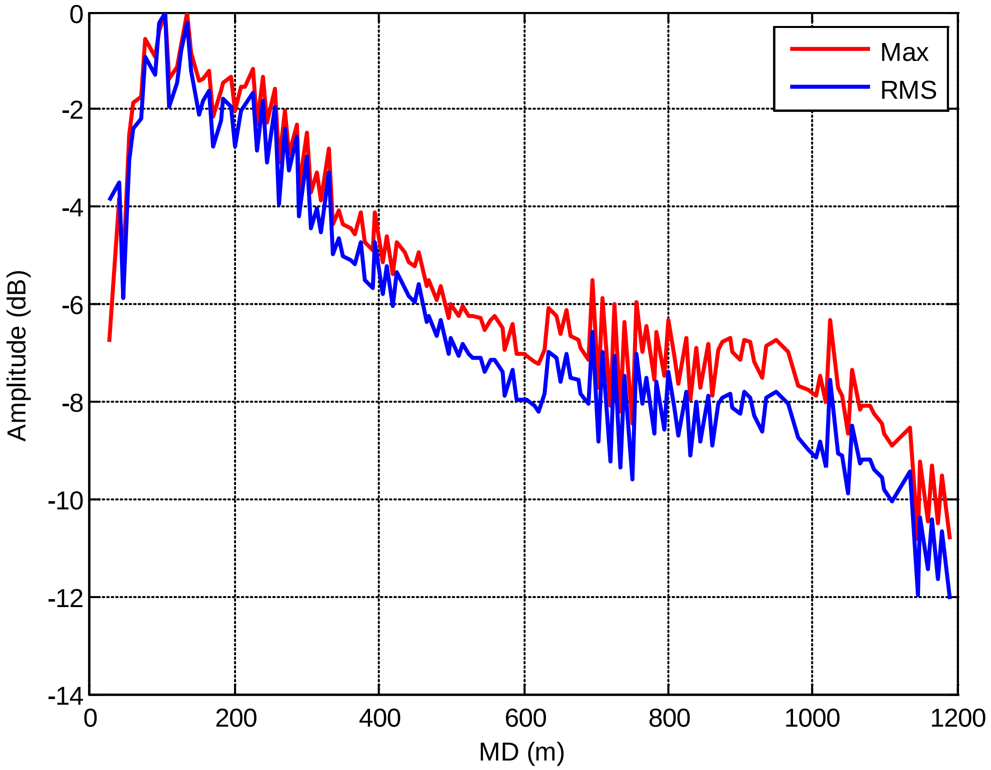

Figure 56. Amplitude of the direct wave.

2. Zero offset VSP data has to be conditioned prior to estimation of attenuation parameters in order to suppress all waves in the analysis window except for the downgoing direct wave. Due to presence of strong S-waves even in the Z-component close to direct arrivals (at top part of the section) we used a 100 ms window (from first arrivals) which does not allow them to affect estimates of the amplitude spectrum.

The presence of upgoing waves in the analysis window can affect the amplitude spectrum estimation. In this research we are using F-X deconvolution applied after flattening of the first arrivals (Figure 57).

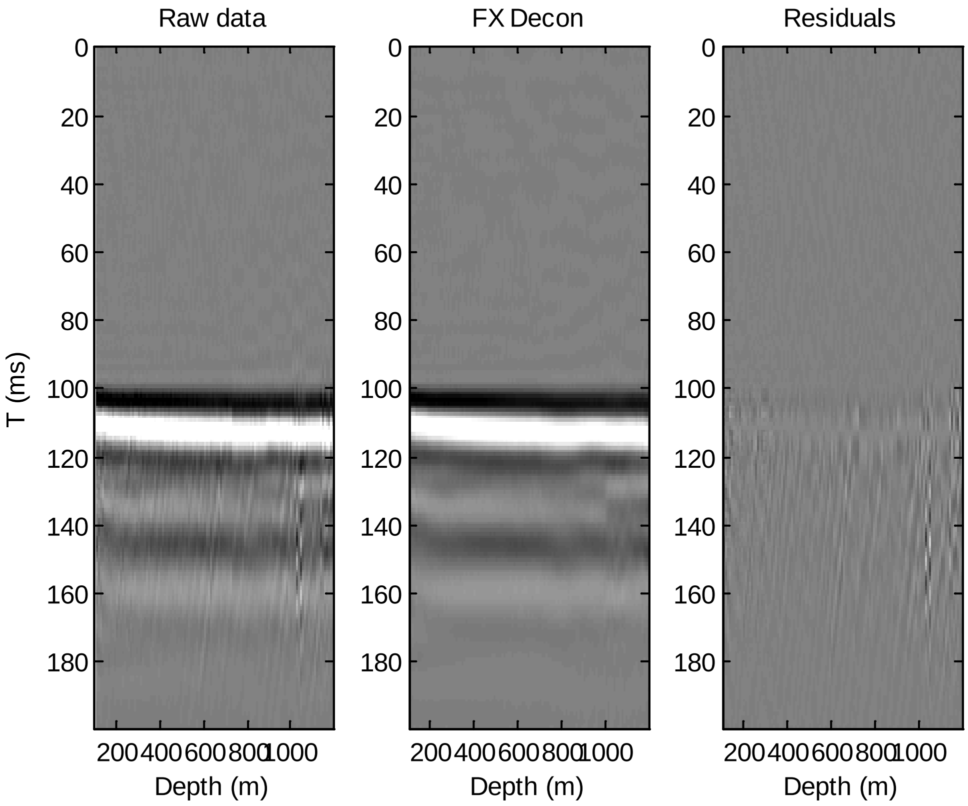

Figure 57. Amplitude spectrum analysis window, F-X deconvolution applied to suppress upgoing P-waves.

3. Computation of centroid frequency and frequency variance curves.

The amplitude spectrum of the downgoing P-wave was computed (Figure 58). It shows a substantial decay of the high frequency component of the signal with depth.

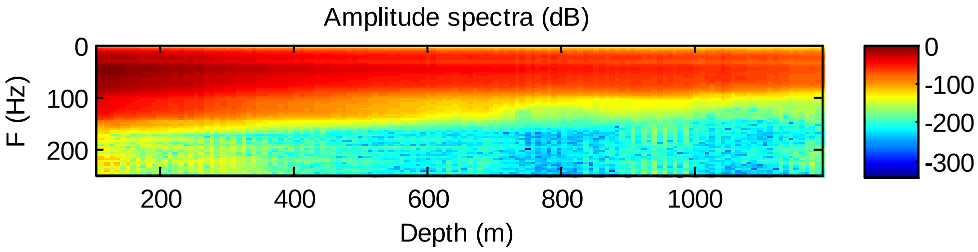

Figure 58. Amplitude spectrum of direct P-wave.

Centroid frequency and it's standard deviation (square root of the varianceis used as it is measured in Hz) are presented in Figure 59. Centroid frequency steadily decays from ~59 to 49 Hz over the 100 m to 700 m interval and from 50 Hz to 47 Hz over the 900 m to 1184 m MD interval. A sudden increase of centroid frequency from 700 to 900 m is most likely caused by severe changes in source conditions which were not fully compensated for by using the shaping filter during pre-processing. The character of the amplitude decay curve (Figure 56) supports this explanation.

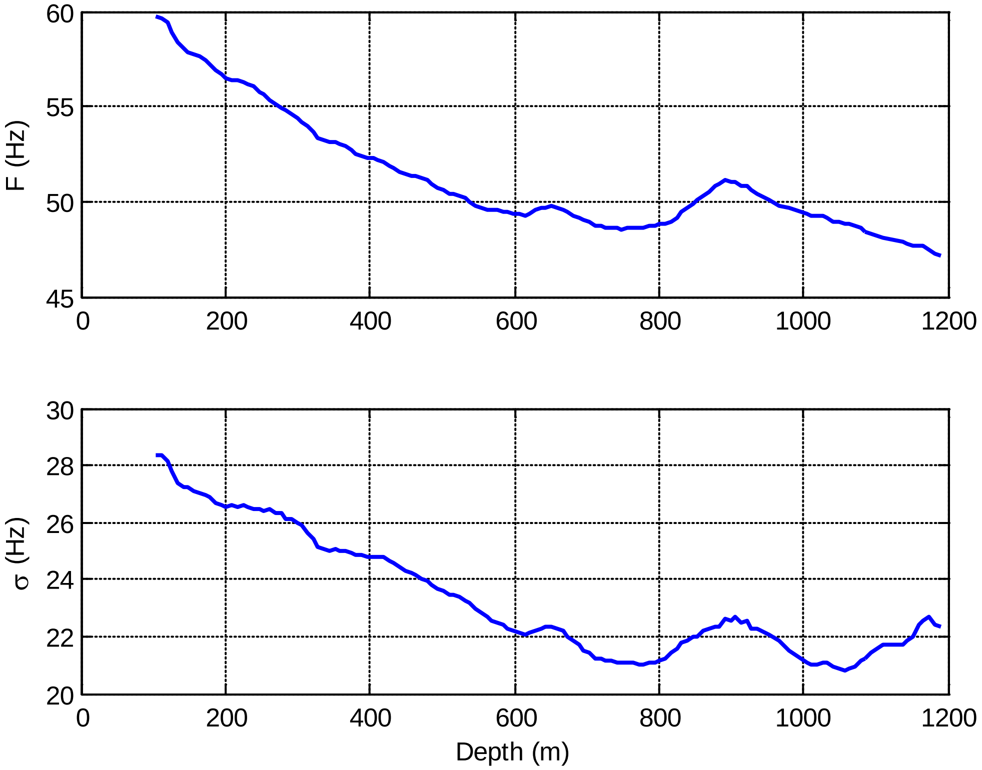

Figure 59. Centroid frequency and amplitude spectrum variance curves.

4. Estimation of Q for the thick-layered model using the centroid frequency shift method.

Interval estimates of seismic attenuation are shown in Table 6. Overall Q values are quite low, close to 40.

Table 6. Interval Q estimates

Interval (MD)/formation	Q^{-1}	**Q**
104-250 m, Leederville Fm	0.029	35
250-625 m, Eneabba	0.025	40
or*		
250-704 m, Eneabba + Basal Eneabba Shale	0.022	46
900-1184 m, within Lesueur Formation, Yalgorup Mbr	0.029	35
* - 625-704 m is too short of a depth interval to obtain reliable estimates for the Basal Eneabba Shale formation alone		

In order to QC these estimates we compute direct wave amplitude decay due to attenuation and compare it to actual amplitude decay curves corrected for the wave front divergence (Figure 60). These two curves match with less than 2 dB discrepancy.

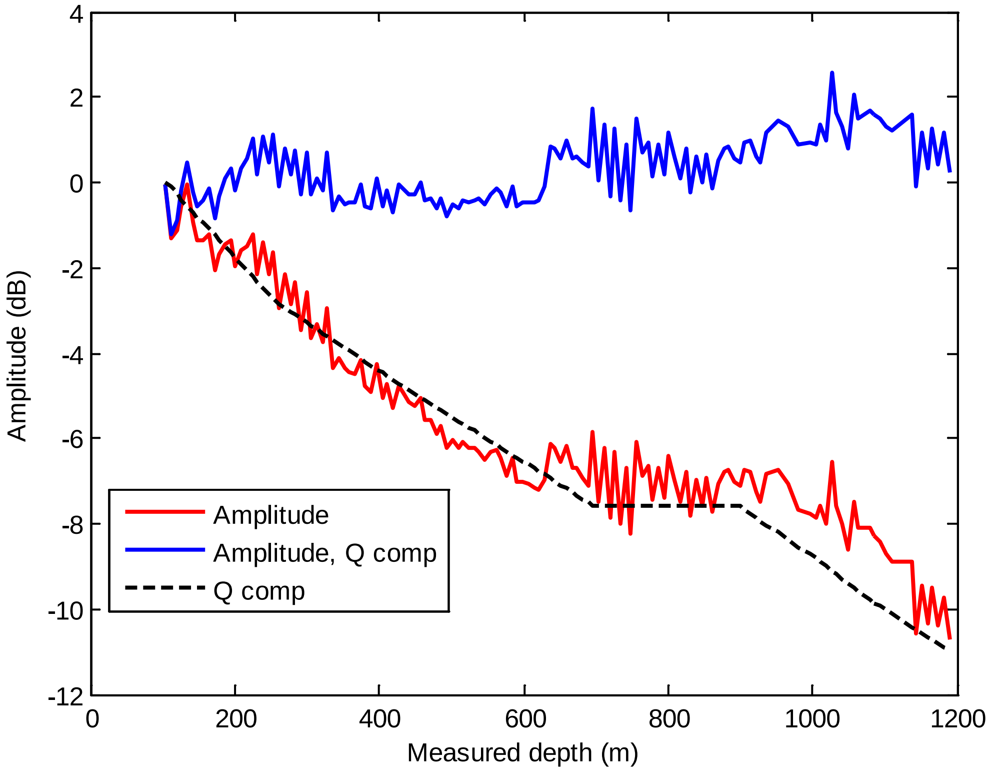

Figure 60. Direct wave amplitude decay curve (red), amplitude decay due to attenuation (black) and amplitude decay curve after Q-compensation (blue).

3.4.2. Scattering vs intrinsic attenuation

Unfortunately without good acoustic and density log coverage for the top part of the section (above 872 m) we cannot incorporate an estimate the relative contribution of scattering and intrinsic components into the overall Q estimates. However we can provide scattering Q estimates for the interval below 872 m. In order to do this we built an elastic model using VSP and sonic log data, computed full-waveform synthetics using the OASES package (MIT) and run a workflow similar to that applied to the field data.

To build the model we used the following assumptions:

1. P-wave velocity above 872 m MD is taken from the VSP andbelow from the log data
2. S-wave velocity above 872 m MD is taken from the VSP and below from Castagna's equation (Castagna et al. 1985): $V_S = 0.86V_P - 1.172$ (where V_P and V_S are measured in km/s). Figure 61 shows a match between V_P and V_S estimates from VSP data with the mudrock line.
3. Density below 872 m is taken from log data and above 872 m it is reconstructed from P-wave velocities using Gardner's equation (Gardner et al. 1974). In order to match the velocity-density relationship for the bottom interval, coefficients in the equation were updated using a least-squares fitting: $\rho = 0.30754V_P^{0.24546}$ (Figure 62).

.

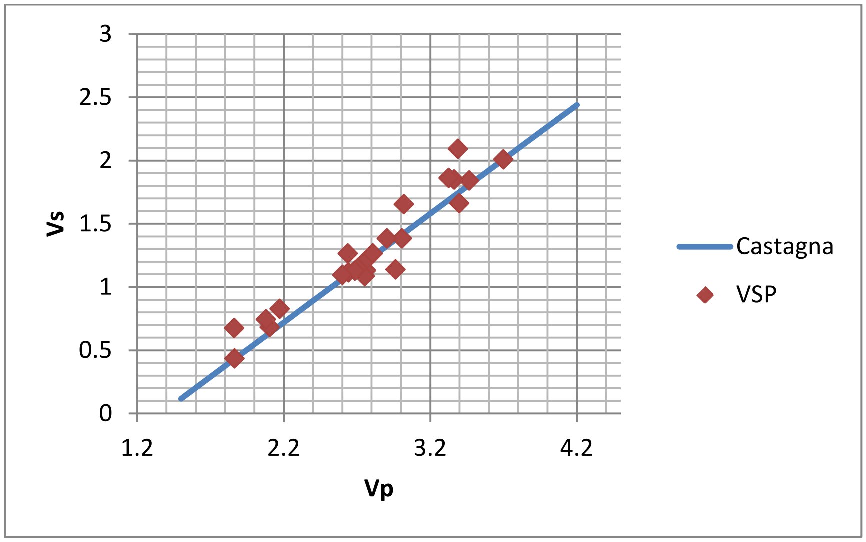

Figure 61. Match between V_P and V_S estimates from VSP data with the mudrock line.

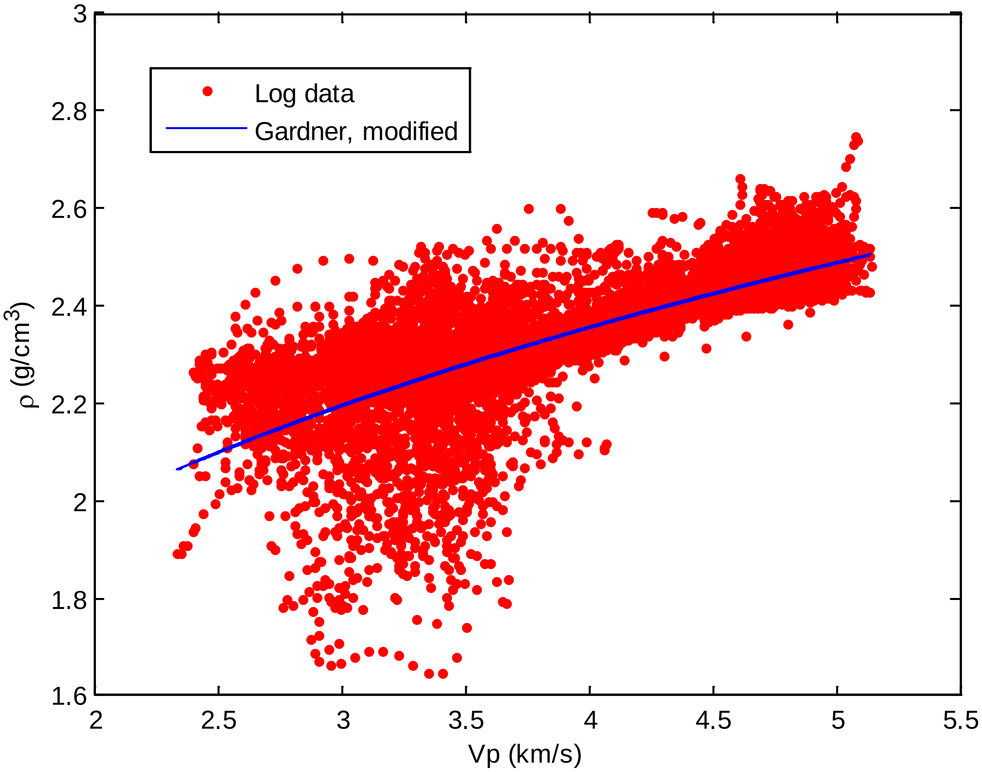

Figure 62. V_P -density relation

In the final step the elastic model was upscaled (Backus 1962) below 872 m to a new layer thickness of 3 m (Figure 63).

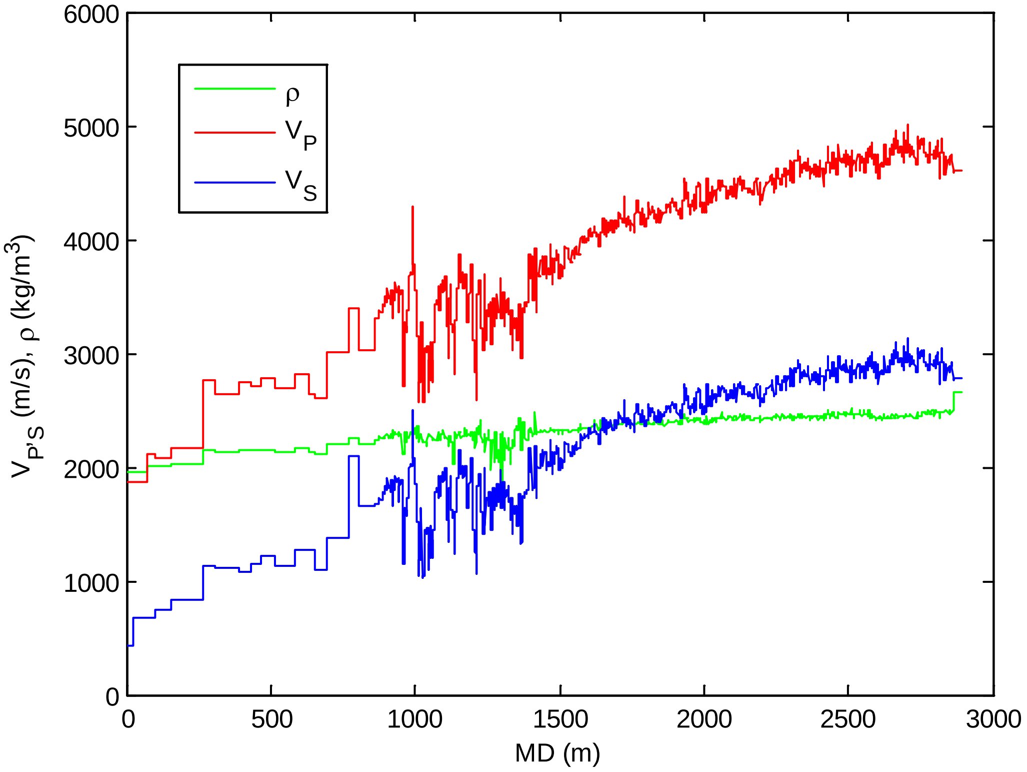

Figure 63. 1D elastic model used to compute synthetic seismograms.

Synthetic VSP seismograms were computed using a 50 Hz Ricker wavelet, 10 m receiver spacing (0-2840 m depth interval) and a 50 m source offset from the well. Estimated amplitude decay, centroid frequency and amplitude spectra deviation curves are presented in Figure 64. Obviously only the bottom part (below 872 m) can be analysed. Only the interval of ~900-1400 m MD shows scattering attenuation which can be quantified reliably with the method we employ (scattering Q ~ 250, compared to apparent Q of 35). Below this interval (e.g. within the lower Lesueur formation) we observe negligible scattering attenuation.

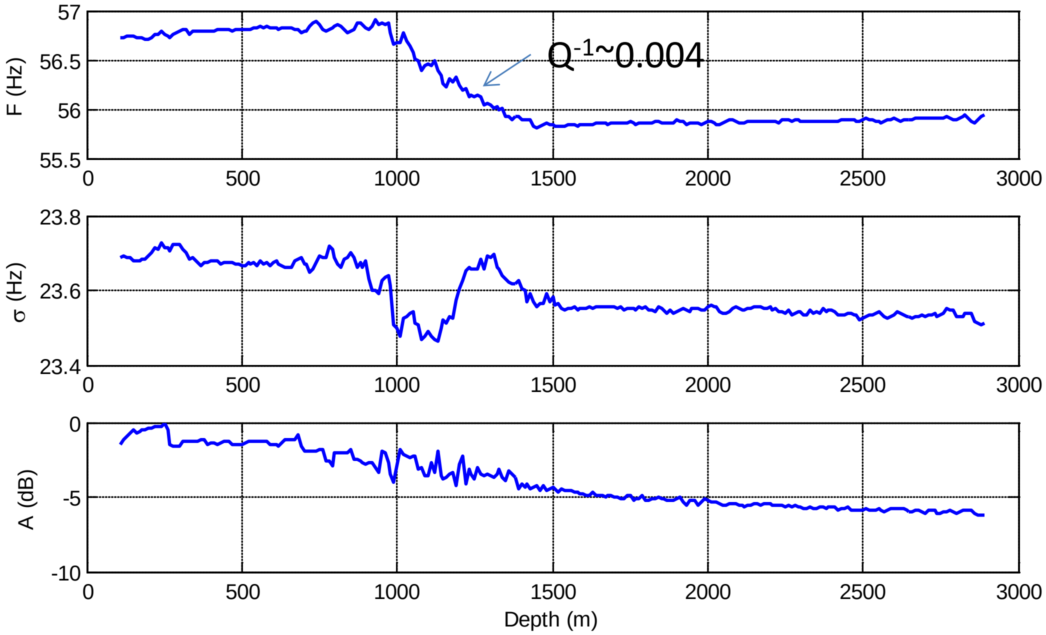

Figure 64. Centroid frequency, frequency deviation and amplitude decay curves obtained from synthetic seismograms.

3.5. Shear wave anisotropy analysis

In this study we apply multicomponent shear wave velocity analysis techniques to the horizontal components of the GSWA Harvey-1 VSP data. In addition to that we apply conventional 2C hodogram analysis.

3.5.1. Multicomponent shear wave velocity analysis

The approach used here, was published in (Pevzner et al. 2011). The algorithm of the velocity analysis is briefly summarised below. It is similar to conventional stacking velocity analysis based on velocity spectra estimation known from surface CDP seismic processing. For simplicity, we assume a HTI medium and a vertical direction of propagation of S-waves. For a given depth interval we compute azimuthal apparent S-wave velocity spectrum using a semblance function (modified in order to keep sensitivity to amplitude of the wave) using a pre-conditioned horizontal component of the oriented ZVSP data. Shear wave splitting phenomena, if it exists, would result in the presence of two maxima on the spectrum having different velocities separated by 90° along the azimuth axis. The process is performed in a running depth window for the entire receiver range.

GSWA Harvey-1 ZVSP data has a significant amount of source-generated S-waves (Figure 50). In order to prepare horizontal components for analysis we perform the following:

1. Orient the data using P-wave polarisation (discussed above)
2. Define 1000 ms analysis time window as shown in Figure 65. The first 400 ms of the same window will be used to perform hodogram analysis.

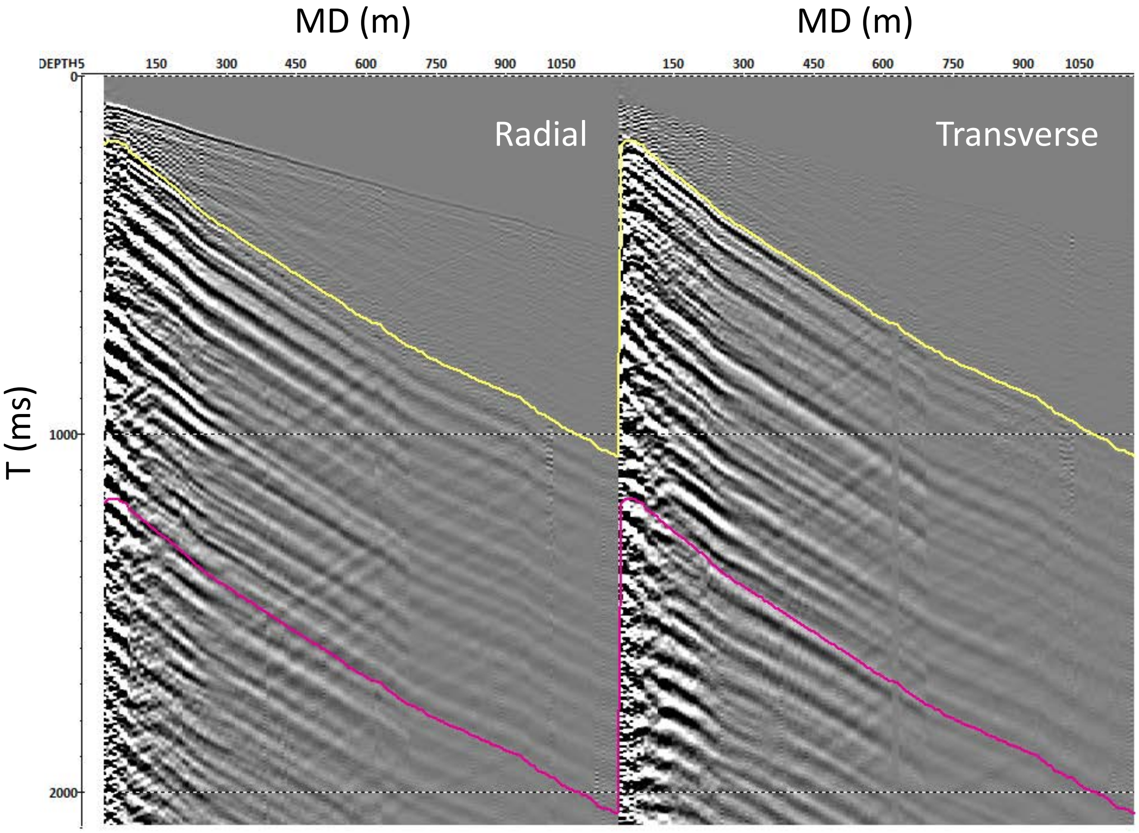

Figure 65. GSWA Harvey-1 VSP data. Oriented horizontal components. Yellow and purple lines define the time window used for analysis.

Parameters of the computations are:

Depth window: 100 m (centred), 20 m step along the borehole

Depth range: 200-1190 m

Time window for semblance computations: 30 ms

Figure 66 shows an example of the obtained azimuthal velocity spectra. The depth interval above ~500 m has a very dispersed azimuthal distribution of the shear wave polarisation and we cannot robustly identify the orientation of the shear wave's polarisation from the velocity spectra (however we can still pick the velocity). In addition to that problem we see that above 300 m data is affected by the presence of surface waves. Below this interval only one strong extremum can be picked. This most likely indicates that there is no strong shear wave azimuthal anisotropy in this area, however, properly processed cross-dipole sonic log data and additional offset/walk-away VSP surveys are needed to confirm this. A single S-wave velocity profile was automatically derived from the velocity analysis, shown in Figure 52 (purple curve), it matches with the velocity obtained from travel time curve processing.

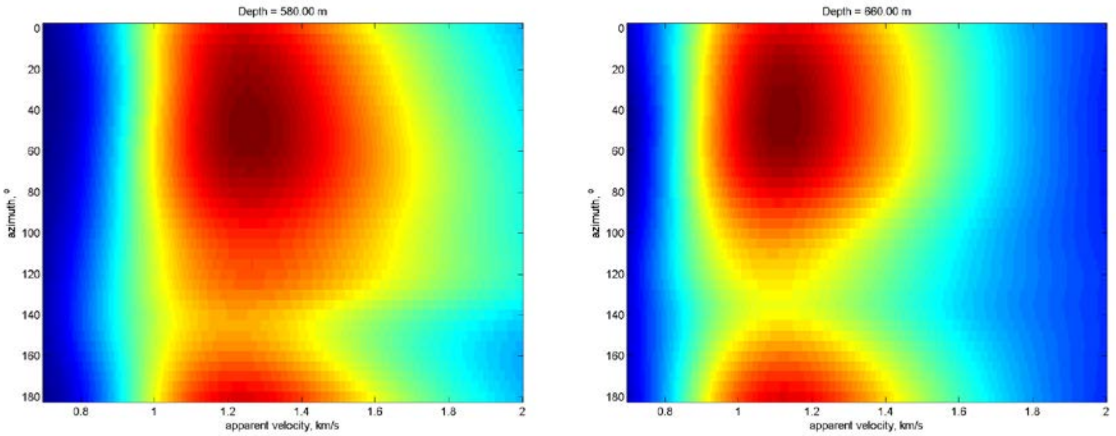

Figure 66. Azimuthal velocity spectra for 560 m (left) and 660 m (right).

3.5.2. Hodogram analysis

In addition to multicomponent velocity analysis we computed hodograms in a 400 ms window below S-wave arrivals (Figure 67). It is evident that for most of the receiver levels two shear waves can be identified. Their orientations were manually picked and compared to orientations obtained from the multicomponent velocity analysis (Figure 68). Two distinct directions separated by almost 90° degrees can be observed. However one of these directions coincides with the direction towards the source, i.e. what we see are both source generated S_H and S_V waves propagating down the well and not the result of shear wave splitting.

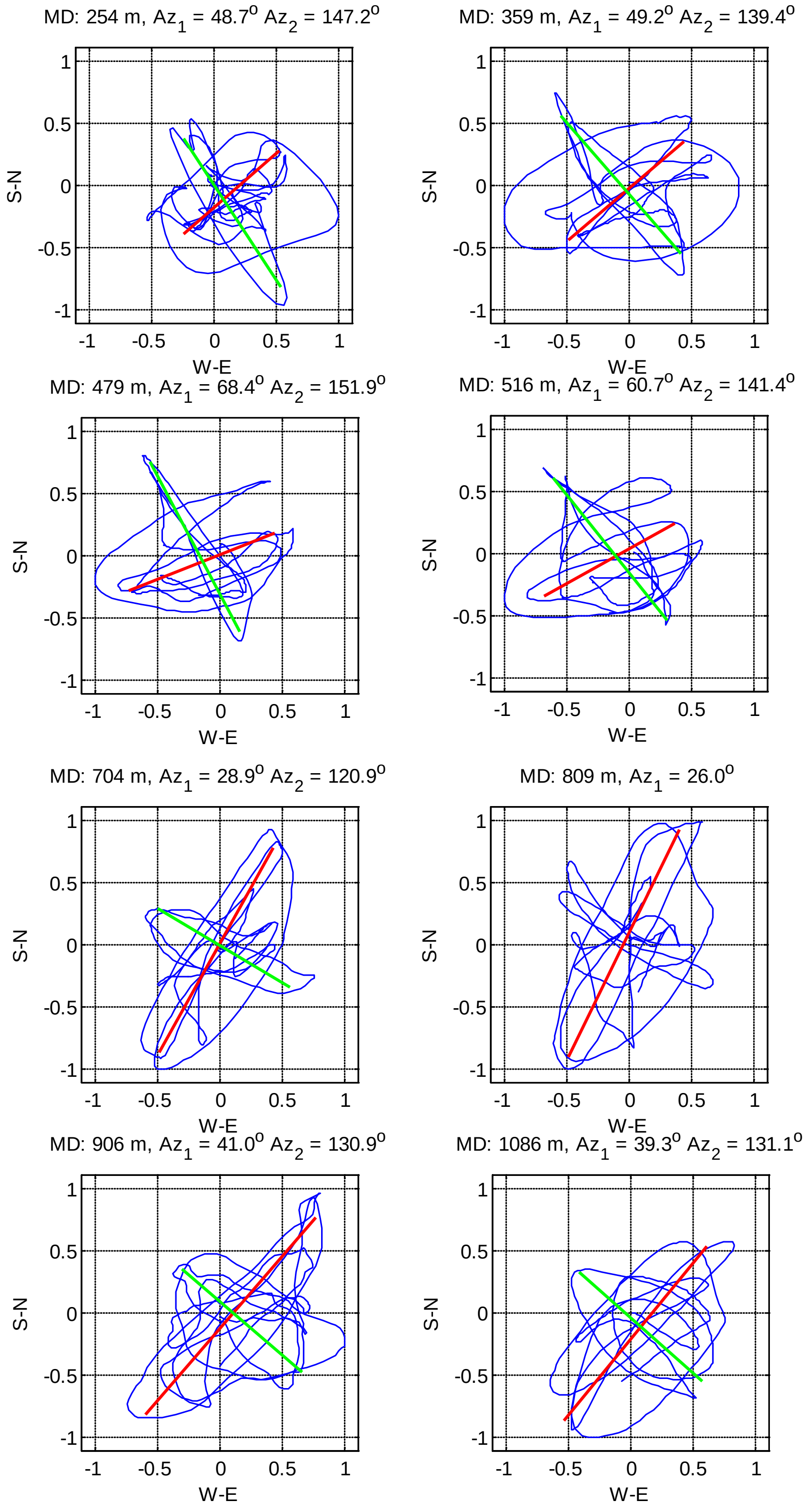

Figure 67. GSWA Harvey-1 VSP data, horizontal projection of hodograms.

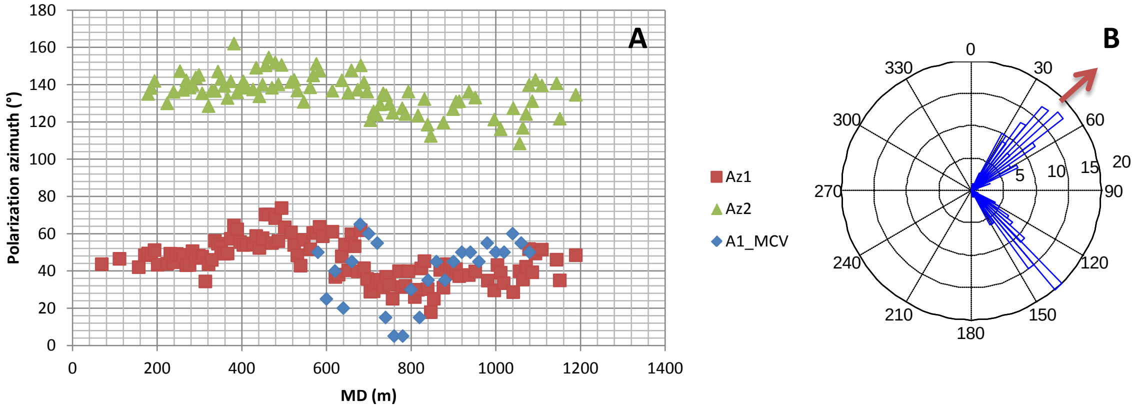

Figure 68. Polarization azimuth of shear waves, A – as a function of depth (Az1 and Az2 - manual picking on hodograms), A1_MCV - automated picking on azimuthal velocity spectra, B – rose diagram.

The main outcome of this horizontal component analysis is that no visible azimuthal shear wave anisotropy can be reported for the GSWA Harvey-1 well. A single shear wave velocity profile can be easily derived.

3.6. Harvey-1 VSP data processing – key findings

- A standard processing workflow and well tie using the corridor stack trace was carried out; VP and VS velocity profiles were derived for the entire ZVSP depth range to about 1200m depth.
- Seismic attenuation estimates give values of the apparent Q factor of about 40 for almost the whole depth range
- Attempts to estimate the relative contribution of scattering and intrinsic attenuation are limited by the log data available for the analysis, however estimates made from existing log data show that the contribution of the scattering component should play a very minor role
- No significant azimuthal shear wave anisotropy was found from shear wave splitting analysis, possibly due to the limited offsets of ZVSP coverage.
- We recommend that full offset (OVSP) surveys be acquired at all future SW Hub wells. Acquisition of walk-away VSP data should also be considered in order to obtain seismic anisotropy parameters required for high quality surface seismic imaging.

4. HARVEY-1 WELL STRESS FIELD CHARACTERISATION

The main objectives of the stress field characterization are summarised as follows:

- Summarize the wellbore instability history in GSWA Harvey-1 well and identify the main instability mechanisms.
- Construct a Rock Mechanical Model (RMM) for GSWA Harvey-1 well. The model includes continuous logs of the formations' elastic and strength properties, in-situ stresses and pore pressure. The magnitudes of these stresses determine the stress regime.
- Perform wellbore stability analysis in GSWA Harvey-1 well and determine the stable mud weight windows (MWW).
- Estimate stress field orientation from borehole data.

The results of our analysis will help address main questions of the subsurface site characterisation, namely, geomechanical properties of the reservoir rock to allow the injection and storage of CO_2 and properties of the in-situ rock stress and fault sealing capacity and long term stability to trap CO_2.

4.1. Available Data and Reports

End of Well Geological Data Report (WADMP) and Stage One (b): Assessment of the Potential for Carbon Dioxide Geosequestration in the Lower Lesuer Region (Schlumberger) reports provided the following information relevant to this study:

- statigraphic column,
- formation tops,
- well sketches,
- Leak-off test (LOT),
- well bore deviation surveys and
- drilling events.

This information is used in this study to interpret the field-scale tectonic forces in the area of interest. To obtain the local forces and stresses at the wellbore scale, which could be the main causes of wellbore instabilities, a detailed analysis of the log data is done. All the available data, which are used as an input to the geomechanical model are listed in Table 7.

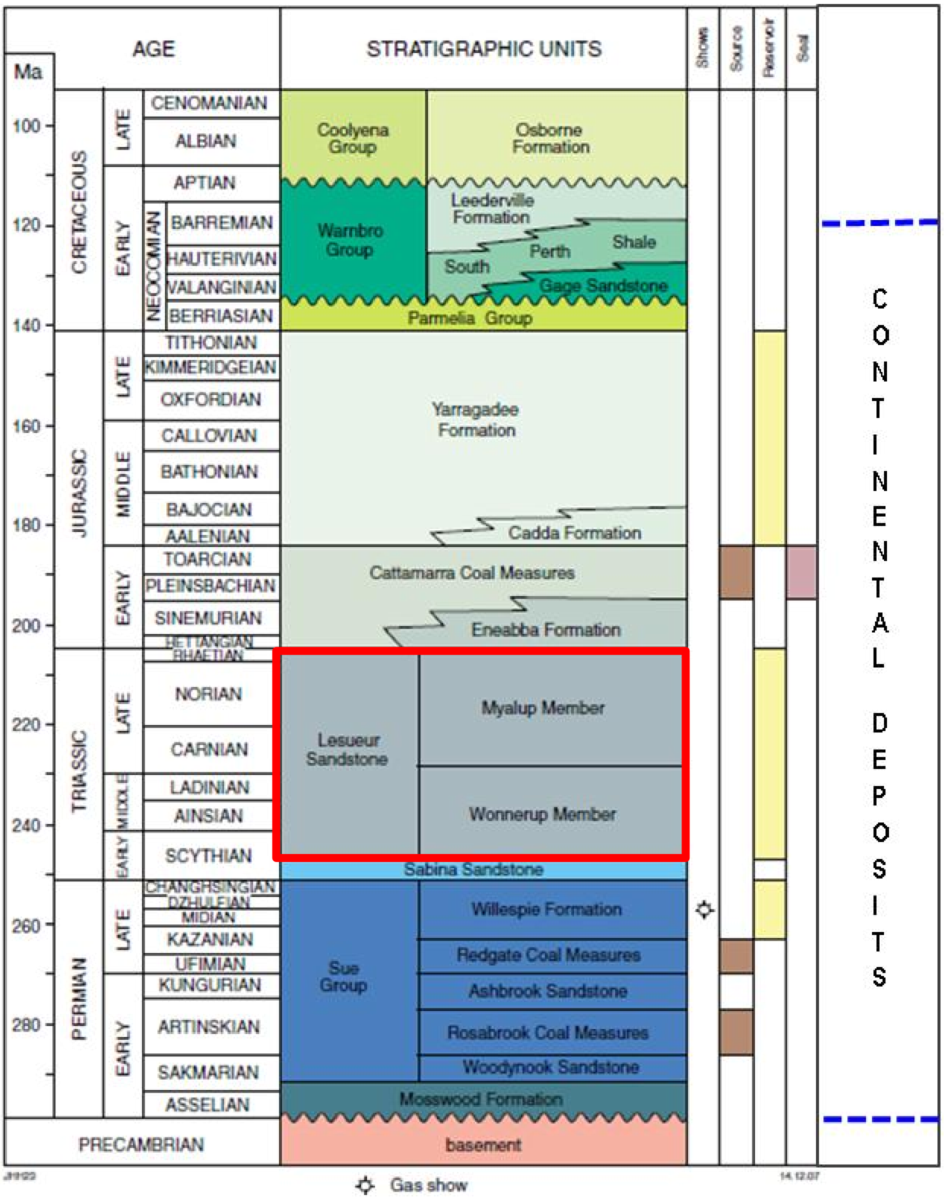

Figure 69: Stratigraphic column in South Perth Basin.

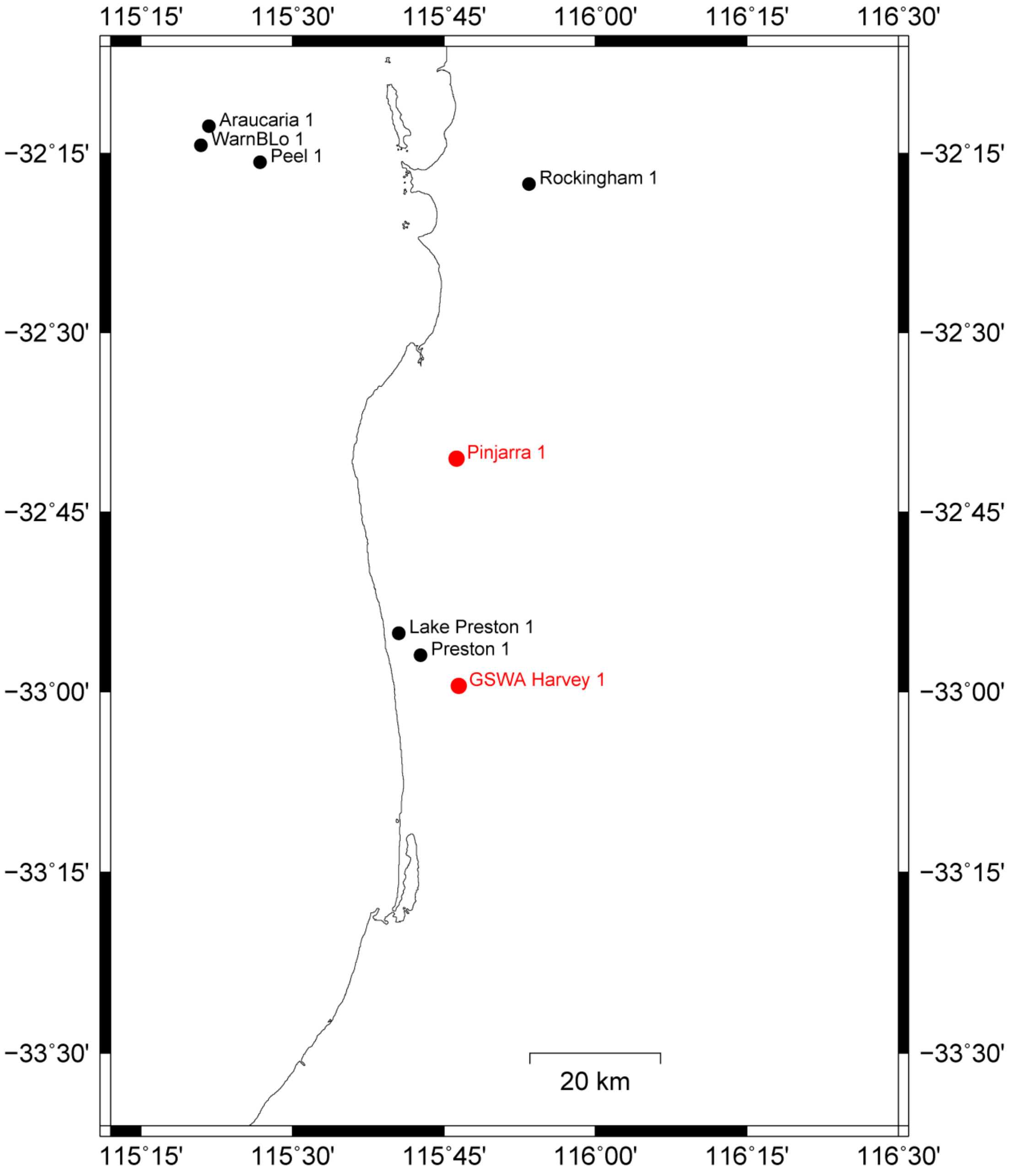

Figure 70: Location of Harvey-1 well and surrounding wells.

Table 7: Available data used for Rock Mechanical Modelling.

	Harvey-1
Gamma-Ray	Available
Density	Available
Porosity	Available
Caliper	Available
Sonic – Compressional	Available
Sonic - Shear	N/A
Deviation Survey	Available
Formation Tops	Available
Mud Density Log	N/A
Drilling Summary	Available
Image Log	Available
Oriented Calliper	N/A
Resistivity	Available
Formation Pre-Test	MDT
Petrophysical Analysis	N/A
FIT/LOT	1 LOT
Core Test (RM)	Partially available (4 samples)*
Drilling Events	Available

🟥 Essential logs for Rock Mechanical Modelling
🟨 Essential data for Rock Mechanical Modelling
🟩 Additional logs for fine tuning the Rock Mechanical Model
🟦 Additional data for fine tuning the Rock Mechanical Model

* The measured static Young's modulus, Poisson's ratio, cohesion and friction coefficient for four samples extracted from the depths of 1897.66, 1897.91, 1902.92, 1940.58 were provided by Dr. Claudio Delle Piane as studied in a companion ANLEC research project report "Facies-based rock properties distribution along the Harvey 1 stratigraphic well" ANLEC R&D project number 7-1111-0199.

As is seen from Table 7, laboratory measurements on core were available for four samples at the time when this study was undertaken. One of the closest wells to GSWA Harvey-1 well is Pinjarra-1 (see Figure 70). However, the formation tops in the two wells are very different (see Figure 71) and therefore using the core test data taken from deep intervals in Pinjarra for shallow depths corresponding to GSWA Harvey-1 well may not be appropriate. In Table 8 the formation tops corresponding to GSWA Harvey-1 well are presented.

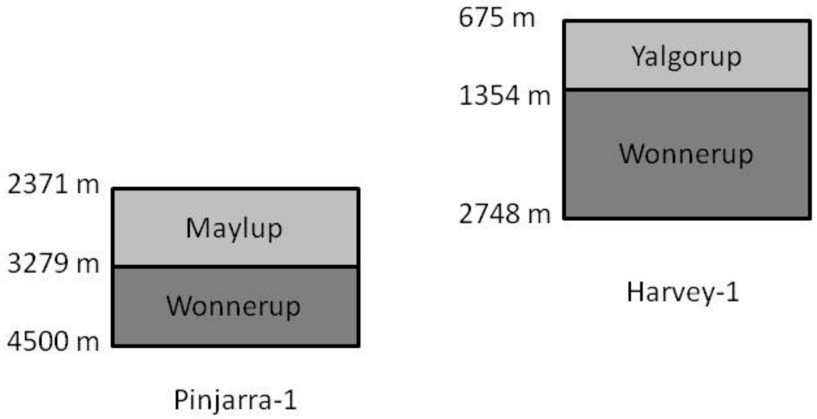

Figure 71: Comparison of top of Lesueur sandstone in Harvey-1 and Pinjarra wells.

Table 8: Formation tops for Harvey-1(AMSL-GL 19.1m, RTE 5.38m)

Formation	**Depth (m)**		
	MDRT	**TVDSS**	**Thickness**
Undifferentiated Warnbro Group	5.38	-19.1	194.6
Eneabba Formation	200.0	175	499.2
Lesueur Sandstone	699.2	674.7	2073.3
Yalgorup Member	699.2	674.7	679.0
Wonnerup Member	1378.7	1354.1	1393.9
Sabina Sandstone	2774.7	2748.0	165.8
Dry Hole T.D.	2945.0	2913.8	

From page 145 of “End of Well Geological Data Report”

4.2. Seismic data analysis

South Perth Basin has a complex geological structure with a number of large and small scale faults. Major faults are roughly oriented N-S. However, minor faults are observed to be oriented NE-SW. This may affect the maximum horizontal stress direction, locally, in wells drilled adjacent to these smaller faults. A complete fault analysis will be done in the ANLEC R&D project 7-1111-0201 “Integration of data from Harvey-1 well to support decisions”.

4.3. Petrophysical Logs and Deriving Rock Mechanical Properties

Petrophysical logs are used for formation evaluation and are also the main input for geomechanical modelling. Mechanical properties of the rocks surrounding a wellbore are derived from petrophysical logs and calibrated with laboratory measurements from core where core data is available. Formation density, compressional and shear sonic velocities are the main input parameters to develop the dynamic elastic modulii input to the model.

Dynamic elastic properties of rocks, including Young’s modulus (E_{dyn}), Poisson’s ratio (ν_{dyn}), Shear modulus (G_{dyn}) and Bulk modulus (K_{dyn}), can be estimated from shear and compressional sonic velocity through the following equations (Fjaer et al. 2008):

$$E_{dyn} = \frac{\rho V_s^2 (3V_c^2 - 4V_s^2)}{(V_c^2 - V_s^2)} \qquad \textbf{(kPa)} \qquad \textbf{(4.1)}$$

$$\nu_{dyn} = \frac{V_c^2 - 2V_s^2}{2(V_c^2 - V_s^2)} \qquad \textbf{(4.2)}$$

$$G_{dyn} = \rho V_s^2 \qquad \textbf{(kPa)} \qquad \textbf{(4.3)}$$

$$K_{dyn} = \rho (V_c^2 - \frac{4}{3} V_s^2) \qquad \textbf{(kPa)} \qquad \textbf{(4.4)}$$

Where ρ is density (g/cm^3), V_c and V_s are compressional and shear sonic velocity (m/s), respectively. These equations highlight the importance of acquiring shear sonic log data in any future planned wells in order to perform a more reliable rock mechanics study.

The shale-sand discrimination was performed based on the thresholds applied to the gamma-ray log. As seen from Figure 72 it appears that GR of 80 GAPI is a good threshold for separation between sandstones and shales. The two sections highlighted in this figure include large amounts of siltstone/claystone. The top section is within the Yalgorup member.

The petrophysical logs corresponding to GSWA Harvey-1 well are shown in Figure 73.

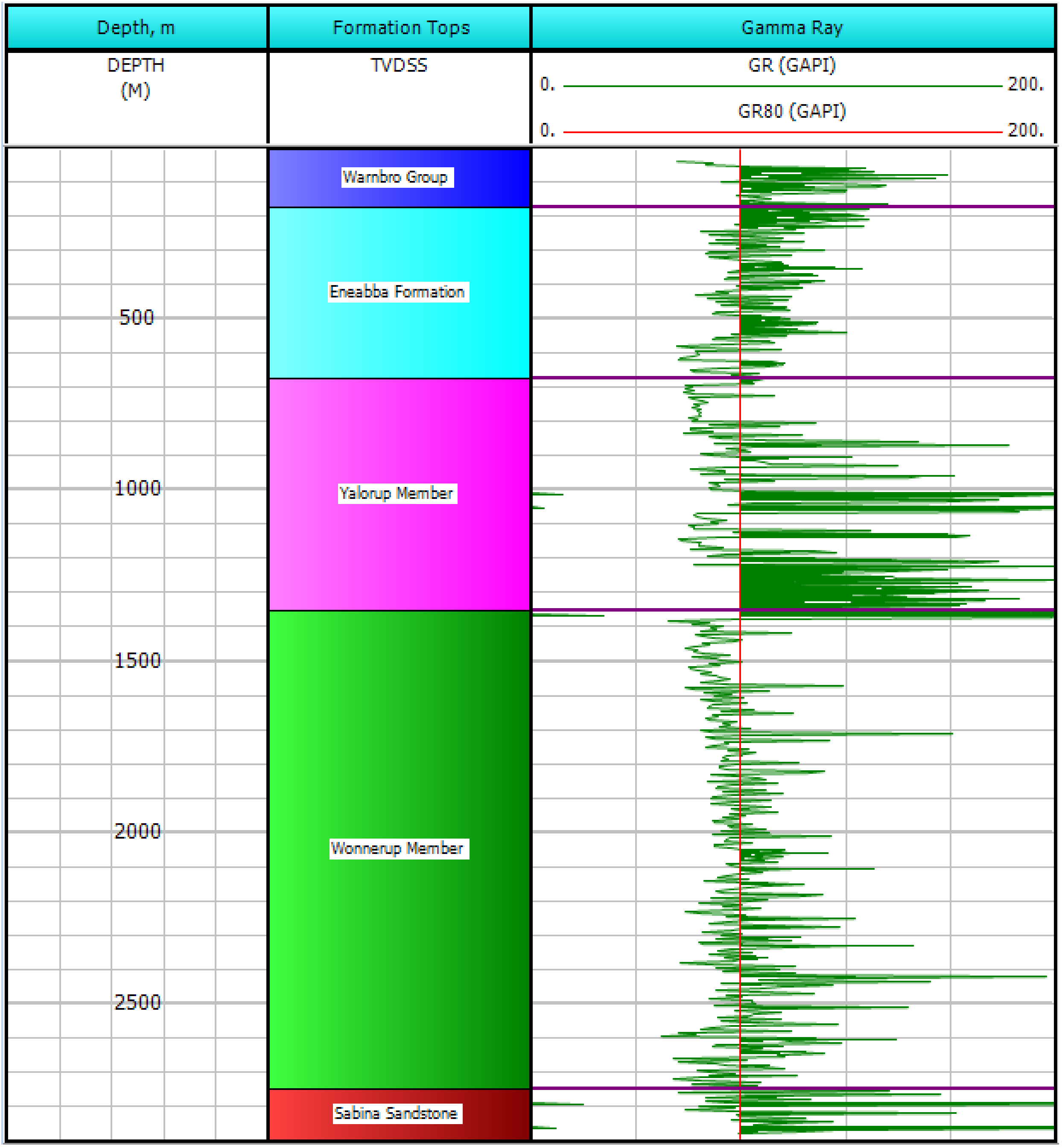

Figure 72: Shale-sand discrimination in Harvey-1 well.

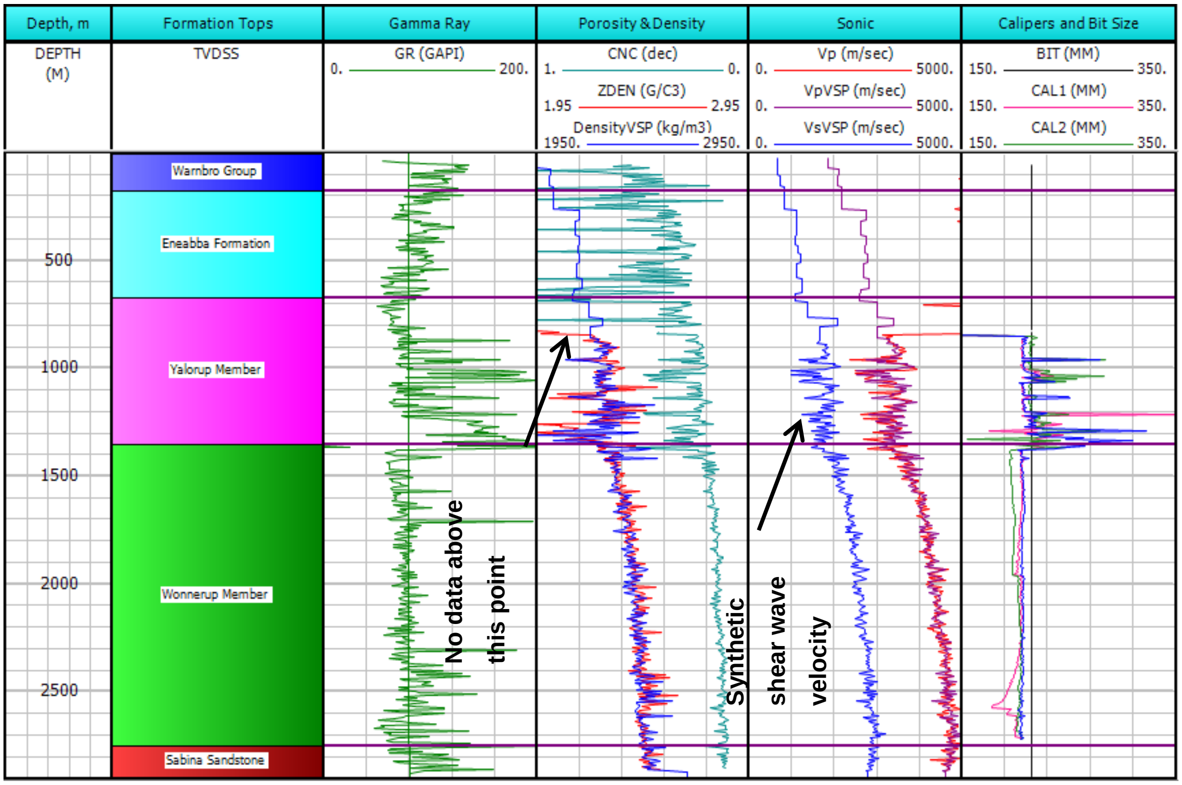

Figure 73: GR, density, porosity, compressional and synthetic shear velocity and calliper logs for Harvey-1 well.

At the depth of ~850-1370 meters, the increase of caliper readings indicates a zone of extensive washouts; these caliper readings are also supported with STAR tool images. These washouts can affect log readings in this depth interval. For our further analysis, we use volume compensated readings where possible. Furthermore, sonic log data are generally less affected with borehole washouts and when the density or neutron devices are useless, the density that calculated from velocity can still be reliable. In the case of Harvey-1 well, sonic velocities are in a good agreement with laboratory velocities where the later are available (ANLEC research project report "Facies-based rock properties distribution along the Harvey 1 stratigraphic well" ANLEC R&D project number 7-1111-0199). This fact implies that the sonic velocity readings are not strongly affected with the washouts. Density, which calculated using P-wave velocity from VSP at the shallow depth and sonic velocity at the depth below 850 m (shown with blue line in Figure 73 Porosity&Density tab), is in a good agreement with the density log (red line in Figure 73 Porosity&Density tab). GR readings can also be affected with washouts. However in our analysis, GR readings are only used for differentiation between shale and sandstone lithologies, which is confirmed with lithological descriptions from End of Well Geological Data Report (WADMP).

4.4. Drilling Events

The drilling operations have the effect of removing a cylindrical column of rock which previously carried the in-situ stresses. As a direct consequence of the removal of the column, the stresses will be redistributed in the vicinity of the bore hole (Figure 74a). In the vicinity of a vertical borehole, stress concentration is greatest in the direction of the minimum horizontal stress (e.g. Reinecker et al., 2003; Zoback, 2006; Fjær et al., 2008). The effects of stress redistribution, in terms of drilling events, can manifest itself in several ways.

If the stress magnitude exceeds the strength of the formation, shear failure is expected. This kind of failure is known as *borehole breakout*, as shown schematically in Figure 74b. In contrast, stress relaxation is observed in the direction of maximum horizontal stress. This relaxation can induce tensile stresses which may exceed the tensile strength of the formation and *induce fractures* in the wellbore wall. The fractures occurring in the wellbore wall due to tensile failure are known as drilling-induced fractures (Figure 74b).

These failures may cause different kinds of drilling incidents such as stuck pipe, over pull, loss of bottom hole assembly, etc. Such incidents result in increased costs and lost time in a drilling operation. In order to predict and prevent such events, studying the history of the previously drilled wells in the same field is helpful to understand problematic formations.

Other drilling incidents, such as well kicks and drilling fluid losses, are well known to drillers and can be very time consuming. An inappropriate mud weight can result in such incidents. Some drilling equipment (e.g. blow out preventers) is installed on a rig to prevent accidents which follow borehole failure, however, knowing the pore pressure and fracture pressure profile of the planned well prior to drilling helps to optimize the mud weight program and prevent kicks and losses.

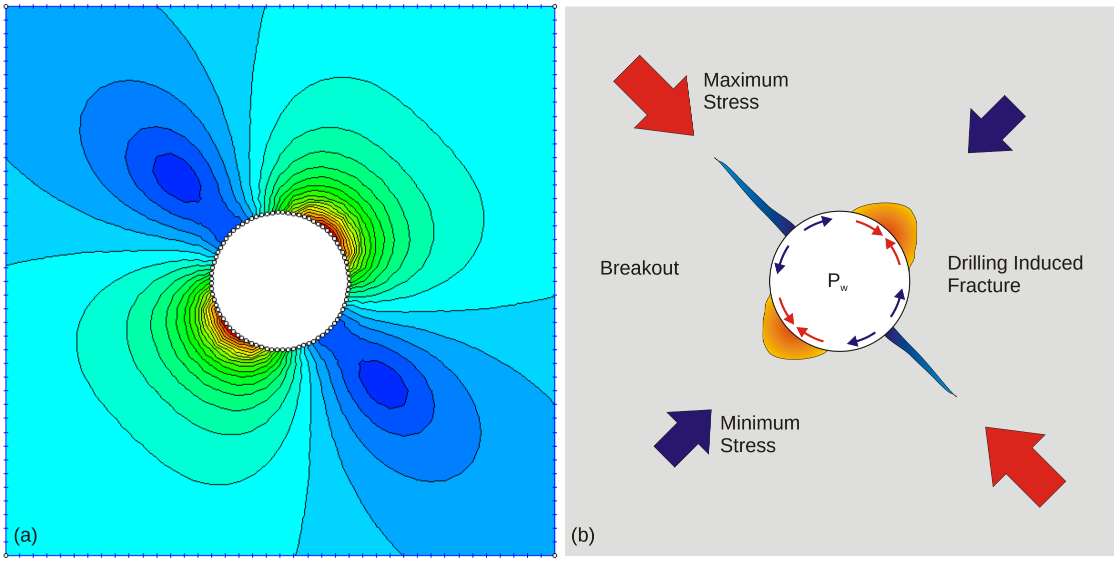

Figure 74: Stresses and failures around a vertical wellbore (a) maximum stress disturbance in a horizontal plane around wellbore, (b) failures occurred in wellbore wall in respect to the maximum and minimum horizontal stress directions.

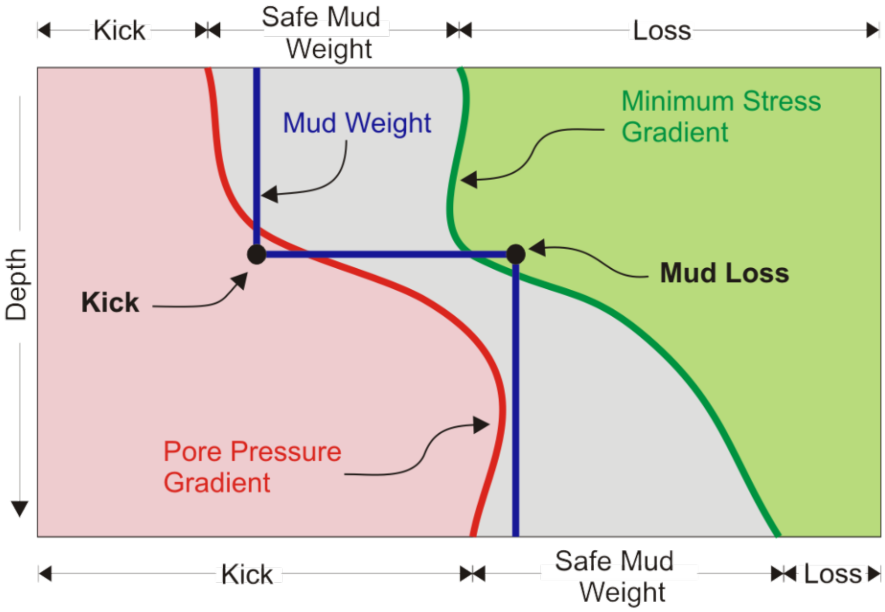

Figure 75: Demonstration of Kick and Loss mechanism.

The mechanisms of kick and loss occurrences are quite simple. The well flows when the mud weight is less than the pore pressure gradient. When the mud weight exceeds the minimum stress gradient of the formation, mud loss occurs. This concept is shown in Figure 75. Accordingly, the pore pressure gradient and minimum stress gradient can be introduced as the lower and upper limits of the safe mud weight window.

Figure 76 shows the mud weight that is used for drilling at each depth and graphically summarises drilling activities of GSWA Harvey-1 well. From this figure it is seen that most of the drilling events and incidents are associated with the Yalgorup member (i.e. above 1500m). This can be considered a geomechanics related problem as the petrophysical logs in this formation indicate weaker responses comparing to the lower Wonnerup member. The figure also shows the depth of a leak-off test in GSWA Harvey-1 well.

Leak-off tests (LOT's) are pressure integrity tests in which the borehole pressurization continues until the pressure at which the pressure increase rate declines. This indicates a fluid leak-off in the formation and called leak-off point (LOP). Tests during which the pressurization phase continues beyond the formation breakdown pressure (a maximum pressure reached in the test) and which performed with several pressurization cycles are called extended leak-off tests (XLOT's). Leak-off tests and extended leak-off tests are used to determine the least principal stress in the formation. In the case of the pressure integrity test in GSWA Harvey-1 well, the leak-off point has not been reached and so for we might say that a limit test or formation integrity test (FIT) was conducted. Thus, the maximal wellbore pressure reached during the LOT did not exceeded the least principal stress or was not sufficient to initiate a fracture. A LOT or XLOT instead of FIT would allow constraining a maximum value or determine the least principal stress, however, such tests could not be done for safety reasons.

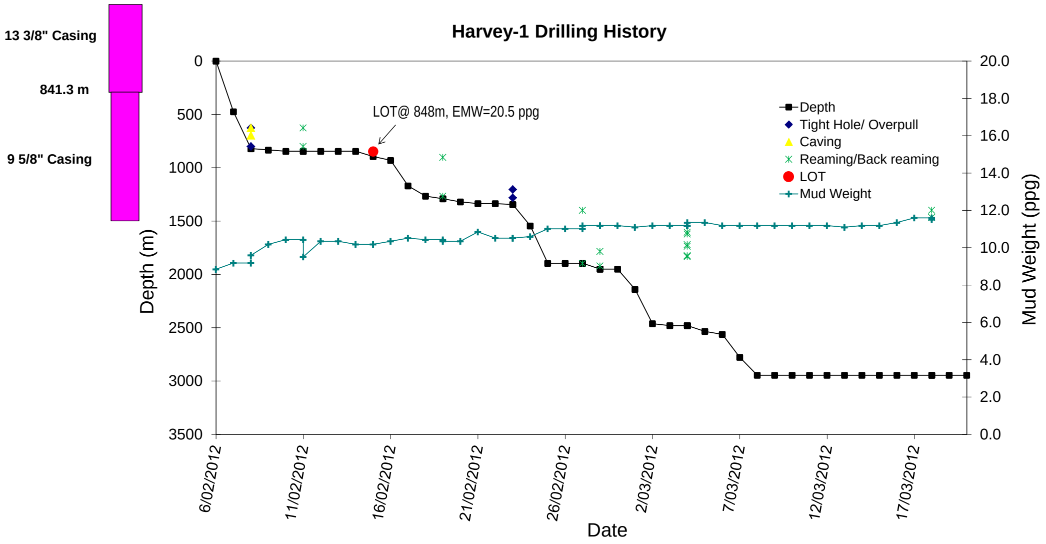

Figure 76: Depth verses time drilling activity of GSWA Harvey-1 well.

4.5. Rock Mechanical Modelling

The processes involved in the construction of a Rock Mechanical Model (RMM) are illustrated in Figure 77. These include a detailed review of all available data, including seismic, drilling, and geology. These data are combined with petrophysical logs to distinguish formations with respect to their mechanical properties and extract elastic and strength properties as well as in-situ stresses, pore pressure and the magnitude of the maximum horizontal stress. The continuous logs obtained are then calibrated against available core testing in the laboratory and downhole test results. Rock elastic properties (Young's modulus, *E*) or formation strength (Uni-axial Compressive Strength, *UCS*) can be obtained from tri-axial tests conducted on core samples in the laboratory. The minimum horizontal stress curve could be compared with the results of LOT's performed at specific depths. The details of the work flow steps involved in building a RMM are illustrated in, below.

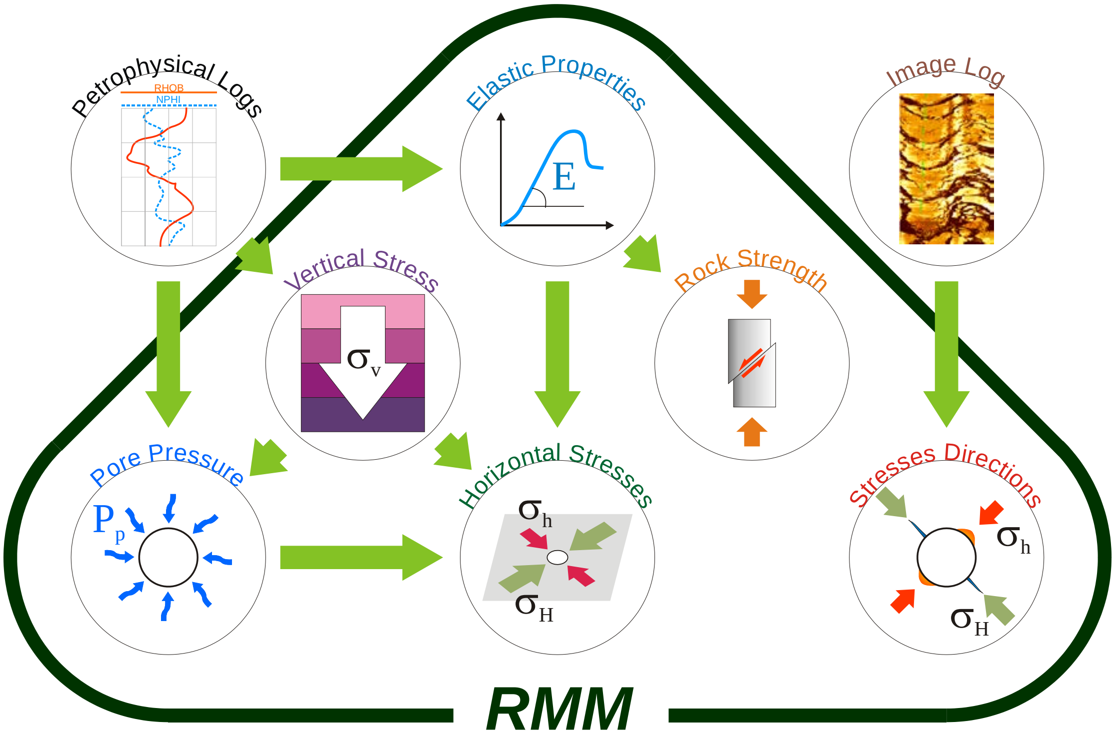

Figure 77: Work flow used to build a Rock Mechanical Model.

4.5.1. Mechanical properties

Different rocks can respond differently under similar stress conditions. The properties and parameters which define the behaviour of a material are known as the mechanical properties. The amount of rock deformation under varying force levels is predictable as are the maximum forces that are sustainable without deformation. The methodology to extract these data from logs is discussed in the following sections.

Elastic properties

The rate of deformation and strain in a material is a function of the static elastic property of the material. The static elastic properties cannot be measured directly from logs, but the dynamic elastic properties can be calculated using equations 4.1 to 4.4.

These dynamic moduli represent the response of the rocks under a dynamic load, (e.g. for sonic waves). The dynamic elastic moduli are in the order of 2 to 5 times greater than those under static load, known as static elastic moduli, as depicted in Figure 78.

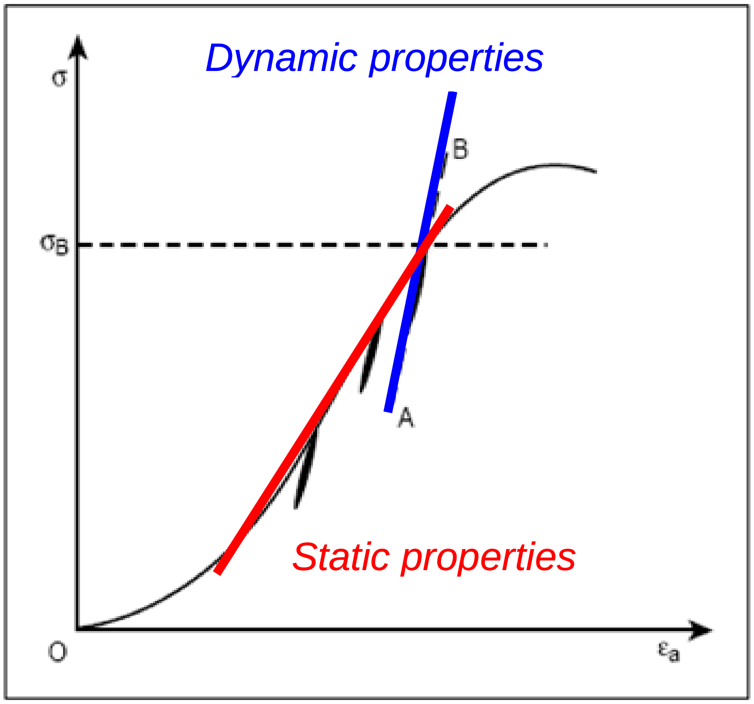

Figure 78: Dynamic versus static elastic moduli.

Numerous correlations have been developed to estimate the static modulus from dynamic modulus. Most of them are based on the limited core tests conducted in a specific area and field. In the GSWA Harvey-1 well study the shales and sand formations use the modified Morales correlation to estimate the static elastic modulus from the dynamic modulus as

$$E_{sta} = (-2.21 \times Effective \quad Porosity + 0.963)E_{dyn}. \tag{4.5}$$

The static Poisson ratio was considered to be equal to the dynamic Poisson's ratio other moduli to be calculated based on the following equations

$$G_{sta} = \frac{E_{sta}}{2 \cdot (1 + \nu_{sta})}, \tag{4.6}$$

$$K_{sta} = \frac{E_{sta}}{3 \cdot (1 - 2\nu_{sta})}. \tag{4.7}$$

In equations 4.5-4.7, E_{sta}, K_{sta}, G_{sta} and ν_{sta} are Young's, bulk, shear static moduli and Poisson's ratio, respectively.

In order to consider the poro-elastic behaviour of the rock, the poro-elastic coefficient, known as the Biot coefficient (α), also needs to be taken into account. The Biot coefficient is defined as

$$\alpha = 1 - \frac{K_m}{K_g}, \tag{4.8}$$

where K_m is the matrix bulk modulus and K_g is the grain bulk modulus of rock. The Biot coefficient of the formation was conservatively assumed to be 1 in this study.

The estimated static elastic properties corresponding to GSWA Harvey-1 well are illustrated in Figure 79.

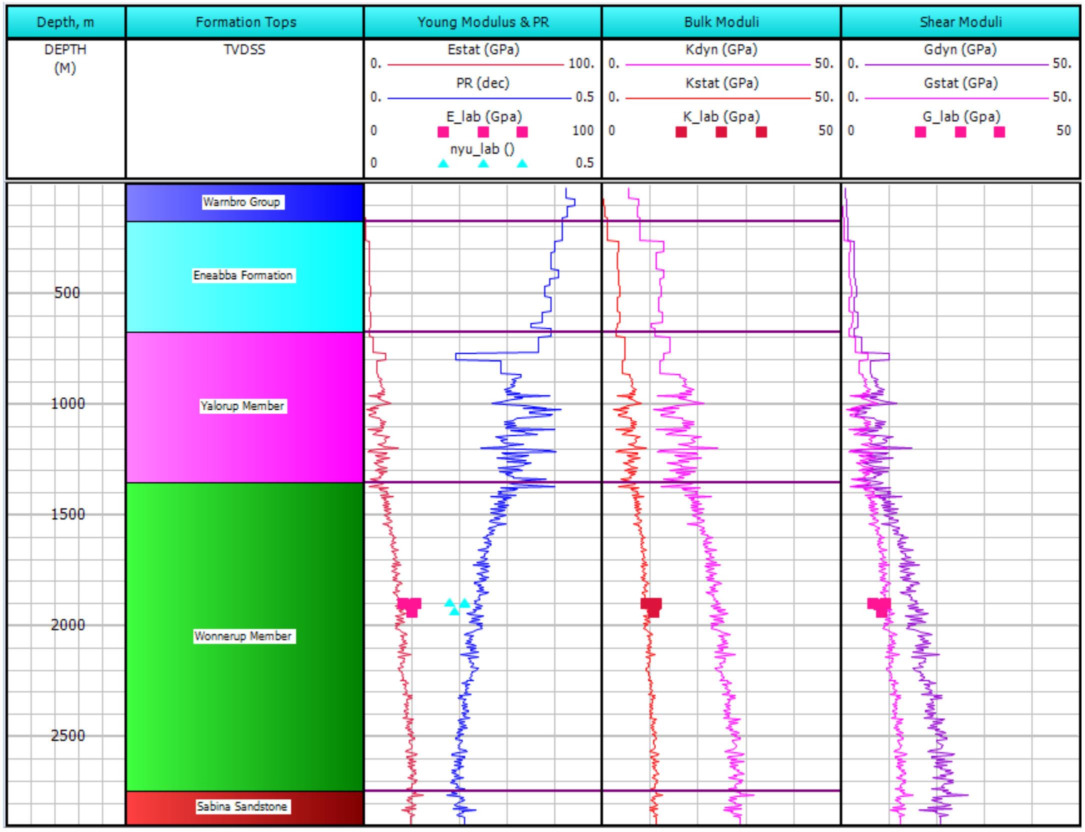

Figure 79: Estimated vs. measured elastic properties of GSWA Harvey-1 well.

Rock strength parameters

The formation fails as the stresses exceed the rock strength. Based on the Mohr-Coulomb criteria, the rock strength parameter can be defined from the uni-axial compressive strength (*UCS*), internal friction angle (ϕ) and tensile strength of the rock (T_0). The Mohr-Coulomb failure criterion, in the form of principal stresses, is expressed as:

$$\sigma_1 = UCS + \sigma_3 \frac{1+\sin\phi}{1-\sin\phi}, \tag{4.9}$$

where σ_1 and σ_3 are the maximum and minimum stresses, respectively.

The strength parameters are generally obtained from core tests in the rock mechanics laboratory. In order to derive a continuous curve, along the wellbore trajectory, correlations are used based on the physical or elastic properties of the formation. Numerous correlations are available in the literature, which are derived from data from different areas and fields to obtain the *UCS* of the rocks. The Bradford correlation (Bradford et al., 1998) was used to estimate the *UCS* in sand and shale formations in this study. The correlations is in the form of

$$UCS = 2.28 + 4.1089 E_{sta}\,. \qquad \text{(MPa)} \tag{4.10}$$

A linear dependency of tensile strength on UCS is generally observed in experimental studies (for more details see Fjær et al., 2008). Tensile strength (T_0) of the rock is usually estimated as 1/10 to 1/15 of its *UCS*. In this study the tensile strength is assumed to be 1/10 of the *UCS* for GSWA Harvey-1 well.

The internal friction angle of rock is estimated based on the volume of shale and porosity. The volume of shale was derived from the gamma-ray log as:

$$V_{Shale} = \frac{(GR_{\log} - GR_{\min})}{(GR_{\max} - GR_{\min})}. \tag{4.11}$$

The internal friction angle is then estimated from the Plumb (1994) correlation as:

$$\phi = 26.5 - 37.4(1 - Porosity - V_{shale}) + 62.1(1 - Porosity - V_{shale})^2\,. \tag{4.12}$$

The tensile strength follows a similar trend as *UCS* profile.

The rock strength properties of Harvey-1 well, obtained from the procedure explained above, are shown in Figure 80. The results indicate that the Yalgorup member is much weaker in terms of strength than the Wonnerup member.

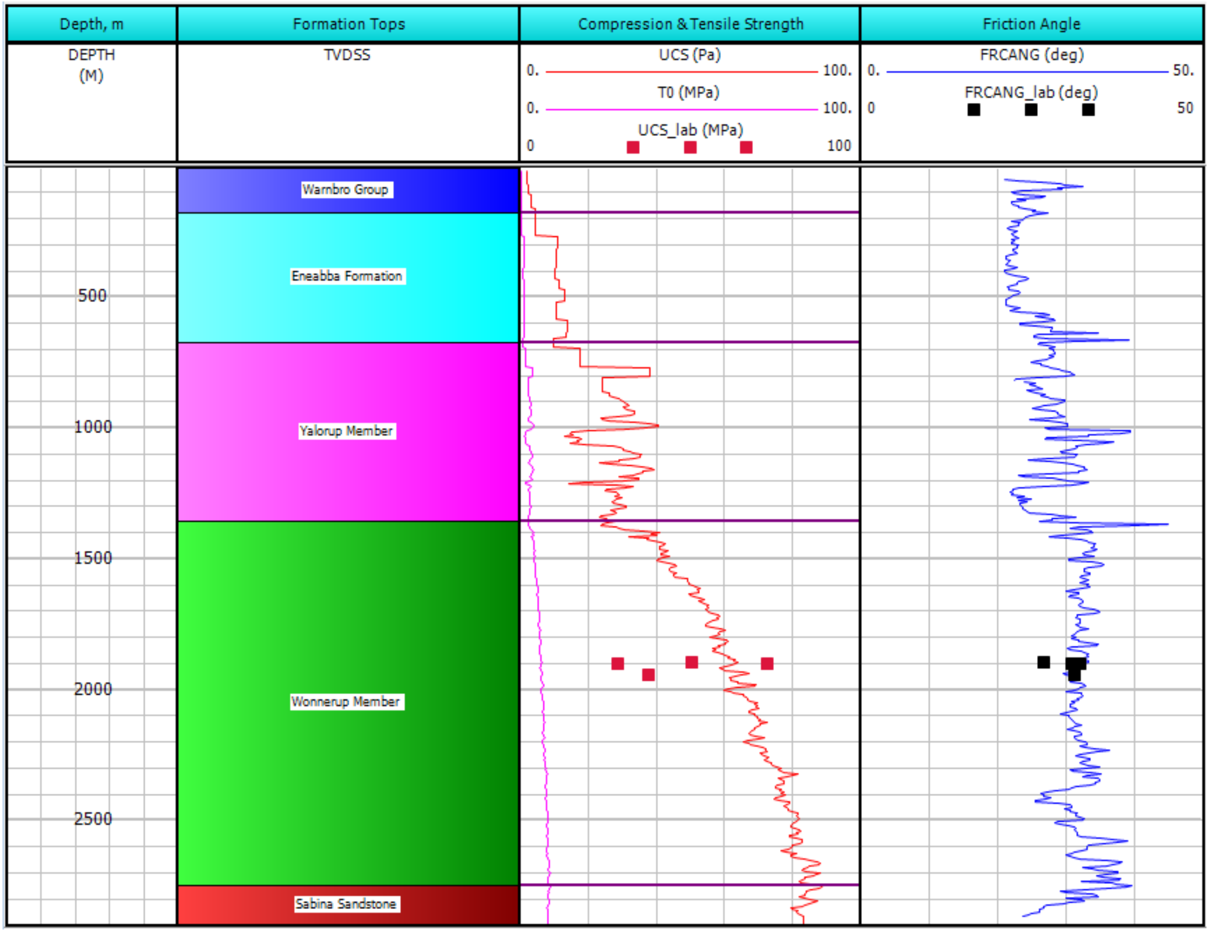

Figure 80: Estimated vs. experimentally measured mechanical properties of Harvey-1 well.

4.5.2. In-situ stresses and pore pressure

Forces applied to the formation are usually expressed in terms of stress or pressure. Oil and gas wells are considered as being drilled near a free surface (the earth's surface). Taking into account that the principal stresses are parallel and perpendicular to free surfaces, it is conceptually convenient to consider the principal stresses as a vertical stress (σ_V) and two horizontal stresses (σ_h and σ_H), as depicted in Figure 81.

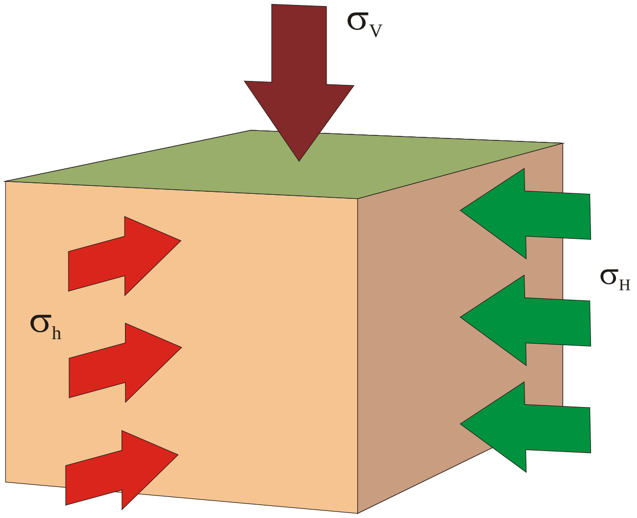

Figure 81: The general state of stresses near surface of earth.

In the following sections the methodology to obtain the magnitude and direction of these stresses are discussed in detail.

Vertical stress

Vertical stress is one of the principal stresses. This stress is the lithostatic weight or the combined weight of overlying layers. It is also known as overburden stress. The overburden stress is directly calculated from the density log, as the integration of the density of different formation layers, as:

$$\sigma_v = \int_{Surface}^{TVD} \rho g dh \tag{4.13}$$

Wireline density log measurements, where available, are used to estimate the bulk density of sediments. As the density from log measurements is only available from the depth of 825m at the GSWA Harvey-1 well, the density of formation at shallower part is estimated using Gardner's velocity-density relations for sandstones (Gardner et al., 1974). Castagna et al. (1993) provided a very good summary of the topic. Gardner gave polynomial and power-law forms of density-velocity relation as follows:

$$\rho = -0.0115V_P^2 + 0.261V_P + 1.515 \tag{4.14}$$

and

$$\rho = 1.66V_P^{0.261}. \tag{4.15}$$

Here ρ is bulk density in g/cm^3 and V_P is compressional velocity in km/s. The equations are proved to be accurate for the velocity range of 1.5-6.0 km/s.

A cross plot of compressional velocity vs. density using the log data from Harvey-1 well is shown in Figure 82 in comparison with Gardner's relation in polynomial (red) and power-law (magenta) form. These two forms of Gardner's relations are in a good agreement with each other and describe a velocity-density relation in the Harvey-1 well. For certainty, we hereafter use the power-law relation to estimate bulk density from compressional velocities.

For the upper 850 m of the Harvey-1 well, where sonic log measurements are not available, the density is calculated from VSP velocities and below 825 m the density is estimated from sonic log velosities. The compressional velocity and density vs. depth are shown in Figure 83. The estimated bulk density in a good agreement with the measured one for the whole interval where the wireline density log measurements are available.

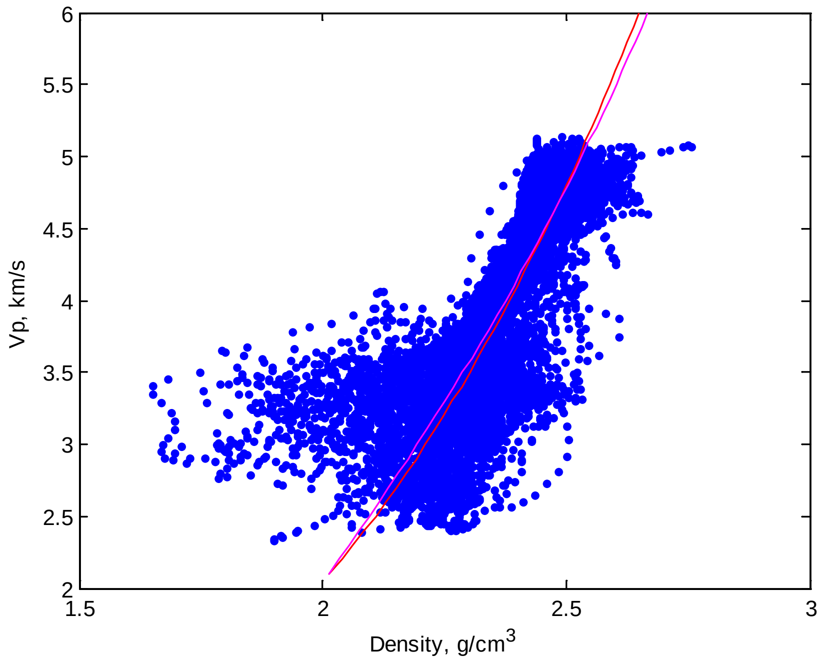

Figure 82. Compressional velocity vs. density cross-plot for Harvey-1 well in comparison with Gardner's polynomial (magenta) and power-law (red) relations for sandstones

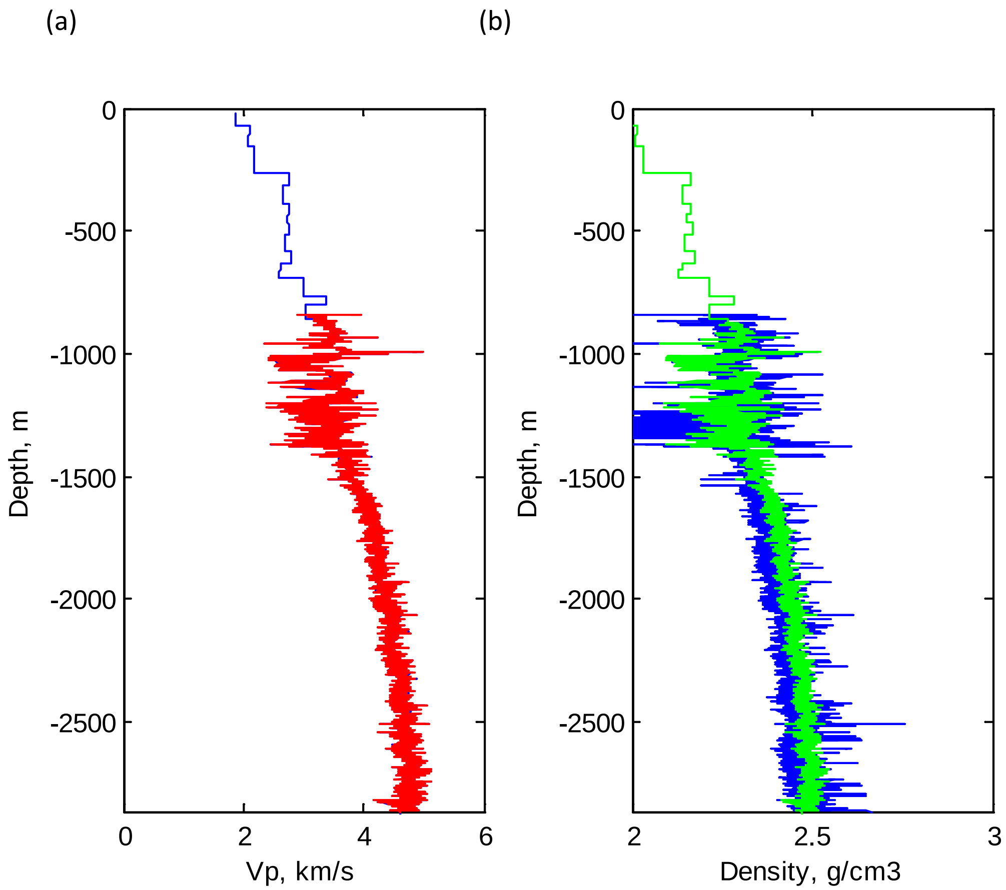

Figure 83. Estimation of the bulk density from velocity: (a) Compressional velocity, VP, measured by sonic log (red) and estimated from VSP (blue); (b) Wireline density log measurements (blue) and bulk density estimated from velocity (green).

Pore pressure

Pore pressure provides an estimate of the lower limit of the mud weight that should be used in the wellbore during drilling to ensure no blowouts or kicks in the well thus it is a critical value to be determined. Estimation of the pore pressure profile prior to drilling the well is not usually straightforward.

Several methods have been developed to estimate the pore pressure profile based on the drilling parameters measured while drilling (D-Exponent), resistivity, sonic and seismic data, etc. However, all estimations of pore pressure have to be calibrated against the field observations such as, drill stem tests and wireline formation pressure tests.

Modular Formation Dynamics Tester (MDT) measurements exhibit a normal pore pressure regime throughout the whole depth of observations from about 800 to 2500 m with pore pressure gradient of 9.8 kPa/m. It is well known that while MDT measurements are reliable in permeable formations they can be irrelevant in low permeable shales. However, indirect indicators of overpressure (such as abnormally low density and/or velocities) are also lacking in the Harvey-1 well even in the low permeable Lesueur sandstone formation. Generally, compressional and shear velocities are sensitive to pore pressure and are significantly lower in overpressured zones. In the case of GSWA Harvey-1 well, laboratory velocities measured in fully saturated samples in drained condition (at zero pore pressure) are in a good agreement with sonic log velocities as reported in Facies-based rock properties distribution along the Harvey 1 stratigraphic well (ANLEC R&D project number 7-1111-0199). Moreover, the volume compensated density log (Figure 73) exhibits a continuous increase of the density with the depth increase. Additionally, hydraulic permeability measured on core samples from Lesueur sandstone formation is relatively high; it ranges from more than 1 Darcy to 0.5 mD with just a few low permeable samples which exhibit permeability below 0.01mD. Details of core sample selection, characterization and permeability measurements can be found in ANLEC R&D project number 7-1111-0199 report (note that this report was not completed at the moment when the current report has been written). Based on the available information, a normal pressure regime was considered in this study and the pore pressure curve was constrained with the MDT pressure data as shown in Figure 84. However, further work should be done to completely exclude possibility that Yalgorup Member of Lesueur Formation is overpressured.

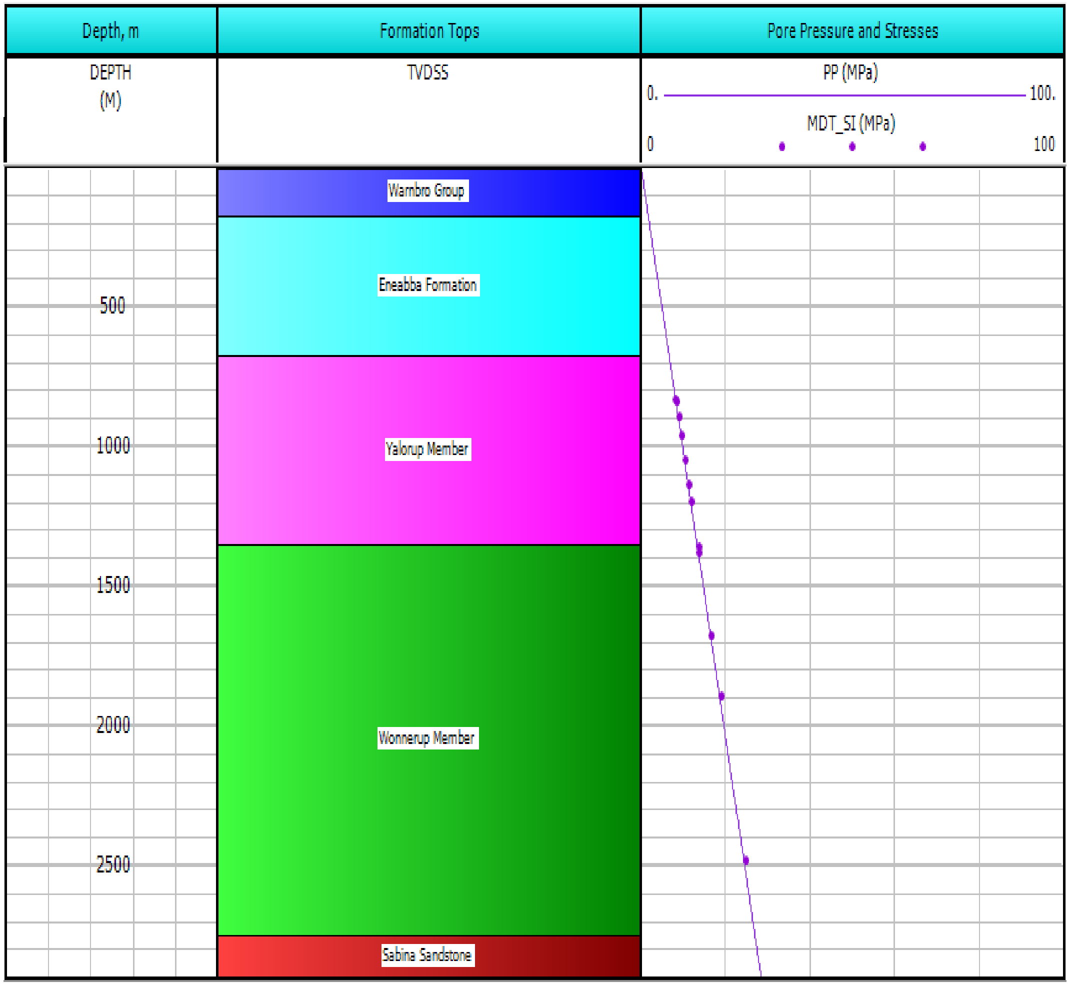

Figure 84. Pore pressure profile of Harvey-1 well.

Horizontal stress magnitudes

The horizontal stresses are originally generated from the formation's lateral strains created by vertical stress. In a homogenous and isotropic environment, assuming that the rock behaves elastically, the horizontal stresses can be predicted from the overburden stress through the Poisson ratio effect as:

$$\sigma_h = \frac{\nu}{(1-\nu)} \cdot \sigma_v \, . \qquad \textbf{(4.16)}$$

A better estimation of horizontal stresses could be made if the poro-elasticity behaviour of the rock and tectonic forces are taken into account. In this case, the following equations can be used to calculate the horizontal stresses

$$\sigma_h = \frac{\nu}{(1-\nu)} \cdot (\sigma_v - \alpha \cdot P_p) + \alpha \cdot P_p + \frac{E_{sta}}{(1-\nu^2)} \cdot (\varepsilon_x + \nu \cdot \varepsilon_y) \qquad \textbf{(4.17)}$$

$$\sigma_H = \frac{\nu}{(1-\nu)} \cdot (\sigma_v - \alpha \cdot P_p) + \alpha \cdot P_p + \frac{E_{sta}}{(1-\nu^2)} \cdot (\varepsilon_y + \nu \cdot \varepsilon_x) \, , \qquad \textbf{(4.18)}$$

where ε_x and ε_y account for the horizontal stress anisotropy.

Only one LOT was available from the Harvey-1 well giving an estimated leakoff value of 20.5 ppg at a depth of 848 m was used to calibrate the minimum horizontal stresses. The maximum horizontal stress was then calibrated based on the calipers response in terms of breakouts and the image logs.

The horizontal stresses estimated for Harvey-1 well using equations 4.16 and 4.17 are plotted in Figure 87. In general It is seen that a strike-slip stress regime is dominant in the studied well as the order of stress magnitudes is SH>SV>Sh. However, at shallower depths of less than 900m the stress regime tends to become reverse, i.e. the vertical stress becomes the minimum stress: this is also in agreement with the value of the LOT data.

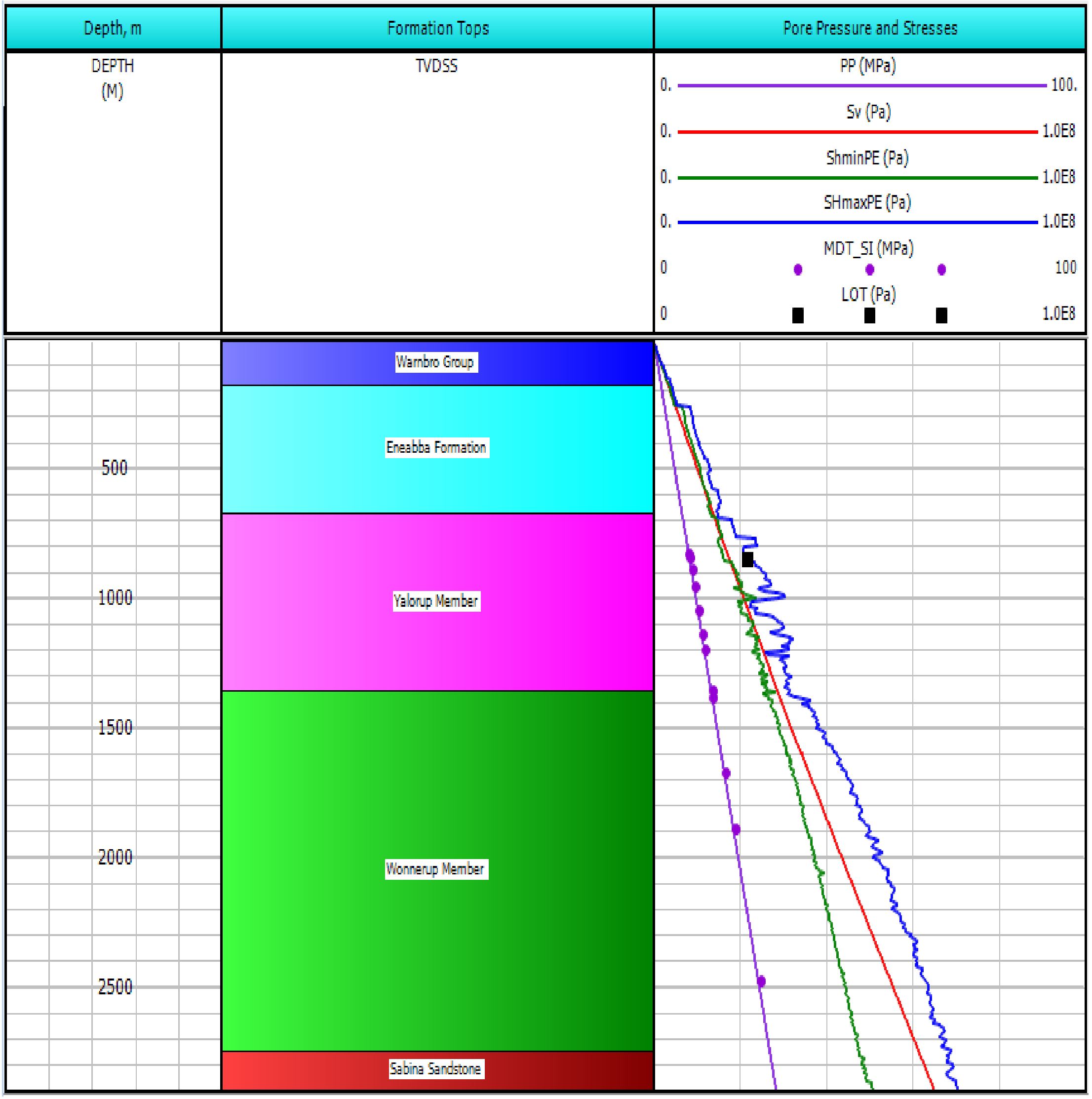

Figure 85. Magnitude of pore pressure, vertical and two horizontal stresses in HARVEY-1 well.

4.6. Wellbore stability analysis and history matching

The shear strength of rock can be estimated through its linear relation with elastic properties, i.e. cohesion (*c*) and friction the angle (ϕ) from well-known Mohr-Coulomb failure criteria equation:

$$\tau = c + \sigma_n \tan\phi . \tag{4.19}$$

This is the original form of Equation 4.9. It shows the rock failure envelope plots as a straight line with intercept *c* and slope tanϕ. A graphical representation of the rock failure envelop is shown in Figure 86, where the area below the failure envelope is the stable region. As cohesion and friction angle of the rock increases, the stable region expands. However, as can be seen from equation 4.9 and 4.18 that stresses may influence the condition of formation failure. The state of stresses can be illustrated in the same plot, in Figure 86 as a circle with diameter of σ_θ - σ_r with σ_θ and σ_r being the hoop (tangential) and radial stresses induced around the wellbore after drilling. The maximum shear stress induced in the rock due to these two stresses would be equivalent to the radius of the represented circle, i.e. $(\sigma_\theta + \sigma_r)/2$ as can be seen in Figure 86. In the situation where this point of maximum shear stress touches the rock failure envelope the rock is subjected to enough stress contrast to fail. This implies that the larger the stress anisotropy, the more prone the rock will be to failure under shear mode. Also, from Figure 86 it can be recognised that the stress difference has a more significant effect on rock failure than the stress magnitudes: two very large stress magnitudes represents a small circle located far from the *x* axis, whereas two small stress magnitudes with large difference represents a large radius circle close to the origin with a higher possibility of touching the rock failure envelope.

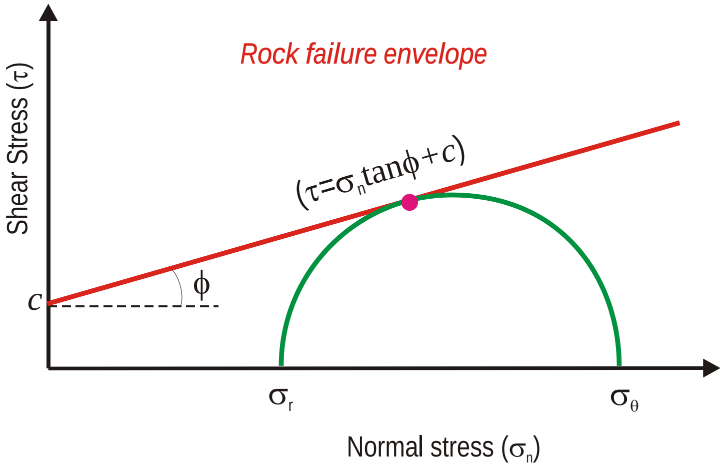

Figure 86. Representation of rock failure envelope and induced stresses

This discussion demonstrates that both rock strength properties and induced stresses are to be considered when rock failure or wellbore instability assessments are being conducted. Misleading results may be obtained if induced stresses are not included. For example, from inspection of Figure 86 it is easy to realise why it is possible to observe failure in a very competent formation if the stress applied differences are large enough. Conversely a weak formation may maintain its integrity if the applied stresses are isotropic.

The stresses induced around a wellbore are also a function of the wellbore pressure. In fact, the mud weight can control the magnitude of the hoop (σ_θ) and radial (σ_r) stresses. Inappropriate mud weight may result in formation instability.

The instabilities associated with a different range of mud weights are illustrated diagrammatically in Figure 87. Four different limits can be distinguished across the mud weight window. The red shaded area (left most) shows low mud weight associated with a kick where the limit, or kick point, is defined at the pore pressure. The second zone, the orange shaded area, represents the mud weight associated with borehole breakouts. The green and black shaded areas show, respectively, the mud losses and drilling induced fractures corresponding to increasing mud weights Losses occur when mud weights are higher than the minimum principle stress, corresponding to the left boundary of the green shaded area. The central, grey area, between the breakout mud weight and the mud weight corresponding to mud loss, represents the *stable mud weight window*. The *safe mud weight window* is situated between the kick and loss thresholds.

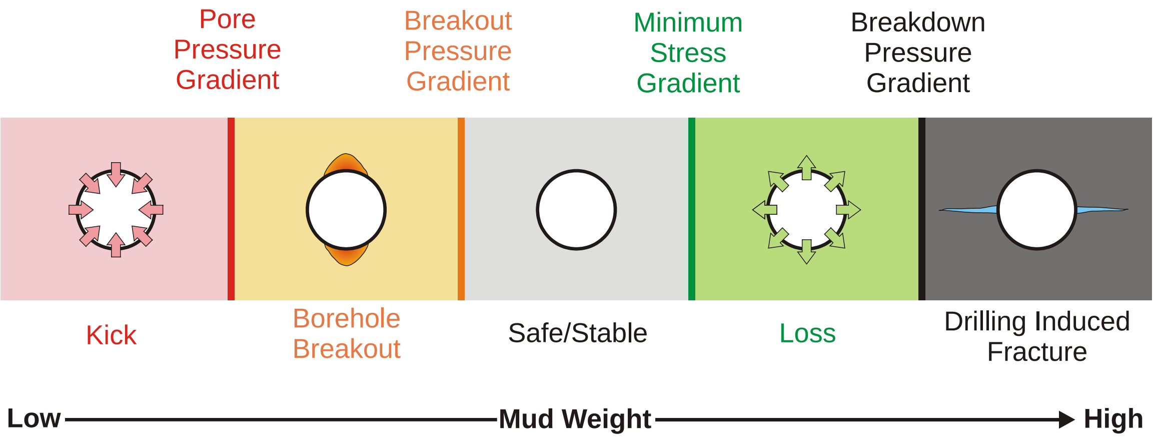

Figure 87. Instabilities mechanisms observed in different mud weight windows

Wellbore stability analysis was conducted for GSWA Harvey-1 well. The mud weight associated with kicks, breakouts, losses and drilling induced fractures are plotted along the wellbore trajectory in Figure 88 corresponding to the Harvey-1 well.

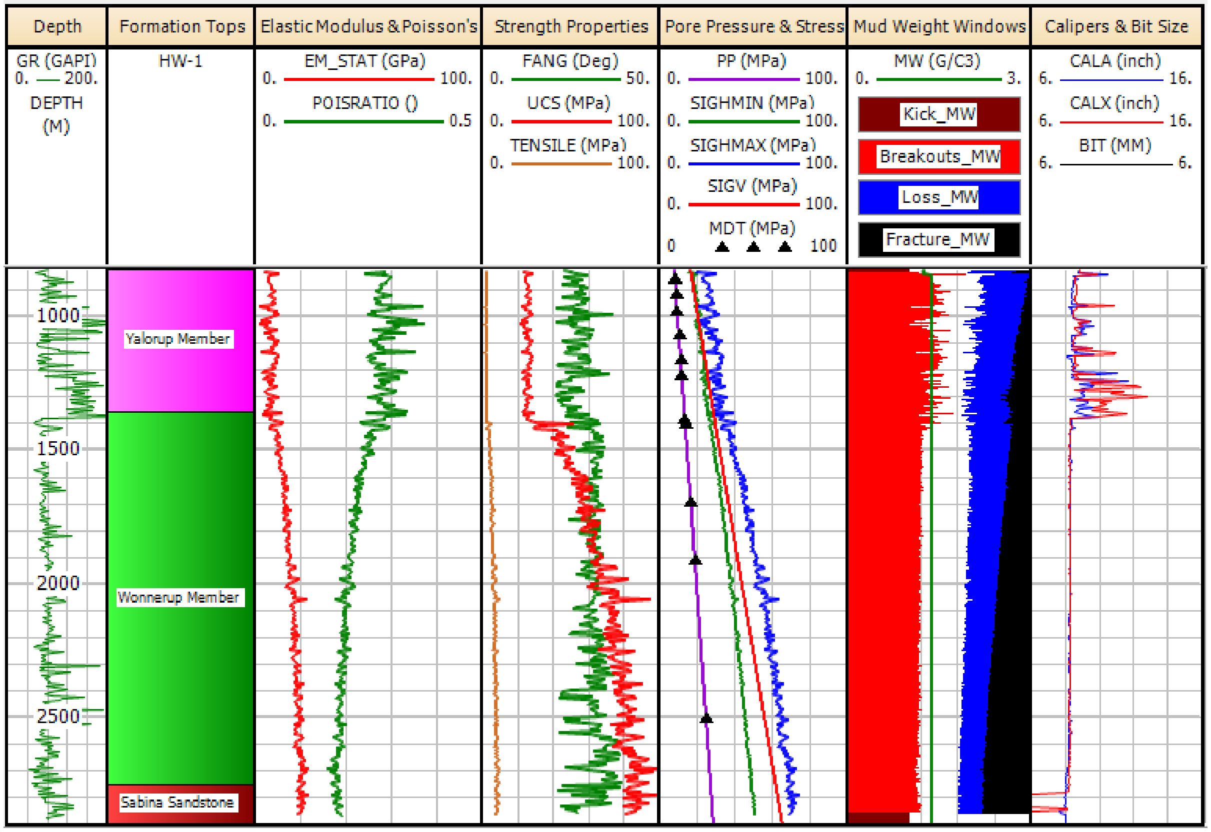

Figure 88: Rock mechanical model and wellbore stability analysis for Harvey-1 well.

4.7. Estimation of maximum horizontal stress orientation

Estimates of the stress field orientation can be obtained from borehole data. Specifically, borehole breakout analysis is a routinely applied technique in order to estimate the direction of the maximum horizontal stress (e.g. Zoback, 2007). Prior knowledge of stress field orientation in the Perth Basin is also mainly based on borehole breakout analyses. A good summary is given by King et al. (2008); see also Figure .

There is an overall east-west orientation for the maximum horizontal stress. However, local variations have been observed. Lake Preston-1 is the closest nearby well site from which maximum horizontal stress direction has been determined (Van Ruth, 2006; Barclay, 2009; see also Figure).

It is the aim of this activity to estimate the stress field orientation using the well log data acquired at the Harvey-1 well site. Its location is indicated in Figure .

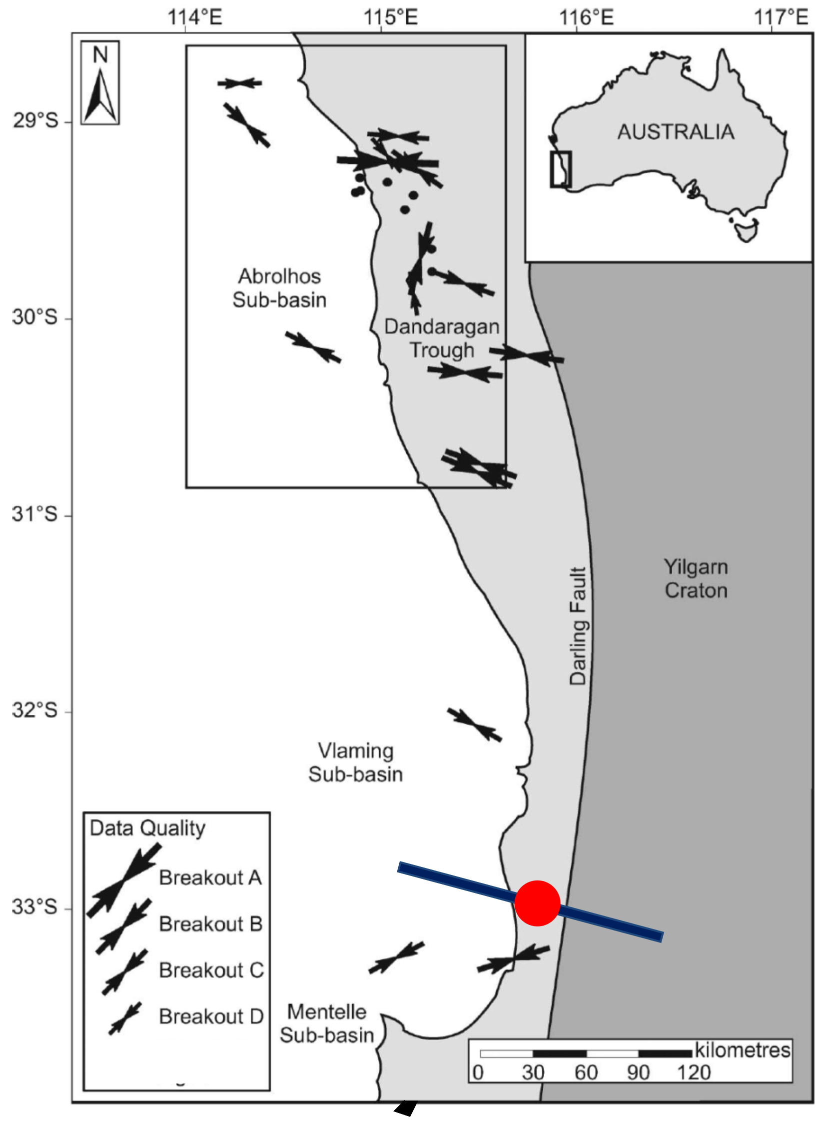

Figure 89. Data compilation of maximum horizontal stress orientation for the Perth basin after King et al., 2008 (see their Figure 1). The red dot indicates location of the Harvey-1 well site (latitude: 32 59 S, longitude: 115 46 E). The thick blue line corresponds to the direction of maximum horizontal stress found from the borehole breakout analysis within this project.

4.7.1. Principles of borehole breakout analysis

Identifying well bore enlargement zones from calliper data yields an estimate of the minimum horizontal stress direction. This is done by associating the long axis of the borehole enlargement with the direction of the minimum horizontal stress (Figure). For vertically wells the direction of the maximum horizontal stress is then perpendicular to the direction of the long axis of enlargements.

We follow the breakout analysis as suggested in Reinecker et al. (2003). Though this analysis is based on four-arm calliper data, the interpretation criteria for the six-arm calliper data are formulated accordingly. A breakout (zone) is counted if

a) there is no tool rotation in the zone of enlargement,
b) there is a tool rotation into and out of the zone of enlargement,
c) the smaller calliper reading is close to the bit size,
d) calliper difference exceeds bit size by 10%,
e) length of the enlargement zone vertically up the well bore should exceed 1m.

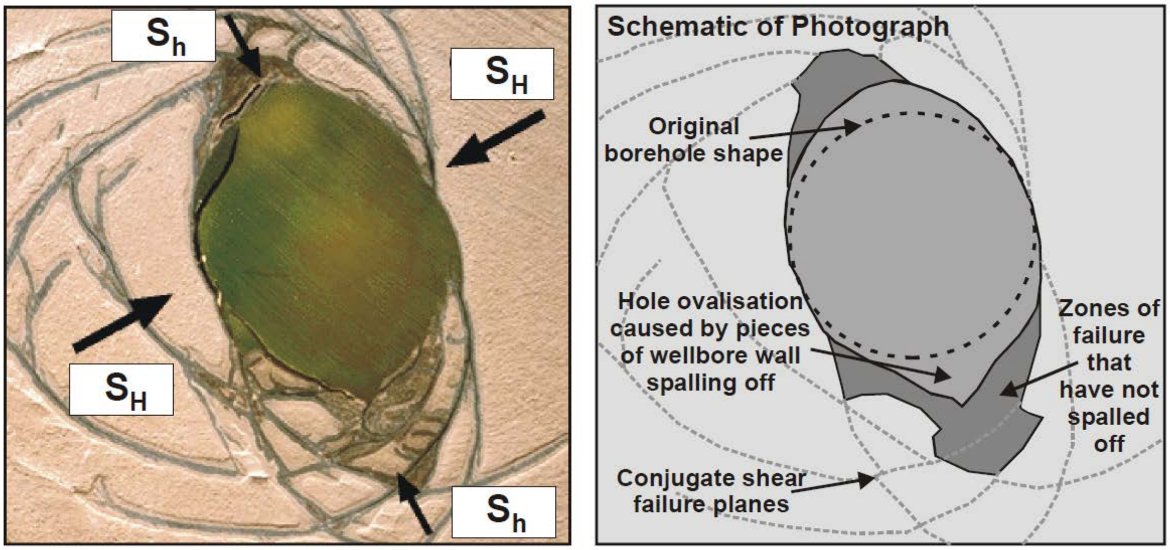

Figure 90. Results of a hollow cylinder laboratory test simulating borehole breakout. Intersection of conjugate shear failure planes results in enlargement of the cross-sectional shape of the wellbore (further details in Reinecker et al., 2003). SH and Sh refer to the maximum and minimum horizontal stress, respectively.

4.7.2. Results for the Harvey-1 well

The following breakout analysis is based on the six-arm calliper data and the azimuth log data of the Baker Hughes STAR Imager^{TM}. It also provides high-resolution resistivity formation images which are not used here. The Circumferential Borehole Imaging Log (CBIL, also trademark of Baker Hughes) data are used for guidance. It creates images of the borehole wall using an acoustic transducer.

We identified a total of 21 breakout zones that satisfy the interpretation criteria a, c-e set out in the previous section. A tool rotation into and out of the enlargement zone has not been observed for any of the 21 zones. Examples of two identified breakout zones are shown in Figure . In one case there is an increase in calliper 2, in another case there is an increase in calliper 1.

Eighteen breakout zones are within the depth interval 1250-1370m and only 3 breakout zones could be identified in the shallower depth interval 1050-1150 m. Outside of these depth intervals a few breakout candidates could be identified, however with lengths of the enlargement zone less than 1 m (thus interpretation criterion e) does not apply).

The combined length of the breakout zones is approximately 35 m. The standard deviation is 10 degrees. According to the World Stress Map quality ranking criteria (e.g. Reinecker et al., 2003) this corresponds to a C-quality. The breakout azimuths found at different depths are shown in Figure 92.

As the long axis of the borehole breakouts corresponds to the direction of the minimum horizontal stress, the maximum horizontal stress direction is approximately perpendicular to this long axis. Therefore, the range of azimuths of the maximum horizontal stress ranges from 85 to 120 degrees. The average azimuth of the maximum horizontal stress is 106 degrees and the standard deviation is 10 degrees.

This average direction of the maximum horizontal stress is broadly consistent with the east-west direction reported for the Perth Basin and surrounding areas (King et al., 2008 and references therein). The blue line in Figure represents the maximum horizontal stress direction at the Harvey-1 well site.

All breakouts occur in the Lesueur sandstones formation. No breakouts have been found in the underlying Sabina sandstone formation (formation top at 2900 m depth). The bulk of the breakout zones are within the depth interval 1250-1370m. It is interesting to note that the formation top of the Wonnerup (a sub-formation of the Lesueur sandstone) is at 1354.1 m. It could mean that most breakouts occur in the transition zone from the Yalgorup-Wonnerup formation.

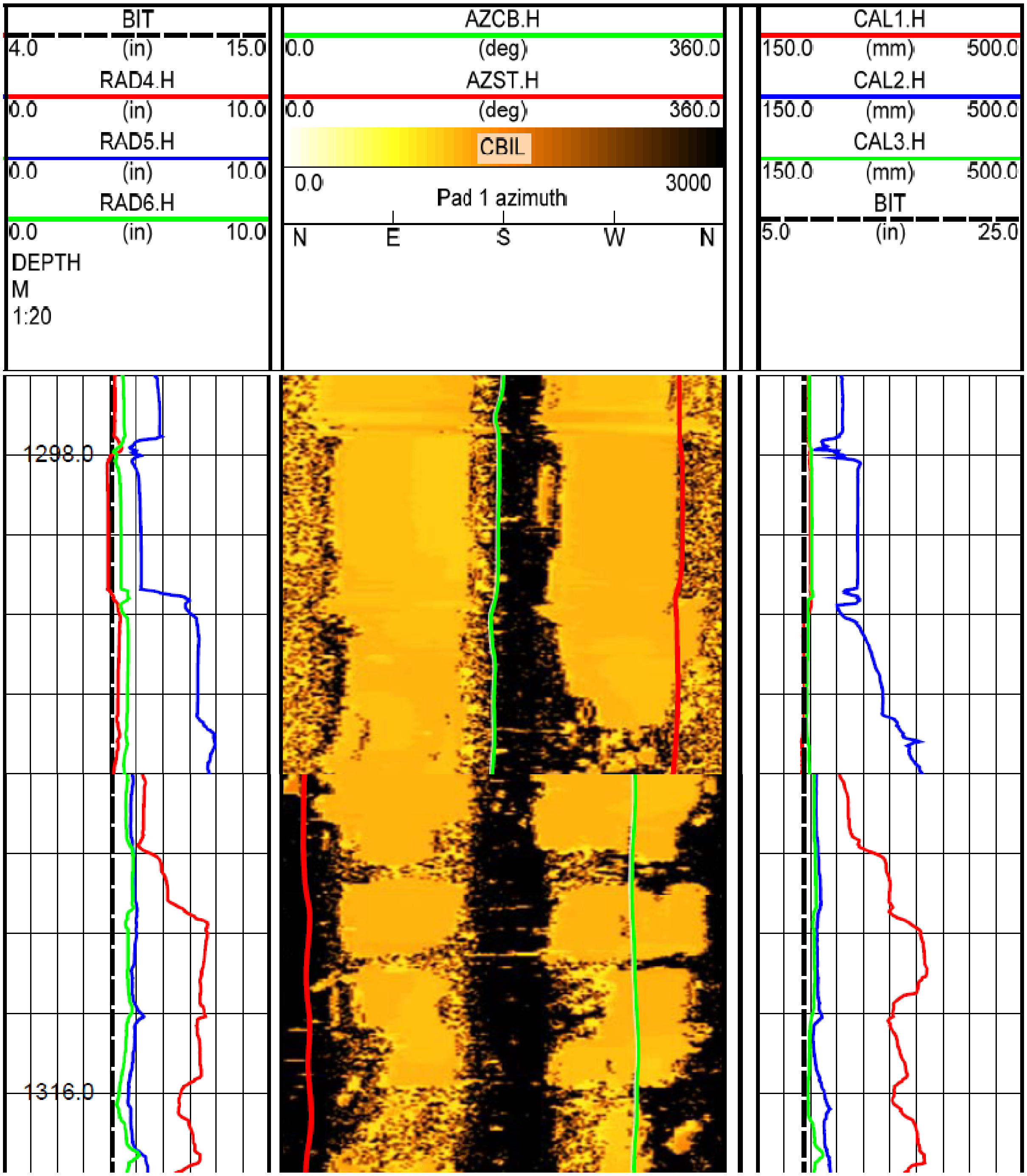

Figure 91. Two examples of breakouts. At depth 1298 m azimuth from STAR tool is approx. 320 deg. and the calliper 2 is increased. This corresponds to breakout azimuth of 200 deg. which can be also seen from the CBIL log. At depth 1316 m azimuth from STAR tool is approx. 25 deg. and the calliper 1 is increased. This corresponds to breakout azimuth of 205 deg. which can be also seen from the CBIL log.

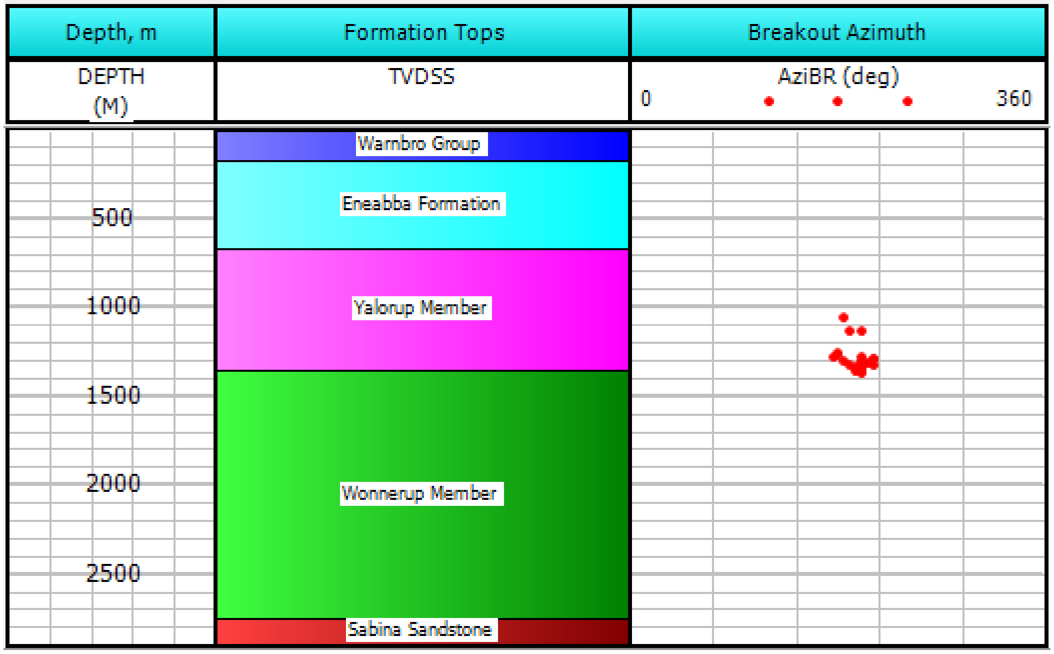

Figure 92. Breakout azimuths for the 21 zones of borehole enlargement

4.8. Stress fields characterisation – summary and key findings

The findings of this study can be summarized as follows:

1. A comprehensive review was performed by applying all available reports, data and logs, which facilitated the extraction of relevant information on wellbore instability issues experienced in GSWA Harvey-1 well.
2. At the time of this study, limited lab data were available to calibrate the rock mechanical properties.
3. The North Perth Basin is complex from the geological point of view with faults at different scales. These faults could potentially alert the direction of regional principal stresses.
4. A Rock Mechanical Model (RMM) for GSWA Harvey-1 well was constructed. The mechanical properties of formations such as Young's modulus (E_{sta}), Poisson's ratio (v_{sta}), uniaxial compressive strength (UCS), tensile strength (T_0) and friction angle along with the stress model; overburden stress (S_V), maximum and minimum horizontal stresses (S_h and S_H) and pore pressure were calculated and estimated.
5. The results of the Rock Mechanical Model analysis showed much weaker elastic and mechanical properties in the Yalgorup Member than in the Wannerup Member. The upper formation composed of intelayers of siltsone/claystone.

6. No unambiguous indicators of abnormal pressure zones appear to exist in drilling GSWA Harvey-1 well. Such indicators of overpressure as abnormally low density and/or velocities do not manifest themselves clearly in the Lesueur sandstone formation. Volume compensated density log exhibits a continuous increase of the density with the depth increase. Compressional and shear velocity in the formation are in a good agreement with laboratory velocities measured in saturated samples at zero pore pressure. Additionally, hydraulic permeability measured on core samples from Lesueur sandstone formation is high for shales. Therefore a normal pressure regime was considered based on the MDT pressure data. However, further work should be done for better understanding of pore pressure regime in the tight zones in Yalgorup Member as well as its potential sealing capacity.
7. The caliper data was used to calibrate the model. Generally the RMM model prediction is in a close agreement with caliper enlargement.
8. In general, a large stable mud weight window (MWW) is predicted; however, it is smaller for the Yalgorup Member than that of Wannerup Member as the Yalgorup Member of the Lesueur sandstone exhibits different, much weaker mechanical properties.
9. The reason of the borehole breakouts observed in the Yalgroup member is the narrow safe mud weight window in this section. The failure of the rock in this formation is due to its low mechanical properties and the existence of stress anisotropy. Practically, if increasing the mud weight is not possible during drilling this section, a good hole cleaning should be practiced to avoid any further drilling related issues.
10. The stress regime is dominantly strike-slip as SH>SV>Sh. However, moving towards shallower depth the stress regime tends to become reverse, i.e. the vertical stress becoming the lowest stress. The existing LOT data confirms this.
11. The average azimuth of the maximum horizontal stress is 106 degrees with the standard deviation of 10 degrees.

Based on these findings and conclusions, the following recommendations can be considered in order to improve the quality of further geomechanical studies in the same region.

1. LOTs are highly recommended to be performed in order to obtain and calibrate the horizontal stress profile.
2. Detailed monitoring and recording of incidents during drilling should be conducted and included in the daily drilling reports. Cutting sizes and shapes are important information which could be helpful in identifying the mode of rock failure.
3. Applying good hole cleaning practices is important within intervals with small mud weight windows.

4. Lab tests of samples from different formations are needed to calibrate and fine tune the model.

5. CONCLUSIONS AND RECOMMENDATIONS

Conclusions

2D surface seismic data reprocessing

Two 2D seismic lines (vintage 2011) were selected for reprocessing tests. The data quality is highly variable along these lines. Re-processing tests produced improved signal-to-noise quality, velocity estimates and reflection images, and uncovered the following issues:

- The source-receiver coupling is highly variable along the lines (near surface conditions change spatially), which significantly degrades the seismic data quality.
- Issues with crooked line geometry significantly degrade the ability to correctly image the subsurface geology (degree of line crookedness, dispersion of CMP points for line 11GA-LL1 is as much as 800m, out of plane events contaminate the data, significant imaging artefacts are present at rapid bends along the line direction, etc.);
- Processing of first break times allowed estimation of a detailed near-surface velocity model up to 600m depth. This velocity model indicates that the shallow part of the section is more heterogeneous than was initially expected, and has thus improved shallow imaging, now showing possible fault indications propagating to within 100-200m of the surface.
- Prestack depth migration (PSDM) test results show that 2D PSDM provides an improvement in seismic images compared to 2D prestack time migration (PSTM), especially when imaging steeply dipping fault-plane reflections, which appear to be more numerous and at a wider range of strike and dip angles than previously observed.

ZVSP borehole seismic data analysis

- A seismic-to-well tie using a VSP corridor stack was performed which shows that the VSP data quality and match to the logs and surface seismic is excellent at the site.
- V_P and V_S velocity profiles were derived for the entire ZVSP depth range to about 1200m depth, and correlate well with other data and velocity analysis techniques.
- Seismic attenuation estimates give values of the apparent Q factor of about 40 for almost the whole depth range.
- Attempts to estimate the relative contribution of scattering and intrinsic attenuation are limited by the log data available for the analysis, however estimates made from existing

log data show that contribution of the scattering component should play a very minor role.

- No significant azimuthal shear wave anisotropy was found from shear wave splitting analysis, possibly due to the limited offsets of the ZVSP coverage.

Stress field characterisation

South Perth Basin has a complex geological structure with a number of large and small scale faults. Major faults are roughly oriented N-S. However, minor faults are observed to be oriented NE-SW. This may affect the maximum horizontal stress direction, locally, in wells drilled adjacent to these smaller faults.

The study required the determination of the most appropriate correlations for deriving rock mechanical properties from petrophysical logs.

The main findings of this study can be summarized as follows:

- The rock mechanical properties of the Yalgorup member are significantly weaker than that of the Wonnerup member. The Yalgorup is composed of interlayers of siltstone and claystone whereas the Wonnerup member is mainly sandstone.
- The results of rock mechanical modelling (RMM) confirmed that the dominant stress regime in the field is strike-slip.
- Most of the borehole breakouts and drilling events reported were in the Yalgorup member. The RMM has a close agreement with these observations.
- The results of the Rock Mechanical Model built for the Harvey-1 well indicate that using a more suitable mud weight for drilling could have mitigated the rock failures.
- The estimated average direction of the maximum horizontal stress is broadly consistent with the east-west direction reported for the Perth basin and surrounding areas (King et al., 2008 and references therein).

Recommendations

3D seismic data acquisition:

- Design the 3D seismic acquisition geometry such that dip-lines run predominantly E-W, with the longest offsets and finest receiver sampling along the E-W direction, and the resulting rectangular bins are elongated in the N-S direction.
- acquire a high-resolution 3D up-hole survey to better determine near-surface velocities v(x,y,z) for accurate statics processing.
- Acquire supplementary high-resolution 2D/3D seismic data to image and map near surface carbonates, velocities and shallow faults (this can be done by NGL research partners).
- perform careful research processing of contractor 3D seismic data to enhance fault images, velocities, Q estimates, anisotropy/stress estimates etc. (NGL research partners).
- 3D prestack depth migration (PSDM) - with a special emphasis on a high-resolution velocity analysis - should be applied to the new 3D seismic data to help better understand the complex geologic structures and fault systems at the SW Hub site (NGL research partners).

VSP borehole seismic:

- acquire zero-offset VSP (ZVSP) and offset VSP (OVSP) data at future SW Hub site wells to get good estimates of anisotropy for stress estimates, consider acquiring walk-away VSP data. (VSP data analysis by NGL partners).
- at all future wells, fully log the borehole interval including and beyond the depth ranges where VSP data will be acquired. (contractor)
- acquire better quality VSP data (improved VSP sources etc.) by switching contractors and/or having NGL people onsite to QC the VSP acquisition.
- acquire high-quality research VSP data in the future with a permanent borehole array and NGL source equipment (NGL partners +ANLEC funding)

Stress field analysis:

- need better logs (including dipole shear) and log processing for Harvey-1 well and future wells to constrain stress estimates (contractor).

- Leak-off tests (LOTs) are highly recommended to be performed at every casing point in order to obtain and calibrate the horizontal stress profile.
- Formation stress tests using MDT data should be acquired and performed.
- Detailed monitoring and recording of incidents during drilling should be conducted and included in the daily drilling reports. Documenting cutting sizes and shapes is important information which could be helpful in identifying the mode of rock failure.

  Mud weights should be calculated based on the current rock mechanical modelling results prior to drilling future wells (to avoid formation damage and borehole breakouts)..

REFERENCES

Annetts, D., J. Hauser, J. Gunning, B. Gurevich, A. Bona, R. Pevzner, B. Harris, M. Urosevic and M. Al Ajami (2012), A deployment strategy for effective geophysical remote sensing of CO_2 sequestration, CSIRO report.

Backus, G.E., 1962, Long-Wave Elastic Anisotropy Produced by Horizontal Layering. J. Geophys. Res. 67, 4427-40.

Barclay, F., N. Mat Friah, R. Nesbit, A. Paxton and Z. John (2009), Stage 1(b): Assessment of the potential for carbon dioxide geosequestration in the lower Lesueur region, Unpublished, Schlumberger Carbon Services.

Bradford, I.D.R., Fuller, J., Thompson, P.J. and Walsgrove, T.R., Benefits of assessing the solid production risk in a North Sea reservoir using elastoplastic modeling. SPE/ISRM 47360, 1998.

Castagna, J.P., Batzle, M.L., and Eastwood, R.L., 1985, Relationships between Compressional and Shear-Wave Velocities in Clastic Silicate Rocks. Geophysics 50, 334-34.

Castagna, J. P., M. I. Batzle, and T. K. Kan (1993), Rock physics – The link between rock properties and AVO response in Offset-Dependent Reflectivity in Theory and practice of AVO Analysis, edited by J. P. Castagna and M. Backus, pp. 135-171, Society of Exploration Geophysicists, Tulsa, Oklahoma.

Eaton, B. A. (1969), Fracture Gradient Prediction and Its Application in Oilfield Operations, J Petrol Technol, 21(Oct), 1353.

End of Well Geological Data Report. Well Name: GSWA Harvey 1. Block No: S150 5814. Government of Wetern Australia. Department of Mines and Petroleum. pp. 259.

Fjær, E., R.M. Holt, P. Horsrud, A.M. Raaen and R.Risnes (2008), Petroleum Related Rock Mechanics, Elsevier, ISSN 0376-7361, 515 pp.

Gardner, G.H.F., Gardner, L.W., and Gregory, A.R., 1974, Formation Velocity and Density - Diagnostic Basics for Stratigraphic Traps. Geophysics 39, 770-80.

Greenhalgh, S.A., and King, D.W., 1980, Determination of Velocity-Depth Distributions by Inversion of Refraction Time-Distance Data. Bulletin of Australian Society of Exploration Geophysicists 11, 92-98.

Holt, M. J., 2012, Borehole Seismic Survey Field Report Zero Offset VSP in GSWA Harvey-1, Baker Hughes for Geological Survey of Western Australia, pp24

King, R. C., R. R. Hillis, and S. D. Reynolds (2008), In situ stresses and natural fractures in the Northern Perth Basin, Australia, Aust J Earth Sci, 55(5), 685-701.

Lawton, D.C. 1989. Computation of Refraction Static Corrections Using 1st-Break Traveltime Differences. Geophysics 54, 1289-1296 Doi 10.1190/1.1442588.

Newman, P., 1973, Divergence Effects in a Layered Earth. Geophysics 38, 481-88.

Pevzner, R., Gurevich, B., and Urosevic, M., 2011, Estimation of Azimuthal Anisotropy from VSP Data Using Multicomponent S-Wave Velocity Analysis. Geophysics 76, D1-D9.

Pevzner, R., Muller, T., Galvin, R. & Gurevich, B. 2012. Estimation of attenuation from zero-offset VSP data: CO2CRC Otway Project case study. SEG Technical Program Expanded Abstracts 31 http://dx.doi.org/10.1190/segam2012-0950.1.

Plumb, R.A. (1994), Influence of composition and texture on the failure properties of clastic rocks, SPE/ISRM 28022. In: Proc. Eurock'94. Delft, Netherlands, 29-31 August. A.A. Balkema, pp. 13-20.

Quan, Y.L., and Harris, J.M., 1997, Seismic Attenuation Tomography Using the Frequency Shift Method. Geophysics 62, 895-905.

Reinecker, J., M. Tingay and B. Müller (2003), Borehole breakout analysis from four-arm caliper logs, World Stress Map Project, Guidelines, http://dc-app3-14.gfz-potsdam.de/pub/stress_data/stress_data_frame.html

Ronen, J. & Claerbout, J.F. 1985. Surface-Consistent Residual Statics Estimation by Stack-Power Maximization. Geophysics 50, 2759-2767 Doi 10.1190/1.1441896.

Ross, W. & Shah, P. 1987. Vertical seismic profile reflectivity: Ups over downs. Geophysics 52, 1149-1154 doi:10.1190/1.1442379.

Slichter, L.B., 1932, The Theory of the Interpretation of Seismic Travel‐Time Curves in Horizontal Structures. Physics 3, 273-95.

Van Ruth, P. (2006), Geomechanics: Vlaming Sub-Basin, Western AustraliaRep., 30 pp.

Zoback, M. (Ed.) (2007), Reservoir Geomechanics, 448 pp., Cambridge University Press.

Zoback, M. D., and J. H. Healy (1984), Friction, Faulting, and Insitu Stress, Ann Geophys, 2(6), 689-698.

APPENDIX A – VELOCITY MODEL FROM ZERO-OFFSET VSP DATA PROCESSING

TVD (from surface, m)	MD (m)	Vp (km/s)	Vs (km/s)	Poisson	Vp/Vs
19.3	24.5	1.865	0.434	0.47	4.30
64.3	69.5	1.864	0.675	0.42	2.76
97.6	102.8	2.106	0.683	0.44	3.08
150.6	155.8	2.081	0.743	0.43	2.80
258.4	263.6	2.174	0.828	0.42	2.63
305.4	310.6	2.762	1.131	0.40	2.44
381.9	387.1	2.643	1.116	0.39	2.37
427.0	432.2	2.753	1.085	0.41	2.54
462.3	467.5	2.710	1.152	0.39	2.35
509.3	514.5	2.772	1.222	0.38	2.27
579.9	585.1	2.686	1.127	0.39	2.38
628.9	634.1	2.809	1.264	0.37	2.22
648.5	653.7	2.638	1.264	0.35	2.09
687.7	693.0	2.602	1.094	0.39	2.38
762.2	767.5	3.007	1.384	0.37	2.17
797.5	802.8	3.390	2.093	0.19	1.62
856.3	861.6	3.022	1.654	0.29	1.83
940.6	945.9	3.364	1.849	0.28	1.82
993.5	998.8	3.466	1.841	0.30	1.88
1019.0	1024.3	2.905	1.384	0.35	2.10
1058.2	1063.5	2.963	1.137	0.41	2.61
1097.4	1102.7	3.398	1.661	0.34	2.05
1140.6	1145.9	3.326	1.861	0.27	1.79
1183.7	1189.0	3.700	2.009	0.29	1.84

APPENDIX B – CHECK SHOT DATA

MD, m	TWTT (ms), datum = 19.1 m msl	TWTT (ms), datum = MSL	TWTT (ms), matched to CDP 4902, 11GA-LL2	Vint (km/s)	Vmean (km/s)	Vlay (km/s)
39.5	32.9	12.5	26.1	1.864	1.963	1.864
44.0	37.6	17.2	30.8	1.864	1.957	1.864
54.5	49.8	29.4	43.0	1.771	1.899	1.864
59.0	55.6	35.2	48.8	1.797	1.863	1.864
69.5	66.3	45.9	59.5	1.955	1.878	2.106
74.0	71.1	50.7	64.3	2.061	1.880	2.106
89.0	85.4	65.0	78.6	2.052	1.916	2.106
96.5	92.0	71.6	85.2	2.063	1.942	2.106
104.0	100.6	80.2	93.8	2.044	1.925	2.081
111.5	107.2	86.8	100.4	2.025	1.946	2.081
119.0	114.5	94.1	107.7	2.080	1.953	2.081
126.5	122.1	101.7	115.3	2.053	1.955	2.081
134.0	129.2	108.8	122.4	2.073	1.963	2.081
141.5	136.4	116.0	129.6	2.162	1.970	2.081
149.0	143.5	123.1	136.7	2.187	1.976	2.081
156.5	149.6	129.2	142.8	2.225	1.996	2.174
164.0	156.9	136.5	150.1	2.204	1.999	2.174
171.5	163.4	143.0	156.6	2.132	2.011	2.174
179.0	170.7	150.3	163.9	2.144	2.013	2.174
186.5	177.9	157.5	171.1	2.126	2.016	2.174
194.0	184.6	164.2	177.8	2.157	2.024	2.174
201.5	191.7	171.3	184.9	2.168	2.027	2.174
209.0	198.5	178.1	191.7	2.190	2.033	2.174
216.5	205.5	185.1	198.7	2.218	2.037	2.174
224.0	211.9	191.5	205.1	2.205	2.046	2.174
231.5	218.8	198.4	212.0	2.200	2.050	2.174
239.0	225.9	205.5	219.1	2.179	2.052	2.174
246.5	232.6	212.2	225.8	2.176	2.057	2.174
254.0	239.4	219.0	232.6	2.231	2.062	2.174
261.5	246.5	226.1	239.7	2.341	2.063	2.174
269.0	252.6	232.2	245.8	2.489	2.073	2.762
276.5	258.1	237.7	251.3	2.724	2.087	2.762
284.0	263.8	243.4	257.0	2.752	2.099	2.762
291.5	268.4	248.0	261.6	2.769	2.118	2.762
299.0	274.7	254.3	267.9	2.797	2.125	2.762

306.5	279.7	259.3	272.9	2.640	2.140	2.762
314.0	284.9	264.5	278.1	2.637	2.153	2.643
321.5	291.7	271.3	284.9	2.597	2.155	2.643
329.0	297.1	276.7	290.3	2.584	2.166	2.643
336.5	302.5	282.1	295.7	2.702	2.177	2.643
344.0	308.6	288.2	301.8	2.678	2.183	2.643
351.5	313.7	293.3	306.9	2.659	2.195	2.643
359.0	319.5	299.1	312.7	2.635	2.202	2.643
366.5	325.2	304.8	318.4	2.634	2.209	2.643
374.0	331.3	310.9	324.5	2.678	2.214	2.643
381.5	336.3	315.9	329.5	2.672	2.226	2.643
389.0	342.0	321.6	335.2	2.704	2.233	2.753
396.5	348.0	327.6	341.2	2.680	2.237	2.753
404.0	353.2	332.8	346.4	2.757	2.247	2.753
411.5	358.7	338.3	351.9	2.796	2.254	2.753
419.0	363.8	343.4	357.0	2.767	2.264	2.753
426.5	369.5	349.1	362.7	2.744	2.269	2.753
434.0	374.9	354.5	368.1	2.702	2.277	2.710
441.5	380.5	360.1	373.7	2.694	2.283	2.710
449.0	386.1	365.7	379.3	2.710	2.289	2.710
456.5	391.7	371.3	384.9	2.712	2.294	2.710
464.0	396.9	376.5	390.1	2.728	2.302	2.710
471.5	402.7	382.3	395.9	2.739	2.306	2.772
479.0	408.1	387.7	401.3	2.736	2.312	2.772
486.5	413.5	393.1	406.7	2.757	2.318	2.772
494.0	418.9	398.5	412.1	2.773	2.324	2.772
501.5	424.5	404.1	417.7	2.816	2.329	2.772
509.0	429.6	409.2	422.8	2.806	2.336	2.772
516.5	434.8	414.4	428.0	2.823	2.342	2.686
524.0	440.5	420.1	433.7	2.803	2.346	2.686
531.5	445.6	425.2	438.8	2.749	2.353	2.686
539.0	451.0	430.6	444.2	2.725	2.358	2.686
546.5	456.8	436.4	450.0	2.649	2.361	2.686
554.0	462.4	442.0	455.6	2.641	2.365	2.686
561.5	468.2	447.8	461.4	2.674	2.367	2.686
569.0	473.7	453.3	466.9	2.661	2.372	2.686
576.5	479.2	458.8	472.4	2.738	2.376	2.686
584.0	485.1	464.7	478.3	2.715	2.378	2.686
591.5	489.9	469.5	483.1	2.785	2.385	2.809
599.0	496.0	475.6	489.2	2.833	2.386	2.809
606.5	500.7	480.3	493.9	2.855	2.394	2.809
614.0	506.2	485.8	499.4	2.845	2.398	2.809
621.5	511.1	490.7	504.3	2.752	2.404	2.809
629.0	517.1	496.7	510.3	2.703	2.405	2.809

636.5	522.5	502.1	515.7	2.652	2.409	2.638
644.0	528.2	507.8	521.4	2.685	2.411	2.638
651.5	533.8	513.4	527.0	2.667	2.414	2.638
659.0	539.4	519.0	532.6	2.648	2.417	2.602
666.5	545.0	524.6	538.2	2.630	2.419	2.602
674.0	550.9	530.5	544.1	2.602	2.420	2.602
681.5	556.6	536.2	549.8	2.680	2.423	2.602
689.0	562.4	542.0	555.6	2.809	2.424	2.602
696.5	567.3	546.9	560.5	2.906	2.430	3.007
704.0	572.3	551.9	565.5	3.017	2.435	3.007
711.5	577.4	557.0	570.6	2.964	2.439	3.007
719.0	582.2	561.8	575.4	3.006	2.445	3.007
726.5	587.6	567.2	580.8	3.007	2.448	3.007
734.0	592.2	571.8	585.4	3.031	2.455	3.007
741.5	597.4	577.0	590.6	3.038	2.458	3.007
749.0	602.0	581.6	595.2	2.996	2.464	3.007
756.5	607.4	587.0	600.6	3.009	2.467	3.007
764.0	612.2	591.8	605.4	3.052	2.472	3.007
771.5	617.2	596.8	610.4	3.181	2.476	3.390
779.0	621.7	601.3	614.9	3.330	2.483	3.390
786.5	626.2	605.8	619.4	3.390	2.489	3.390
794.0	630.2	609.8	623.4	3.398	2.497	3.390
801.5	635.1	614.7	628.3	3.295	2.501	3.390
809.0	639.3	618.9	632.5	3.204	2.508	3.022
816.5	644.4	624.0	637.6	3.185	2.511	3.022
824.0	649.0	628.6	642.2	3.063	2.517	3.022
831.5	653.8	633.4	647.0	3.003	2.521	3.022
839.0	659.1	638.7	652.3	2.980	2.524	3.022
846.5	664.3	643.9	657.5	2.981	2.527	3.022
854.0	668.9	648.5	662.1	3.029	2.532	3.022
861.5	674.1	653.7	667.3	3.091	2.535	3.022
869.0	679.0	658.6	672.2	3.111	2.538	3.364
876.5	683.5	663.1	676.7	3.288	2.543	3.364
884.0	688.2	667.8	681.4	3.431	2.548	3.364
891.5	692.3	671.9	685.5	3.377	2.555	3.364
899.0	696.5	676.1	689.7	3.370	2.561	3.364
906.5	701.6	681.2	694.8	3.340	2.563	3.364
914.0	705.8	685.4	699.0	3.363	2.569	3.364
921.5	710.0	689.6	703.2	3.386	2.575	3.364
929.0	714.6	694.2	707.8	3.340	2.580	3.364
936.5	719.4	699.0	712.6	3.314	2.583	3.364
951.5	728.1	707.7	721.3	3.314	2.594	3.466
966.5	737.3	716.9	730.5	3.434	2.602	3.466
981.5	746.4	726.0	739.6	3.545	2.611	3.466

996.5	753.9	733.5	747.1	3.464	2.624	3.466
1004.0	757.7	737.3	750.9	3.389	2.631	2.905
1011.5	764.4	744.0	757.6	2.829	2.628	2.905
1019.0	768.1	747.7	761.3	2.829	2.634	2.905
1026.5	775.3	754.9	768.5	2.963	2.629	2.963
1034.0	778.8	758.4	772.0	2.934	2.637	2.963
1041.5	784.3	763.9	777.5	2.963	2.637	2.963
1049.0	789.1	768.7	782.3	2.757	2.640	2.963
1056.5	795.4	775.0	788.6	2.862	2.638	2.963
1064.0	800.4	780.0	793.6	2.993	2.640	3.398
1071.5	804.8	784.4	798.0	3.295	2.645	3.398
1079.0	809.5	789.1	802.7	3.384	2.648	3.398
1086.5	813.7	793.3	806.9	3.408	2.653	3.398
1094.0	818.2	797.8	811.4	3.463	2.656	3.398
1101.5	822.5	802.1	815.7	3.218	2.661	3.398
1109.0	826.7	806.3	819.9	3.343	2.665	3.326
1136.5	844.7	824.3	837.9	3.294	2.674	3.326
1144.0	847.0	826.6	840.2	3.343	2.684	3.326
1151.5	853.0	832.6	846.2	3.686	2.683	3.700
1159.0	856.5	836.1	849.7	3.739	2.689	3.700
1166.5	860.4	840.0	853.6	3.763	2.695	3.700
1174.0	863.4	843.0	856.6	3.555	2.702	3.700
1181.5	869.5	849.1	862.7	3.555	2.701	3.700
1189.0	873.0	852.6	866.2	3.555	2.707	3.700